University of Alberta

Counterflowing Jets: Scaling Factors and Mean Concentration Fields

by

Luis Alfonso Torres Garcia

A thesis submitted to the Faculty of Graduate Studies and Research
in partial fulfillment of the requirements for the degree of

Master of Science

Department of Mechanical Engineering

Fall 2009
Edmonton, Alberta

Examining Committee

Dr. Brian A. Fleck, Mechanical Engineering

Dr. David J. Wilson, Mechanical Engineering

Dr. Morris R. Flynn, Mechanical Engineering

Dr. Peter M. Steffler, Civil Engineering

To my parents and wife,...

...for my daughter and the little one coming.

Abstract

An experimental investigation of the mean scalar concentration field of jets into a uniform counterflow stream using planar laser induced fluorescence is presented. The centerline decay and radial spreading of the mean concentration field of the jet were investigated. Jet to counterflow velocity ratios ranging between 4 to 19 were used for two different jet diameters. Universal forms for the centerline concentration decay, and radial concentration profiles of the jet are presented. Scaling factors of the centerline concentration decay are introduced. The jet growth rate was found to be divided into two regions: the linear growth region and the power law growth region. The effects of inlet yaw angles on the penetration length, axial concentration decay and similarity region of the counterflowing jet are presented. A minimal effect of the tested inlet yaw angles on the concentration field was observed. Empirical expressions to predict the centerline concentration decay are given.

Acknowledgements

I would like to thank my supervisors Dr. Brian Fleck and Dr. David Wilson for their support and guidance. Thanks for giving me the opportunity to work with you in this investigation. I really appreciate the trust you put on my work and the opportunity of being part of the water channel, it was a remarkable experience.

I would also like to thank Dr. David Nobes for his valuable suggestions and guidance during the design and improvement of the measurement system used in this project.

I would like to manifest my gratitude to the staff of the Mechanical Engineering Machine Shop. Roger Marchand and Tuula Hilvo for their desire to help when I approached them. Especially, I want to thank Bernie Faulkner, "The Wizard". His technical expertise in electronics, photography, mechanical design, welding, and machining, made my life easier. As I used to say, "If you have any problem talk to Bernie, if you cannot solve it do not do anything else, keep talking to him and the solution will come."

I also want to thank Douglas for his help, the discussions and interactions held with him, and most importantly, his friendship, facilitated the way to the completion of this degree.

Finally, I would like to thank my wife Solange for her willingness to help and listen to me every time I needed. Her encouragement and support, sometimes were the only reasons that kept me moving through the different stages of this program, gracias gordita.

Table of Contents

List of Tables

List of Figures

List of Symbols

C	fluorescein concentration, mg.L^{-1}
C_c	concentration at the centerline of the jet, mg.L^{-1}
C_j	concentration at the exit of the jet, mg.L^{-1}
C_x	mean concentration along the x axis, mg.L^{-1}
C_y	mean concentration along the y axis, mg.L^{-1}
D	internal jet diameter, mm
I_f	fluorescence light intensity, digital counts (DC)
I_l	laser intensity
$\bar{I}_f$	averaged fluorescence intensity
Re_D	diameter based Reynolds number
U	horizontal velocity component, cm.s^{-1}
U_f	velocity of the dyed fluid, cm.s^{-1}
U_j	velocity of the jet, cm.s^{-1}
U_o	velocity of counterflow stream, cm.s^{-1}
U_r	jet to coflowing velocity ratio
V	vertical velocity component, cm.s^{-1}
x_p	maximum axial penetration length, mm
y_p	maximum lateral penetration length, mm
x_b	axial location of the maximum lateral penetration length, mm

Greek Letters

$\tau_{1/2}$	half-life time, ms
λ	length ratio (y_p/x_b)
β	length ratio (y_p/x_p)
ϕ	length ratio (x_b/x_p)
θ	inlet yaw angle, deg

Chapter 1

Introduction

1.1 Introduction and Background

Turbulent jets are probably the most studied shear flow and different geometries have been involved in the study of this flow. Some of the most well known studies involved jets in quiescent surroundings, jets in a coflowing stream, jets in crossflow, impinging jets, wall jets, and jets facing upstream into a uniform counterflow or counterflowing jets. Within this group of geometries the counterflowing jet has been the object of relatively few investigations (Arendt et al., 1956; Sui, 1961; Timma, 1962; Beltaos and Rajaratnam, 1973; Morgan and Brinkworth, 1976; McDannel et al., 1982; König and Fiedler, 1991b; König and Fiedler, 1991a; Lam and Chan, 1995; Yoda and Fiedler, 1996; Lam and Chan, 1997; Chan and Lam, 1998; Lam and Chan, 2002; Bernero and Fiedler, 2000; Tsunoda and Saruta, 2003). A counterflowing jet is originated by the flow of a jet nozzle facing an opposite stream. Figure 1.1 depicts the geometrical parameters of the counterflowing jet. The jet flow is generated by a nozzle which starts a momentum exchange process between the jet and the counterflow. This mixing process generates a decay of the velocity and concentration of the jet flow in the downstream jet direction. Eventually, the counterflow absorbs all the jet momentum that is then carried back with this opposite current (Yoda and Fiedler, 1996). The distance from the exit of the jet to the point where the jet is stopped is known as the jet penetration length (x_p), which very closely estimates the location of the stagnation

stream-surface at the centerline of the jet for turbulent Schmidt numbers near unity. The maximum lateral penetration and its location are defined in Figure 1.1 as y_p and x_b respectively. Three different regions can be identified in the counterflowing jet, the zone of flow establishment (ZFE) which contains the iso-concentration core and the transition to the established flow region (EFR). In the established flow region the jet flow is the dominant flow and the counterflowing jet behaves similar to a free jet(König and Fiedler, 1991b; Beltaos et al., 1999; Yoda and Fiedler, 1996). Finally there exists a mixing zone (MZ), where the flow is dominated by the counterflow stream; this region was defined by König and Fiedler (1991b) as the "wake region". In the mixing zone the jet is swept downstream by the counterflow stream. The counterflowing jet is known for its ability to enhance the mixing efficiency when it is compared with the other geometries (Beltaos and Rajaratnam, 1973; Bernero and Fiedler, 2000). Consequently, jets in counterflow streams are found in industrial applications that requires enhancing of mixing, as is the case of environmental fluid applications (Beltaos and Rajaratnam, 1973; Lam and Chan, 1995; Chan, 1999), "aerodynamic stabilizers in fuel devices and jet engines" (McDannel et al., 1982), and in the stabilization of afterburners or turbojet engines (Beltaos and Rajaratnam, 1973).

Some early studies carried out in counterflowing jets have been reported by Arendt et al. (1956), Sui (1961), and Timma (1962). Arendt et al. (1956) reported a dimensional analysis of the jet penetration length based on the magnitude of the velocity field of the counterflowing jet. Sui (1961) investigated the velocity field of the counterflowing jet and empirical formulas were obtained to predict the time averaged velocity components. Timma (1962) carried out an investigation of the effects of the initial conditions on the jet penetration length, as well as a study on the similarity of the velocity profiles. Probably one of the most complete investigations done in a counterflowing jet was presented by Beltaos and Rajaratnam (1973). In this work the time-average velocity field was investigated and a discussion of the results of previous investigators is given. Beltaos and Rajaratnam (1973) proposed a semi-empirical approach to predict the mean velocity field of the counterflowing jet. In addition, a

universal form of the centerline velocity is presented, where the penetration length of the jet is used as the length scale for the centerline velocity decay and the axial distance. Additionally, Beltaos and Rajaratnam (1973) presented a similarity function of the radial velocity profiles which was found to be a good representation of the radial velocity profiles.

Morgan and Brinkworth (1976) presented a remarkable investigation of the upstream penetration of a counterflowing jet in a turbulent pipe flow. It was demonstrated that the penetration of the counterflowing jet can be expressed as a function of the momentum fluxes of the two currents involved in the momentum exchange, as well as a linear function of the jet to counterflow velocity ratio. It was found by Morgan and Brinkworth (1976) that there were two different flow regimes that are related to the jet penetration. The low jet momentum regime, for which the jet to counterflow momentum flux ratio does not exceed the value of 0.5 and the high momentum regime which occurs at values above 1.5. A linear relationship between the jet penetration and the jet to counterflow velocity ratio was found based on experimental data; this linearity is lost when the high momentum regime is reached. A flow visualization study was presented by König and Fiedler (1991b), which was centered in the penetration length and the fluctuations of the counterflowing jet. König and Fiedler (1991b) identified two cases for the counterflowing jet based on the jet to counterflow velocity ratio U_r. The stable case, given for $U_r < 1.4$ and the unstable case for $U_r > 1.4$. In the unstable case, König and Fiedler (1991b) observed that the jet axis presented random oscillation through and around the mean axis of the jet, which were found to have a large amplitude. In later work, this author noticed that these amplitudes decrease with the inclinations of the jet nozzle (König and Fiedler, 1991a).

König and Fiedler (1991b) defined the counterflowing jet as "a combination of jet and wake - where the jet generates its own wake", dividing the counterflowing jet into a jet region, a deflection region and a wake region. The characteristics of each region were found to depend on the jet to counterflow velocity ratio (König and Fiedler,

1991b). Based on the previous, it is easy to understand the chaotic behavior of the fluctuations presented in the counterflowing jet. The fluctuating nature of this flow made it very difficult to fully define its characteristics, due to the difficulty obtaining high quality measurements of opposing streams. The development of non intrusive measurements techniques, such as laser induced fluorescence, laser Doppler anemometry, planar laser induced fluorescence, and particle image velocimetry, offered the opportunity to obtain new information describing the velocity field, and the measurements of the mean and instantaneous concentration.

Yoda and Fiedler (1996) presented flow visualization and mean concentration measurements of a counterflowing jet using planar laser induced fluorescence. This investigation was focused on determining the penetration length of the jet and the dilution of the centerline concentration for different values of U_r. The observed penetration lengths were found to agree with the results of Beltaos and Rajaratnam (1973), however, some disagreements were found with the findings of König and Fiedler (1991b) and Lam and Chan (1995). The effects of small inclinations of the jet nozzle were investigated in the study presented by Yoda and Fiedler (1996), but only effects on the penetration length were given, as well as a qualitative description of the effects on the fluctuations of the jet.

Perhaps the most complete and detailed investigation of the physics of the concentration field of a jet in a counterflow stream is given in the work presented by Chan (1999). The main findings of this investigation are summarized in the publications of Lam and Chan (1995), Lam and Chan (1997), Chan and Lam (1998), and Lam and Chan (2002). Chan (1999) presented an analytical model to predict the mean velocity and concentration field, these analytical expressions were obtained by considering the velocity field of the counterflowing jet. The mixing characteristics were studied by means of the laser induced fluorescence measurements of the mean concentration field and information on the centerline concentration dilution and the spreading of the jet in the radial direction is given. No similar investigation on the mean concen-

tration field of the jet has been presented. Though the number of published studies describing jets in other configurations is ample, studies such as the present work, on a jet in a uniform counterflow are meager in the literature and thus, there is a need for additional research to more fully describe this flow.

Among the number of investigations done on counterflowing jets, it is evident that the velocity field has been significantly more investigated than the concentration field. Additionally, in previous investigations on counterflowing jets only the maximum axial penetration has been presented as the scale factor. In the present investigation, planar laser induced fluorescence is used to characterize the mean concentration field of a jet in a uniform counterflowing stream. Scaling factors that generate universal forms of the centerline concentration decay are introduced in the present investigation. These scaling factors are used to produce empirical expressions to predict the centerline concentration of the counterflowing jet. The scales are obtained from the geometrical parameters of the 5 % contour of the mean concentration field. The study of the physical properties of the mean concentration field is used to define the different regions presented in the growth of the counterflowing jet. The results of this work will be used to validate and compare the findings of the physics properties of the mean concentration field presented by Chan (1999) and Yoda and Fiedler (1996). Additionally, a systematic study of the effects of small inlet yaw angle on the mean concentration field of the counterflowing jet is presented.

1.2 Layout of the Thesis

The present thesis is written in paper format, with every chapter intended to be a self-contained publication, so information from other chapters is not required in order to understand its content. As a consequence, the corresponding section of the experimental set-up is repeated in every chapter, with the exception of Chapter 6 which summarizes the findings of the present investigation and offers recommendations for future investigations. The outline of the present thesis is given as follows.

1.2.1 Chapter 2: Experimental correction process on a non-uniform laser sheet in a planar laser induced fluorescence technique for the study of jets

Chapter 2 describes the planar laser induced fluorescence system used to measure the concentration field of the counterflowing jet. Every component of the system is described and a brief literature review is presented for each component. The characteristics of every element in the optical system used to generate a thin laser sheet are given. Additionally, this chapter includes the steps involved in the calibration process used to obtain information about the concentration field using digital image analysis. The limitation of the calibration process, as well as its resolution, repeatability, and accuracy are discussed. Finally, the measurement technique is validated through the analysis of the concentration field of the near field of a *jet in a coflowing* stream.

1.2.2 Chapter 3: Centerline concentration of a counterflowing jet: averaged concentration measurements

This chapter presents an investigation of the centerline concentration decay and penetration length of the counterflowing jet. The counterflowing jet is investigated for jet to counterflowing velocity ratios in the range $4 \leq U_r \leq 19$. Scaling factors that generate a universal form of the mean centerline concentration of the counterflowing jet are presented in this chapter. These scaling factors are obtained from the geometrical length of the 5 % contour of the mean concentration field of the counterflowing jet. Empirical expressions to predict the centerline concentration decay of the counterflowing jet are shown in this chapter.

1.2.3 Chapter 4: Radial profiles of a counterflowing jet: averaged concentration measurements

The similarity region of the radial profiles (across rather than along the jet) of the counterflowing jet at different jet to counterflowing velocity ratios in the range $4 \leq U_r \leq 19$, are investigated and discussed in this chapter. Radial profiles of the mean

concentration field of the counterflowing jet are presented in this section. Length scales from Chapter 3 are used in the radial concentration profiles in an attempt to find a similarity form of the radial profiles of the counterflowing jet. The similarity function and the behavior of the spreading of the jet in the radial direction within the established flow region and mixing zone are investigated and discussed. The rates of growth of the counterflowing jet through the different regions are presented in this chapter.

1.2.4 Chapter 5: Experimental study of small inlet yaw angle effect in the flow of the counterflowing jet

In Chapter 5, planar laser induced fluorescence is used to investigate the effect of small yaw angles in the penetration length. Counterflowing jets with inlet yaw angles of 4 and 8 degrees are compared with the system aligned with the counterflow. The findings of the effects of the yaw angle in the penetration length, centerline concentration decay, and radial spreading of the counterflowing jet are presented. These effects are investigated for several jet to counterflowing velocity ratios, ranging from 4 to 19. Data of the penetration length, centerline concentration decay and radial profiles of the mean concentration field of the jet are given and discussed. Furthermore, the universal form of the centerline concentration decay as well as the similarity region of the radial profiles of the counterflowing jet are investigated for a counterflowing jet with small inlet yaw angles.

References

Arendt, J., Babcock, H. A., and Schuster, J. C. (1956). Penetration of a jet into counterflow. *Proc. ASCE Journal Hydraulics Division 82*, pages 1038 – 8 – 11.

Beltaos, S., Brinkworth, B. J., Lam, K. M., and Chan, H. C. (1999). Round jet in ambient counterflowing stream. *Journal of Hydraulic Engineering*, 125(4):428 – 432.

Beltaos, S. and Rajaratnam, N. (1973). Circular turbulent jet in an opposing infinite stream. *First Canadian Hydraulics Conference, Edmonton*.

Bernero, S. and Fiedler, H. E. (2000). Application of particle image velocimetry and proper orthogonal decomposition to the study of a jet in a counterflow. *Experiments in Fluids*, pages S274 – S281.

Chan, H. C. (1999). *Investigation of a round jet into a counterflow*. PhD thesis, Dept. of Civil Engineering, University of Hong Kong.

Chan, H. C. and Lam, K. M. (1998). Centerline velocity decay of a circular jet in a counterflowing stream. *Physics of Fluids*, 10(3):637 – 644.

König, O. and Fiedler, H. E. (1991a). On the asymptotic behaviour of axisymmetric turbulent jets in an ambient stream under arbitrary inclination angles. *Zeitschrift für Flugwissenschaften und Weltraumforschung*, 15(2):103 – 106.

König, O. and Fiedler, H. E. (1991b). The structure of round turbulent jets in counterflow: a flow visualization study. *Advances in turbulence 3*, pages 61 – 66.

Lam, K. M. and Chan, C. H. C. (2002). Time-averaged mixing behavior of circular jet in counterflow: Velocity and concentration measurements. *Journal of Hydraulic Engineering*, 128(9):861 – 865.

Lam, K. M. and Chan, H. C. (1995). Investigation of turbulent jets issuing into a counterflowing stream using digital image processing. *Experiments in Fluids*, 18:210 – 222.

Lam, K. M. and Chan, H. C. (1997). Round jet in ambient counterflowing stream. *Journal of Hydraulic Engineering*, 123(10):895 – 903.

McDannel, M. D., Peterson, P. R., and Samuelsen, G. S. (1982). Species concentration and temperature measurements in a lean premixed flow stabilized by a reverse jet. *Combustion Science and Technology*, 28:211 – 224.

Morgan, W. D. and Brinkworth, B. J. (1976). Upstream penetration of an enclosed counterflowing jet. *Industrial and Engineering Chemistry Fundamentals*, 15(2):125 – 127.

Sui, K. N. (1961). The investigation of the development of circular and planar jets in parallel and opposing streams. *Eesti NSV teaduste akadeemia, Tallin, Toimetised, Isvestia Fuusika - matemaatika - ja technikateaduste seeria. Seeria fiziko - matimaticheskikh nouk.*, 10:215 – 223.

Timma, E. (1962). Turbulent circular and falt streams developing in a counterflow. *Russian periodical, Adakemii Nauk. Estonskoy SSr, Seriya Fiziko - Matamaticheskikh i Tekhnicheskikh Nauk*, 4:253 – 262.

Tsunoda, H. and Saruta, M. (2003). Planal laser-induced fluorescence study on the diffusion field of a round jet in a uniform couter-flow. *Journal of Turbulence*, 4(013).

Yoda, M. and Fiedler, H. E. (1996). The round jet in a uniform counterflow: flow visualization and mean concentration measurements. *Experiments in Fluids*, 21(6):427 – 436.

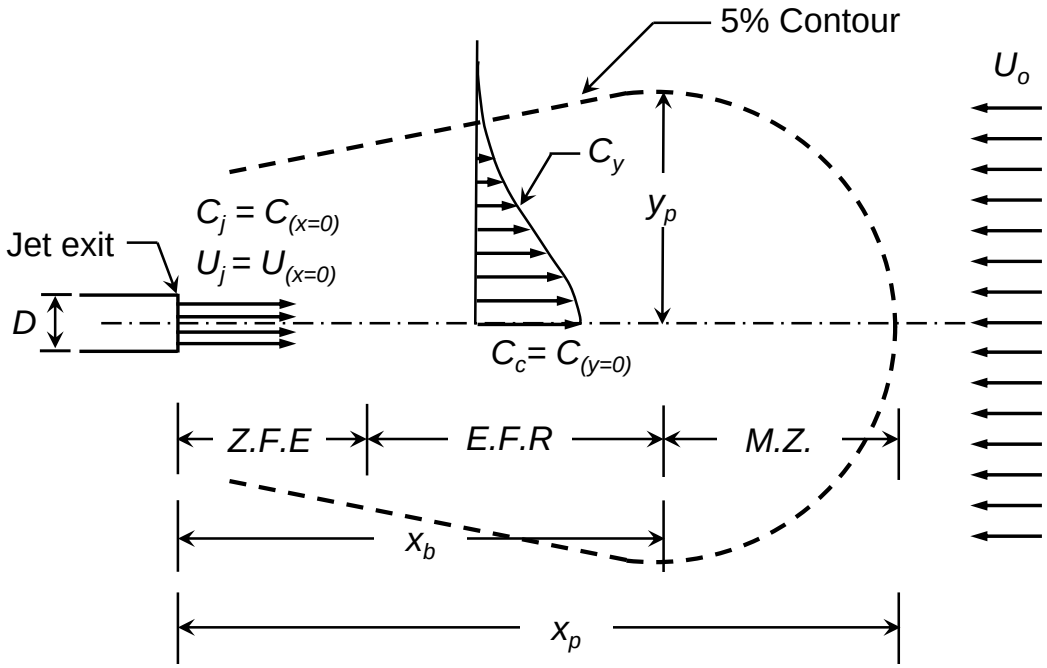

Figure 1.1: Schematic of the geometric parameters in the counterflowing jet (after Beltaos and Rajaratnam (1973), Yoda and Fiedler (1996), and Chan (1999)). Three different regions can be identified: the zone of flow establishment (ZFE), the established flow region (EFR), and the mixing zone (MZ).

Chapter 2

Experimental correction process on a non-uniform laser sheet in a planar laser induced fluorescence technique for the study of jets

Abstract

A experimental calibration process for a planar laser induced fluorescence technique was developed to obtain concentration measurements through the analysis of digital images. A Powell Lens® was employed to obtain a thin laser sheet. This calibration technique uses individual calibration curves for each pixel in the array. These calibration curves are obtained from a moving target of a known concentration. Post-processing of the gathered data is used to convert the laser intensity into dye concentration, removing the low background levels produced during the execution of the experiments. For low dye concentration levels, attenuation can be neglected and only the experimental calibration is necessary to obtain quantitative measurements of the scalar field in the aqueous medium, without the need for extensive data processing. The quantitative data obtained from this experimental process was validated through the analysis of the scalar field for a coflowing jet.

2.1 Introduction

Laser induced fluorescence is a spectroscopic technique commonly used in quantitative measurements of scalar concentration. In laser induced fluorescence, fluorescent dye is used as the tracer and a laser is employed to produce the florescence of the dye (Walker, 1987). Some of the earliest works in laser induced fluorescence were presented by Dewey (1976) and Owen (1976). This technique became very popular within the fluid dynamics community and it has been commonly used in the investigation of the qualitative and quantitative analysis of mixing and in the structures and dynamics of jets and shear layers. Detailed investigations of this technique were presented by Walker (1987) and Ferrier et al. (1993). Walker (1987) studied the technique, focusing on the instrumentation and the properties of the dye, considering the effect of "beam extinction or laser saturation" as well as temperature and pH dependence. A similar study by Ferrier et al. (1993) illustrated a method used to obtain the concentration of tracers in a turbulent flow field through which the correction of the digital signals were explained.

The three main components of laser induced fluorescence are the laser, the dye and the light detector. The fluorescent dye is a key component within the elements of laser induced fluorescence system. The susceptibility of a dye to thermal blooming and photobleaching changes with the dye, and it is considered a factor in determining the proper calibration and correction process when using laser induced fluorescence for concentration measurements (Walker, 1987; Saylor, 1995; Crimaldi, 1997; Wang and Fiedler, 2000). Thermal blooming and photobleaching are influenced by laser intensity, dye concentration, and the geometry of the measured volume (Saylor, 1995; Crimaldi, 1997; Wang and Fiedler, 2000). It has been proven that effects of photobleaching for configurations of single-point laser induced fluorescence and planar laser induced fluorescence are very different, being given that those effects are negligible in the latter configuration (Larsen and Crimaldi, 2006).

Several researchers have described different correction and calibration processes in order to obtain scalar concentration from fluorescence intensity. The most common method to obtain the constants that relate fluorescence intensity with laser power and dye concentration involves the use of an image of a known concentration. In some cases time consuming correction processes are applied to the calibration images in order to correct errors related to the laser light distribution, and light detector (Tian and Roberts, 2003; Cruyningen et al., 1990; Ferrier et al., 1993). Ferrier et al. (1993) proposed a correction process for attenuation when the important parameters such as attenuation coefficient of the medium, and the constant that relates fluorescence intensity with laser power and dye concentration have to be calculated before every experiment and for every scanline in the array. Ferrier et al. (1993) also suggested a method to correct the images for lens vignette error. Diez et al. (2005) show some geometrical considerations that can be used to correct the images due to the variation of the light intensity distribution in the laser sheet. Crimaldi (2008) describes a relatively simple image processing procedure that is an extension of the algorithms used by Crimaldi and Koseff (2001), Prasad and Sreenivasan (1990), and Koochsfahani et al. (1985), just to mention a few. However, the procedure described in the work presented by Crimaldi (2008) requires the calculation of parameters such as attenuation coefficient and concentration constant.

This chapter describes a calibration process where the individual calibration curves overcome the required calculation of the attenuation coefficients, and the correction process used to eliminate errors due to laser light distribution and light detector. This simple calibration process allows the measurements of scalar fields from the analysis of digital images. Additionally, the present study outlines the principal characteristics of the planar laser induced fluorescence system used, as well as a detailed analysis of each of the components. The calibration process is then applied in the study of the scalar field of a jet in a coflowing stream.

2.2 Planar laser induced fluorescence System

2.2.1 Fluorescent Dye

Fluorescein sodium salt (also known as disodium fluorescein, fluorescein, and Uranine) is used in the present investigation. This dye is commonly used in scalar measurements (Larsen and Crimaldi 2006). It possesses a high quantum efficiency and solubility, low temperature dependance, very low toxicity, and the pH effects can be easy to control (Walker, 1987; Magde et al., 2002). Fluorescein sodium salt has a maximum absorption of energy at a wavelength approximately 488 nm, later this energy is released as light in a larger wavelength, 515 nm (Walker, 1987). These absorption and emission spectrums are convenient for the instrumentation used in this study (sections 2.2.2 and 2.2.3).

Walker (1987) measured the effects of pH, temperature, dye concentration, and laser power on fluorescence intensity. It was found that fluorescence intensity changes with pH and temperature. The fluorescence intensity increases with pH reaching a plateau for values greater than 8. These results can also be seen in the investigation carried out by Zhu et al. (2006). The temperature effects on the fluorescence intensity of fluorescein sodium salt are not significant; Walker (1987) found a change of 6 % for a 20 ^{o}C variation. One of the most important findings of the investigation presented by Walker (1987) was the laser attenuation by the fluorescein concentration. This study presented an integral formulation to calculate the amount of dye attenuated along a straight beam path. However, if the fluorescein concentration is lower than 0.04 mg.L^{-1}, the attenuation of the laser results in a 1 % error (Walker, 1987).

In a later work, Saylor (1995) investigated the effects of photobleaching of fluorescein sodium salt when laser induced fluorescence is used to measure concentration. This work studied and compared the photobleaching of fluorescein under a continuous wave laser and a pulsed laser. It was found that the averaged fluorescence half-life

($\tau_{1/2}$) intensity was approximately four times greater when a pulsed laser is used instead of a continuous wave laser (2.9 ms and 12.3 ms respectively). This suggests that the use of a pulsed laser is more effective because it allows significant amount of photobleaching recovery in between the pulses. However, the experiments of Saylor (1995) were performed with the fluid at rest, where bleaching is more of a problem.

Wang and Fiedler (2000) performed a study of the combined effect of photobleaching and thermal blooming on concentration measurements using planar laser induced fluorescence. The biggest effect of thermal blooming is that it increases the molecular collision without allowing light emission, causing a reduction of the fluorescence intensity (I_f). Wang and Fiedler (2000) showed that thermal blooming has a strong dependance on the laser intensity (I_l) and fluorescein concentration (C); with the increase of I_l and C thermal blooming becomes more significant. Thermal blooming can be avoided by taking the heat away from the measuring volume, which can be achieved by keeping the fluid in motion at a high enough velocity (Wang and Fiedler, 2000).

Crimaldi (1997) studied the effect of photobleaching and velocity fluctuations in scalar measurements using fluorescein and rhodamine 6G. It was found that fluorescein was significantly more susceptible to photobleaching than rhodamine 6G, and that fluorescence intensity decreases with velocity. These results concur with the ones presented by Wang and Fiedler (2000). However, in the investigation presented by Crimaldi (1997), fluorescence intensity seems to reach a constant value for velocities higher than 45 cm.s^{-1}, while for the study presented by Wang and Fiedler (2000) this constant value of the fluorescence intensity was achieved at velocities greater than 20 cm.s^{-1}. It is important to mention that the works presented by Saylor (1995), Crimaldi (1997), and Wang and Fiedler (2000) were based on single-point laser induced fluorescence configurations for which the geometry of the measurement volume is different than the planar laser induced fluorescence configuration. A later work presented by Larsen and Crimaldi (2006) investigated the importance of pho-

tobleaching in planar laser induced fluorescence configurations. It was shown that photobleaching has little effect when using planar laser induced fluorescence .

Thermal blooming and photobleaching have been proven to be influenced by laser intensity, dye concentration, and the measure volume geometry (Crimaldi, 1997; Wang and Fiedler, 2000). Therefore it is possible to think that the effect of thermal blooming and photobleaching depends on the characteristics of the system, which suggests that the effects of thermal blooming and photobleaching in scalar measurements have to be tested for every specific system.

The dependance of fluorescence dye intensity on the velocity of the fluid which contains the dye were investigated in the present study. Figure 2.1 depicts the schematic of the experimental set-up used to analyze the relationship between fluorescence intensity and the velocity of the fluid carrying the fluorescent dye. A system with a valve and rotameter was installed at the dye inlet line in order to control the flow rate through a square glass tube. The square tube was placed perpendicular to the laser sheet and set at the center of the camera's field of view. The fluorescence intensity was measured at nine different velocities from 0 to 16 $cm.s^{-1}$. For every velocity 764 images were taken using a frame rate of approximately 39 Hz, with an exposure time of 10 ms. A 80 liter glass tank reservoir was used to store the dye. A mixing pump was used in the tank to keep the dye moving in order to ensure the uniformity of the solution. The desired dye concentration was set at the dye reservoir by diluting a master solution of 100 $mg.L^{-1}$of concentration. After increasing the concentration in the dye reservoir a period of 10 minutes was given in order to obtain a better mix of the dye solution. Eight different concentrations of fluorescein sodium salt were studied, the concentration was varied from 0.01 to 0.10 $mg.L^{-1}$. The sets of images were averaged in order to calculate the average intensity value for every dye concentration at the corresponding velocity. Figure 2.2 shows the average intensity plotted against the velocity of the dye in the square tube.

From Figure 2.2 appears that velocity has a negligible effect on fluorescence intensity for the system used in this investigation. A maximum error of 3 % was found when the dye was at rest and the dye concentration was 0.10 mg.L^{-1}. A stronger relationship between fluorescence intensity and velocity was found by Wang and Fiedler (2000), however this investigation was done for a single point laser induced fluorescence , whose results cannot be transferred to planar laser induced fluorescence geometries (Larsen and Crimaldi, 2006). For dye concentrations lower than 0.05 mg.L^{-1}, the relative deviation is not more than 2 %, therefore low concentrations of fluorescein sodium salt can be used in the PLIF method used in this investigation with little error. This result is also supported by the investigation performed by Larsen and Crimaldi (2006) in which they found a minimal effect of photobleaching in planar laser induced fluorescence applications.

As was previously mentioned, a key effect of dye concentration is the attenuation of the laser intensity, resulting in fluorescence intensity decay along the scanline of the laser sheet (Walker, 1987). Using the set-up shown in Figure 2.1, the intensity along a scanline of the laser sheet was observed. Figure 2.3 depicts the fluorescence intensity at different concentrations for a single scanline across the section of the square tube of 25.4 mm. This figure shows that for levels of dye concentration less or equal to 0.05 mg.$L^{-1}$the attenuation of the laser is minimal, with a relative deviation of approximately 2 %. The maximum relative deviation was found at 3 % for dye concentration of 0.10 mg.L^{-1}. These results agree with the ones found by Walker (1987) where the attenuation of the laser was found to be approximately 1 % for a concentration of 0.04 mg.L^{-1}. In the calibration process presented in this study a maximum concentration of 0.05 mg.L^{-1} is used in order to avoid correction process due to laser attenuation. This correction process is a time consuming post-processing procedure that in some cases requires the calculation of the attenuation constant for every experiment and every scanline in the array of the image (Ferrier et al., 1993).

2.2.2 Laser Sheet Generation

Some of the most common methods to generate laser sheets are the line scan method and cylindrical lens method. In the line scan method the laser beam is scanned along the field in order to generate the laser sheet. The cylindrical lens method uses a cylindrical lens to generate a constant laser sheet (Larsen and Crimaldi, 2006). To the knowledge of the author, the present study includes a new method to generate a laser sheet by the implementation of a Powell Lens®. This lens is able to spread the laser into a laser sheet with an approximate uniform intensity distribution (Powell, 1987). Figure 2.4 shows the schematic used to generate the laser sheet. The laser used in this investigation was a 2.1 Watts Argon ion laser. It was operated in a single mode at a wavelength of 488 nm, this wavelength is the corresponding to absorption wavelength of fluorescein sodium salt (Walker, 1987).

The quality of the image depends on the way the laser sheet is generated (Crimaldi, 2008). For a laser sheet generated by the line scan method, the images are very clear but have a small spatial distortion. For the images of the laser sheet created by a cylindrical lens (static sheet), the spatial resolution is not disturbed, but the image exhibits some blur. The blurring exhibited by the images can be minimized by selecting a short exposure time (Crimaldi, 2008). As was previously mentioned, no other studies have reported the use of the Powell Lens® to generate a laser sheet, therefore, the effects of the Powell Lens® on image quality and photobleaching have not been established. In the present study, these effects are considered to be approximately equal to the laser sheet generated using a cylindrical lens.

In order to minimize the amount of losses in the reflective mirrors (see Figure 2.4) two 25.4 mm diameter laser line dielectric mirrors were chosen for this application. These mirrors are fabricated by Newport and they are able to reflect approximately 99 % of the laser within an incident angle of $\pm$ 45^{o}. A coated 25.4 mm diameter focusing lens was used to focus the beam at 1000 mm. The focal point was located at approx-

imately the center of the camera field of view in order to have the maximum of the Rayleigh length at the center of the field of view of the camera. The Rayleigh length for the configuration shown in Figure 2.4 was found to be approximately 402 mm.

The resulting light distribution in the laser sheet for two dye concentrations is shown in Figure 2.5. This figure was obtained by recording the intensity values of the laser sheet along the x direction of the square tube using the setting depicted on Figure 2.4. The intensity profiles reflect a drop at the center of the laser sheet, this sink of light is about 30 % of the maximum intensity registered in the laser sheet. This distribution of light in the laser sheet depends on the quality of the laser beam and the angle to which the beam is being spread (Powell, 1987). Therefore, a better Gaussian distribution of the light in the cross section of the beam results in a better light distribution in the laser sheet. Additionally, this light distribution is affected by imperfections in the lens, dust on lens, and slight angle changes. All these conditions are difficult to control, however, for the calibration process used in this study, if the distribution of light in the laser sheet does not change when a experiment is being carried out, the non uniformities of the laser sheet can be corrected by the calibration process (a detail of this process can be seen in Section 2.3).

2.2.3 Light Detector

The light detector used in this study was a two dimensional array CCD camera. This camera is a 12 bit SensiCam high speed CCD system, with a resolution of 1280 x 1024 pixels. The specifications of this camera are shown in Table A.1. The maximum quantum efficiency of the camera is approximately 500 nm, which is close to the spectrum emission of fluorescein sodium salt. The quantum efficiency of the camera at the spectrum emission of the fluorescein sodium salt is approximately 40 %.

A light detector is a device that counts photons and these are presented in any kind

of light source. In order to avoid photons from others sources affecting the emitted signal of the fluorescent dye, a filter was placed in front of the lens of the camera. In this investigation a Kodak Wratten filter No. 12 was used to eliminate the light coming from the direct emission of the laser in order to avoid contamination of the data. The filter has effectively zero transmittance at the excitation wave length (490 nm) and at the laser wavelength (488 nm), while allowing 55 % of transmittance at 520 nm and reaches the 78 % transmittance at 530 nm. The main drawback of choosing this filter is that at the peak of the emission spectrum a considerable percentage of the emitted fluorescence light is being wasted. This drawback is however outweighed by the advantages of attenuating the light from the very high intensity emission from the laser.

In the work presented by Ferrier et al. (1993) some of the most common problems with the light detector are investigated. The "camera lens vignette" is presented, in this study, as the intensity variation along the sensor array. The sensor in "the edges of the array receive less light than the locations at the center of the ship" (CDD array) causing the image to be brighter at the center. Ferrier et al. (1993) corrected this problem by taking an image of a flat board section illuminated by sunlight. This image was then normalized and every image was divided by this normalized flat image. Three other options to correct this problem are presented by Cruyningen et al. (1990), however, this problem is overcome by the current method of using individual calibration curves for each pixel.

The aspect ratio of the pixels was studied by imaging a scaled paper with a resolution of 1 mm. It was found that the individual digitized pixels were approximately square and constant along both directions. The temporal noise was investigated by taking a sequence of images for three different dye concentrations. Figure 2.6 depicts the time series response of the fluorescence intensity for 0.00, 0.03 and 0.05 mg.L^{-1}of dye concentration. The amplitude of the noise increases with dye concentration. However, when the signal is normalized by the average fluorescence intensity ($\bar{I}_f$), obviously the

maximum relative deviation from the average intensity decreases for higher values of light intensity. The normalized fluorescence intensity is shown in Figure 2.7, for the case of 0.05 mg.L^{-1} the noise was found to be ±6 % of the signal. The noise became more significant for low dye concentration, for 0.03 mg.L^{-1}and 0.00 mg.L^{-1}this noise is approximately ±7 % and ±10 % respectively. In our calibration process the noise is not removed, therefore, it becomes a significant component of light intensity uncertainty.

The background pattern of the camera was investigated for different camera configurations. Figure 2.8 depicts the images of the camera dark response for the sensor of the camera covered (Figure 2.8a) and the corresponding image when the camera lens was covered (Figure 2.8b). These images were taken by obtaining the average of 400 frames with a size of 1280 x 1024 pixels. A noise pattern with the shape of a vertical band can be seen from Figure 2.8, it is important to point out that this noise varies in 1 digital count. In Figure 2.8b it is possible to appreciate that the intensity of the noise pattern is being slightly reduced by incorporating the lens into the system. A significant effect can be seen when the filter and the laser are added to the system. This can be observed in Figure 2.9a and Figure 2.9b. These figures show irregularities that were not exhibited in Figure 2.8a and Figure 2.8b. In order to correct for this background pattern, an averaged image of the background pattern is subtracted from the calibration and experiment images. The background pattern is affected by any change in the light distribution of the laser sheet, which varies for every experiment. Therefore, the calibration procedure accounts for all the background patterns by taking an average background calibration of images for every experiment. This averaged background image is also used as the calibration image for dye concentration equal to 0.00 mg.L^{-1}.

2.3 Calibration Process

The experimental setup used for the calibration process is shown in Figure 2.1, a detailed description of these components can be seen in Section 2.2.1. The square glass tube has to be placed at the same location of the jet, under the same condition for which the experiments are executed. It is important to indicate that there are loses when the laser sheet passes through the glass, however, these losses were experimentally found to be negligible. A key factor for the calibration procedure is that it is based on two assumptions. First, it is assumed that the attenuation of the laser intensity due to the fluorescent dye is negligible, which can be achieved by using a low dye concentrations. Secondly, the light distribution in the laser sheet is constant through the execution of the experiment. This is possible to achieve by letting the laser warm up for a long before use, approximately 2 hours. The calibration process is carried out after the execution of the experiments, therefore, if the laser sheet light distribution changes through time, the individual calibration curve obtained in the calibration will not correspond to the light distribution used in the experiment. The calibration procedure can be summarized in the following steps.

1. A master solution of dye is prepared and used to obtain the desired dye concentration in the dye tank (see Figure 2.1). This reservoir is used to store the dye that circulates through the square tube. The velocity of the fluorescent dye is set at 8 $cm.s^{-1}$. This velocity of fluorescent dye results in approximately the average fluorescence intensity value for the range of velocities studied (see Section 2.2.1).

2. Three calibration images were taken after the execution of the experiments. These calibration image sequences are taken at known fluorescent dye concentration. Three concentrations for the calibration images are set to be 0.00 $mg.L^{-1}$, the peak inlet dye concentration, and a concentration within these two. Every calibration image sequence is obtained by traversing the glass square tube along the camera field of view while the image sequence is being taken. The purpose

of moving the square tube through the camera field of view is to approximate the ideal situation when an image of a fluorescein line within the dimensions of a row of pixels is taken at every row. This is achieved by averaging the fluorescence intensity for every pixel just considering the moment for which the square tube are present. The corresponding calibration images for a zero concentration is also taken after the execution of the experiment in order to check for any background dye levels, which were found to be minimal. Figure 2.10 shows an example of one frame of a calibration image sequence, this image was taken using a fluorescein sodium salt concentration of 0.05 mg.L^{-1}. Camera settings for calibration are set to match the settings to be used for experiments. Likewise, the water used to obtain the desired dye concentration in the calibration images must be the same as is to be used in the experiment in order to account for the effect of pH and temperature in the fluorescein dye.

3. The calibration images are later processed by a postprocessing code. This code builds a calibration image by selecting the maximum I_f value for every pixel in the whole sequence. Once the maximum calibration image is built ($M_{max(i,j)}$), the corresponding amplitude of the signal for the fluorescent dye concentration used in the calibration is subtracted in order to obtain the minimum value of the calibration image ($M_{min(i,j)}$). The calibration image sequence was averaged just for the values between $M_{max(i,j)}$ and $M_{min(i,j)}$, resulting in the averaged calibration image (CI). This was done in order to avoid to average light intensity values in the moment of the absence of the traversing square tube. Figure 2.11 depicts the built calibration image for a dye concentration of 0.05 mg.L^{-1}. The built calibration images are stored in a 3D array. In order to simplify the understanding they are noted as $CI_{i,j,1}$, $CI_{i,j,2}$, and $CI_{i,j,3}$ for the minimum, medium, and maximum concentration in the calibration images respectively.

4. After the calibration images are obtained for every dye concentration, the postprocessing code was used to subtract the average background pattern of the images ($B_{(i,j)}$) and to determine the coefficients of the linear fit for each pixel

in the array. The data were fit into a linear fit of the form

$$C_{(i,j)} = I_{f(i,j)}.a_{(i,j,2)} + a_{(i,j,1)} \tag{2.1}$$

where, $I_{f(i,j)}$ is the fluorescence intensity image in digital counts that is being converted into the dye concentration matrix $C_{(i,j)}$. It is important to mention that before introducing the fluorescence intensity image into Equation 2.1, the average background pattern image should be subtracted from this image.

As can be seen, the simple calibration process described previously can be used with any kind of fluorescein dye, as long as the two key conditions are fulfilled: low dye concentration to neglect dye attenuation and constant light intensity distribution during the execution of the experiment. In order to validate the calibration process described previously, the scalar field of a coflowing jet is studied in Section 2.5.

2.4 Errors and Uncertainties

Planar laser induced fluorescence is a technique that involves several components, each of these components with their own uncertainties and errors which contributes to the experimental error in the system. Optical uncertainties can be found in the misalignment of the optical components that results in variations of the light distribution in the laser sheet. This light distribution can be also affected by temperature variations in the cavity of the laser, which, can contribute to the uncertainties of the system. Measurement devices can be a source of significant uncertainties in the system. Flow and volume measurement devices are used to control the flow rate for the calibration process and the amount of dye used to generate the desired dye concentration for the calibration images. As was mentioned before, fluorescence intensity is not purely a function of concentration, it also slightly depends on the velocity of the fluid, which generates an error into the calibration system. If the velocity of the fluid is slower than the velocity used in the calibration process, the observed concentrations will be slightly smaller for the same dye concentration due to the small effect of velocity dependance on the fluorescence intensity. Nevertheless, this error was assessed

to be less than 2 %. Finally, the errors in the light detector can be associated with the digitalization process, which can be minimized by increasing the signal to noise ratio, which can be achieve by increasing the fluorescence concentration of the dye. However, by increasing the concentration a error due to dye attenuation is introduced.

In order to quantify the error associated in the calibration process, a set of 400 images of three known fluorescein dye concentrations were analyzed using the calibration process described in Section 2.3. The different concentrations of fluorescein sodium salt were circulated through the square tube (Figure 2.1) while the images were taken. Figure 2.12 shows the average fluorescence light intensity and the corresponding dye concentration along the square tube obtained using the calibration process described previously. It can be seen that this calibration process is able to correct the uneven distribution of the light intensity in the laser sheet (dotted line), resulting in more constant value of the dye concentration (solid line). Several positions across the square tube were analyzed, for the worst case scenario the resulting dye concentration was found to be within 5 % of the expected value. However, these levels of error were found in areas where the fluorescence signal was affected by irregularities of the glass and laser reflections on dust or mineral particles in the water, and thus can be designated as wild data. Excluding wild data, the error of predicting the dye concentration was found to be within 2 %, which for most applications is an acceptable level of error.

The errors in the calibration process were found to be larger for instantaneous fluorescein dye concentration. Figure 2.13 depicts the instantaneous fluoresced light intensity and the corresponding instantaneous dye concentration obtained using the calibration process described previously. Although, the calibration process was able to correct the non-uniformity of the laser sheet (dotted line) it was found that using Equation 2.1 the dye concentration is over predicted by approximately 14 % for the worst case scenario. Additionally, the instantaneous background noise level happened to be lower than 0.003 $mg.L^{-1}$. The background noise for the average case was found to be approximately 0.0005 $mg.L^{-1}$. Therefore, the errors in measuring the dye

concentration using the calibration images are minimized when the mean dye concentration field is desired. This noise level is related to the temporal noise component in the signal, which becomes part of the uncertainty in the measurements, that can be only minimized by a time average (Ferrier et al., 1993).

2.5 Application to a Coflowing Jet

The mean concentration field of a coflowing jet was obtained through the use of the calibration process presented in this study. The mean scalar field was computed and used to generate radial and axial concentration profiles. The investigation of the concentration field of the coflowing jet will be used to provide the validation of the experimental technique used in this investigation.

2.5.1 Experimental Setup

The experiments were carried out in a closed loop water channel facility in the Mechanical Engineering Department at the University of Alberta. Figure 2.14 depicts the experimental set-up of the test section used in the experiments. The center of the test section set-up was located at approximately 3200 mm downstream from the water channel entrance. A glass screen was placed on top of the free surface to avoid any distortion due to the small waves generated at the surface. The laser sheet was obtained using the optical arrangement depicted in Figure 2.4. The camera was placed at approximately 1200 mm from the axis of the coflowing jet. This coflowing jet was set 200 mm from the bottom of the water channel, the level of water was kept at a height of 400 mm for all the experiments.

A uniform grid was place at the inlet of the water channel (see Figure 2.14) built with flat stainless steel bars of 19.2 by 5 mm of cross section area. The total open area was approximately 56 % with a mesh spacing of 76.2 mm. This grid turbulence generates near uniform velocity profile for the streamwise component, with variations found to be within 5 % (Hilderman, 2004). At the test section the turbulence intensity was

found to be about 4 % for the mean horizontal (Hilderman, 2004). The velocity of the water used for the experiments was 5 cm.s^{-1}. The jet was generated by a cylindrical nozzle of internal jet diameter (D) equal to 8.81 mm. It was designed to have an inlet length of $104D$ in order to obtain a fully developed flow. Three different jet velocities were studied, ranging from laminar to turbulent flow in the pipe inlet; 18, 38.4, and 67.4 cm.s^{-1}(U_o). The corresponding jet to coflowing velocity ratios (U_r) were: 4, 8, and 14 with diameter based Reynolds number (Re_D) of 1500, 3350, and 5900. The images of the jet were grey level images taken with the 12 bit camera described in Section 2.2.3. At every flow jet condition a set of 1000 images was taken at a rate of 19.32 Hz. The exposure time used in these images was 10 ms.

2.5.2 Experimental Results

Figure 2.15 depicts the time averaged fluorescein light intensity images for the three different velocity ratios. The contours in the images exhibit light intensity structures that do not correspond to the concentration field. Figure 2.16 depict the same average images after the calibration process is applied. It can be seen that the light intensity structures have been removed after the images are corrected by the calibration process. In Figure 2.16 it is possible to observe the expected averaged scalar distribution, where it is possible to identify the zone of flow establishment and the region of fully developed flow (Chu et al., 1999). Figure 2.17 depicts the dimensionless radial time averaged concentration profiles for three jet-to-coflowing velocity ratios. It is possible to appreciate the expected self similarity of the coflowing jet once the fully developed region has been reached. These results agree with the work presented by Chu et al. (1999), and Antoine et al. (2001). The fit presented in the data of Figure 2.17 corresponds to a Gaussian fit of the form:

$$\frac{C_y}{C_c} = \exp\left[-\left(\frac{y}{y_{1/e}}\right)^2\right] \tag{2.2}$$

where C_y is the local mean concentration, C_c is the mean concentration at the cen-

terline of the jet, y is the radial position, and $y_{1/e}$ is the radius at which $C_y = e^{-1}C_c$. This Gaussian fit is commonly assumed for the axial velocities in the fully developed region (Chen and Davidson, 2004). From Figure 2.17 it is possible to observe that the one data set which visibly departs from the trend is for the case of a laminar inlet, that has a delayed spread due to late transition to turbulence (Figure 2.16a). It is important to indicate that for this flow condition ($U_r = 4$) the potential core extends until approximately $14D$, therefore, at $15D$ it is likely that the fully developed region has not been completely established here. Even though the Gaussian function fits well with most of the data shown in Figure 2.17, it can be seen that at about 20 % of the centerline concentration, the data start diverging from the Gaussian fit. This could be the resulting effect of the coflowing stream in the spreading of the jet, which depends on the jet to coflowing velocity ratio (Chu et al., 1999). Similar results to those in Figure 2.17 were reported by Davidson and Wang (2002). Additionally, it is important to recall that for very low concentrations (low florescence intensity), the error in the measurement technique increases, affecting the data. In these profiles, 20 % of the centerline concentration represents, for the worst case scenario, 10 % of the fluorescent dye concentration at the source of the jet, which is very close to the instantaneous background noise (see Section 2.4).

The dilution of the centerline concentration of the coflowing jet is depicted in Figure 2.18. The centerline dilution of the concentration is shown using the dimensionless form presented by Chu et al. (1999) and Davidson and Wang (2002). It is possible to observe that the normalized dilution of the centerline concentration varies linearly with x/l_m on a log-log axes, which was also observed in the investigations previously cited. The length l_m is defined as the momentum excess length scale and it is given by

$$l_m = \frac{(M_{eo})^{1/2}}{U_o} \tag{2.3}$$

where U_o is the ambient fluid velocity and M_{eo} is the excess momentum per unit

density,

$$M_{eo} = (U_j - U_o)\ U_j\ \frac{\pi D^2}{4} \tag{2.4}$$

in Equation 2.4 U_j is the magnitude of the jet exit velocity, and D is the diameter of the jet nozzle. For the developed jet far downstream, the data shown in Figure 2.18 agree well with the experimental studies of Chu et al. (1999) and Davidson and Wang (2002) supporting the experimental technique used in this investigation.

For the fully developed region of the jet, the centerline mean concentration variation with the axial distance is shown in Figure 2.19. The exit concentration of the jet (C_j) is normalized by the local mean concentration in the axis of the jet (C_c). Using the equation for the centerline velocity variation presented by Hussein et al. (1994), it is possible to write the centerline mean concentration variation with the form:

$$\frac{C_j}{C_c} = \frac{1}{B_c}\left(\frac{x}{D} - \frac{x_o}{D}\right) \tag{2.5}$$

where the constant B_c is related with the spread constant B by:

$$B_c = \frac{1}{2}\pi^{\frac{1}{2}} B \tag{2.6}$$

as can be seen from equations 2.5 and 2.6 the greater the slope of the fitted line, the smaller the value of B which represents a higher decay rate of the centerline concentration. Figure 2.19 depicts a higher centerline concentration decay for the jet with the smaller jet to coflowing velocity ratio ($U_r = 4$). The values of B_c found for the case of $U_r = 8$ and $U_r = 14$, are $B_c = 6.7$ and $B_c = 6.3$ respectively, and are comparable to the ones presented by Antoine et al. (2001). Nonetheless, the values for the virtual origins found in this study significantly differ for the one presented by Antoine et al. (2001). Although, there is not enough information related with the centerline mean concentration variation, studies (Hussein et al., 1994) on the centerline velocity variation have shown a discrepancy in the location of virtual

origins with different values for $x/D < 50$ ($x_o \simeq 3$D and $B_c \simeq 5.7$) and for $x/D > 50$ ($x_o \simeq 7D$ and $B_c \simeq 5.0$). These numbers are comparable to the corresponding results of the turbulent jets presented in this study. Antoine et al. (2001) presented data for $x/D > 50$ which is a significantly larger range compared with the one studied in this investigation.

2.6 Conclusion

The planar laser induced fluorescence measurement technique used in the present study has been described in detail. A new method to generate a thin laser sheet was suggested in this study. It was demonstrated that the effect of thermal blooming and photobleaching are not significant in the planar laser induced fluorescence system described in this study. The results presented in this investigation show that the effects of the velocity in the fluorescein dye concentration are negligible within the range of velocities investigated.

A simple calibration process to obtain information of the concentration field using image analysis was described. This calibration process was proven to be independent of the light intensity distribution in the laser sheet. The use of the individual calibration curves for each pixel in the array corrects the variation of the quantum efficiency among the pixels of the camera. The simple calibration process described in this study can be easily performed prior to each experiment and the postprocessing of the data does not required an extensive computational effort. The calibration process described in this chapter can be used independently of the fluorescein dye use in the planar laser induced fluorescence technique.

Scalar field data for a coflowing jet in a open water channel was presented. Measurements were performed for three different jet conditions. The time averaged scalar concentration field agreed well with the theory and previous experimental studies done in similar geometries, thus providing validation for the presented experimental

technique.

References

Antoine, Y., Lemoine, F., and Lebouche, M. (2001). Turbulent transport of a passive scalar in a round jet discharging into a co-flowing stream. *European Journal of Mechanics B-Fluids*, 20(2):275 – 301.

Chen, Y. and Davidson, M. J. (2004). Radial velocities in axisymmetric jets and plumes. *Journal of Hydraulic Research*, 42(1):29 – 33.

Chu, P. C. K., Lee, J. H., and Chu, V. H. (1999). Spreading of turbulent round jet in coflow. *Journal of Hydraulic Engineering*, 125(2):193 – 204.

Crimaldi, J. P. (1997). The effect of photobleaching and velocity fluctuations on single-point LIF measurements. *Experiments in Fluids*, 23(4):325 – 330.

Crimaldi, J. P. (2008). Planar laser induced fluorescence in aqueous flows. *Experiments in Fluids*, 10.1007/s00348-008-0496-2.

Crimaldi, J. P. and Koseff, J. R. (2001). High-resolution measurements of the spatial and temporal scalar structure of a turbulent plume. *Experiments in Fluids*, 31(1):90 – 102.

Cruyningen, I. V., Lozano, A., and Hanson, R. K. (1990). Quantitative imaging of concentration by planar laser-induced fluorescence. *Experiments in Fluids*, 10(2-3):41 – 49.

Davidson, M. J. and Wang, H. J. (2002). Strongly advected jet in coflow. *Journal of Hydraulic Engineering*, 128(8):742 – 752.

Dewey, C. (1976). Qualitative and quantitative flow field visualization utilizing laser-induced fluorescence. In *Proceeding of the AGARD conference of non-intrusive instrumentation in fluid flow research*, AGARD-CP-193.

Diez, C., Bernal, L. P., and Faeth, G. M. (2005). PLIF and PIV measurements of the self-preserving structure of steady round buoyant turbulent plumes in crossflow. *International Journal of Heat and Fluid Flow*, 26(6):873 – 882.

Ferrier, A. J., Funk, D. R., and Roberts, P. J. W. (1993). Application of optical techniques to the study of plumes in stratified fluids. *Dynamics of Atmospheres and Oceans*, 20:155 – 183.

Hilderman, T. L. (2004). *Measurement, modelling, and stochastic simulation of concentration fluctuations in a shear flow*. PhD thesis, University of Alberta.

Hussein, H. J., Capp, S. P., and George, W. K. (1994). Velocity measurements in a high-Reynolds-number, momentum-conserving, axisymmetric, turbulent jet. *Journal of Fluid Mechanics*, 258:31 – 75.

Koochsfahani, M. M., Dimotakis, P. E., and Broadwell, J. E. (1985). A "flip" experiment in a chemically reacting turbulent mixing layer. *American Institute of Aeronautics and Astronautics*, 23(8):1191 – 1194.

Larsen, L. G. and Crimaldi, J. P. (2006). The effect of photobleaching on PLIF. *Experiments in Fluids*, 41(5):803 – 812.

Magde, D., Wong, R., and Seybold, P. (2002). Fluorescence quantum yields and their relation to lifetimes of rhodamine B and fluorescein in nine solvents: improved absolute standards for quantum yields. *Photochemistry and Photobiology*, 75(4):327 – 334.

Owen, F. (1976). Simultaneous laser measurement of instantaneous velocity and concentrations in turbulent mixing flows. In *Proceeding of the AGARD conference of non-intrusive instrumentation in fluid flow research*, AGARD-CP-193.

Powell, I. (1987). Design of a laser beam line expander. *Applied Optics*, 26(17):3705 – 3709.

Prasad, R. R. and Sreenivasan, K. R. (1990). Quantitative three-dimensional imaging and the structure of passive scalar fields in fully turbulent flows. *Journal of Fluid Mechanics*, 216:1 – 34.

Saylor, J. R. (1995). Photobleaching of disodium fluorescein in water. *Experiments in Fluids*, 18(6):445 – 447.

Tian, X. and Roberts, P. J. W. (2003). A 3D LIF system for turbulent bouyant jet flows. *Experiments in Fluids*, 35(6):636 – 647.

Walker, D. A. (1987). A fluorescence technique for measurement of concentration in mixing liquids. *Journal of Physics E Scientific Instruments*, 20:217 – 224.

Wang, G. R. and Fiedler, H. E. (2000). On high spatial resolution scalar measurement with LIF - Part 1: Photobleacing and thermal blooming. *Experiments in Fluids*, 29(3):257 – 264.

Zhu, H., Derksen, R. C., Krause, C. R., Fox, R. D., Brazee, R. D., and Ozkan, H. E. (2006). Fluorescent intensity of dye solutions under different pH conditions. *ASTM Special Technical Publication*, (1470):191 – 197.

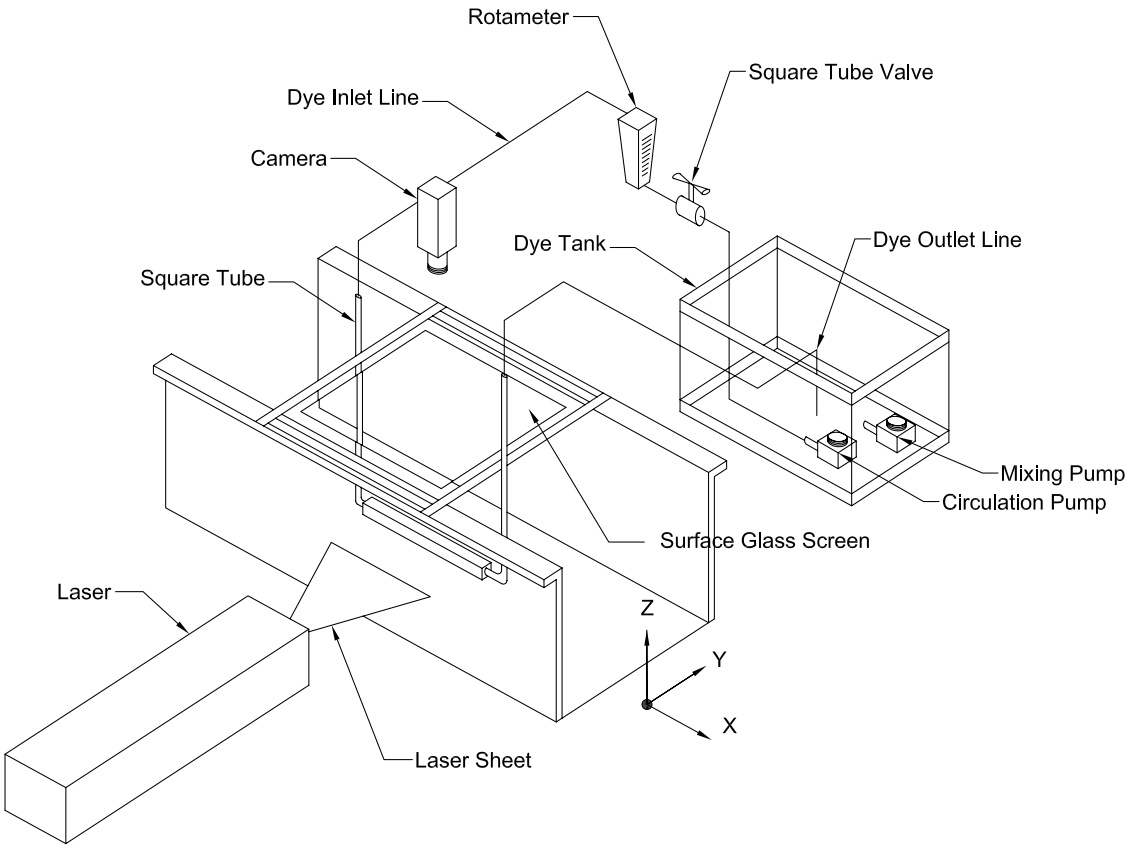

Figure 2.1: Schematic of the experimental setting used to determine the dependance of fluorescence dye intensity on the dyed fluid velocity for different concentrations of fluorescein sodium salt.

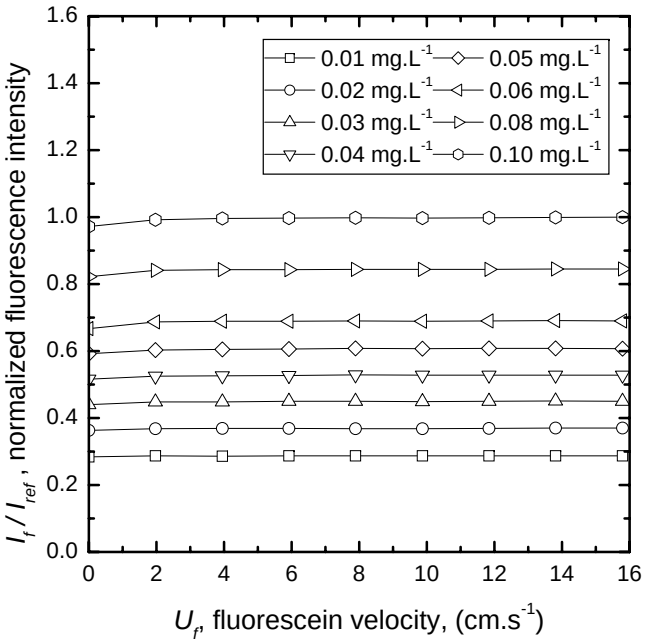

Figure 2.2: Dependance of fluorescence dye intensity (I_f) on the dyed fluid velocity (U_f) for different concentrations of fluorescein sodium salt. The fluorescence dye intensity is normalized by the maximum fluorescence intensity for 0.10 mg.L^{-1}(I_{ref}).

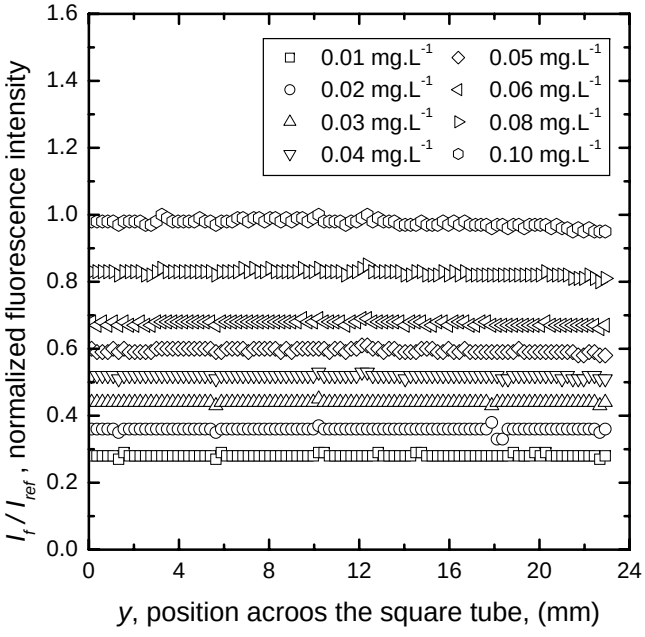

Figure 2.3: Attenuation of fluorescence dye intensity (I_f) along a scan line of the laser sheet for different concentrations of fluorescein sodium salt. The fluorescence dye intensity is normalized by the maximum fluorescence intensity for 0.10 mg.L^{-1}(I_{ref}).

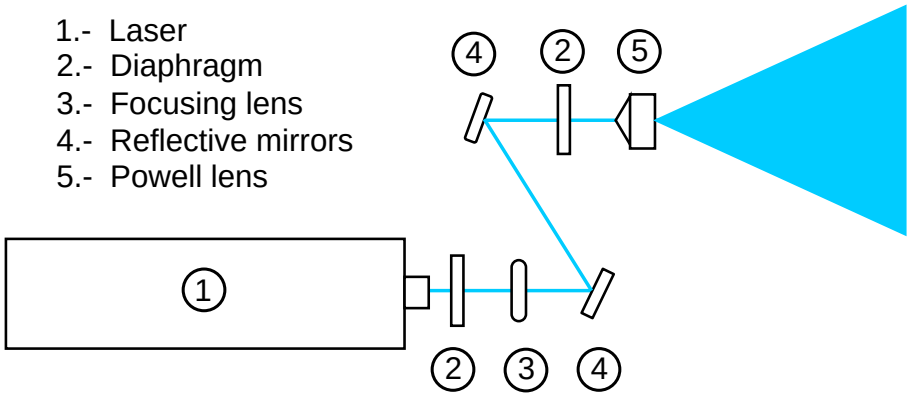

Figure 2.4: Schematic of the optical configuration used to generate the laser sheet. The key component of this configuration is the Powell Lens®.

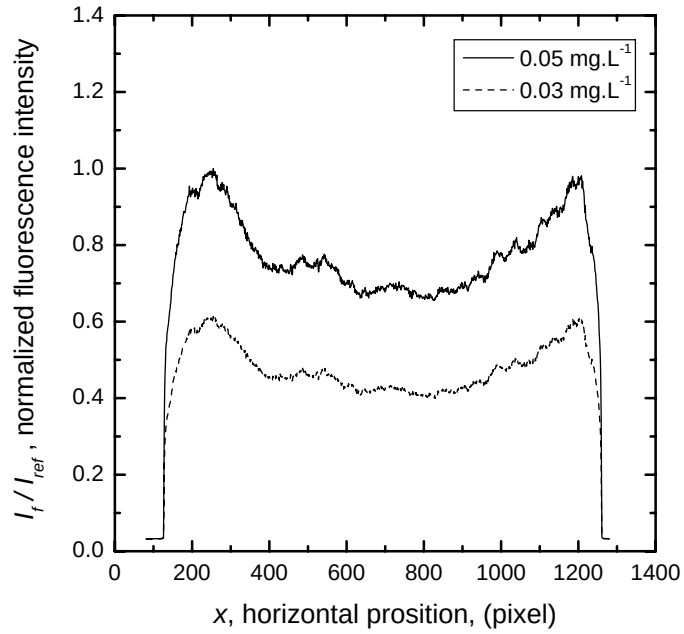

Figure 2.5: Typical laser sheet intensity profiles for two concentration of fluorescein sodium salt. The fluorescence dye intensity is normalized by the maximum fluorescence intensity for 0.05 mg.L^{-1}(I_{ref}).

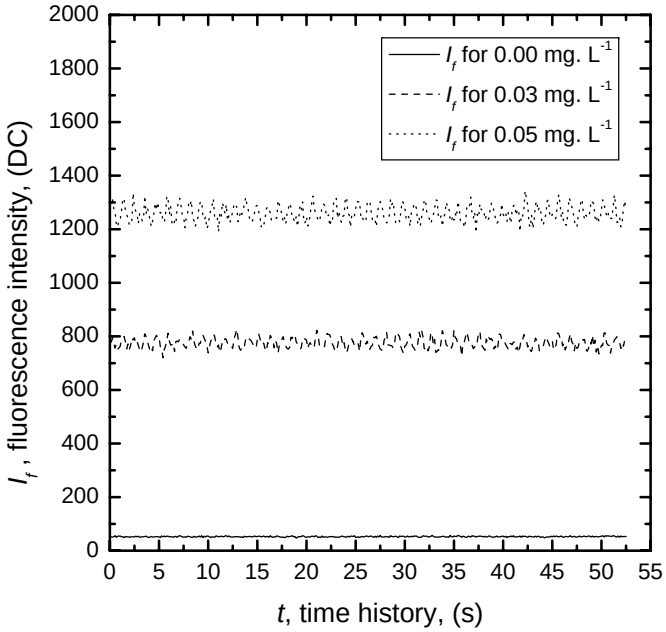

Figure 2.6: Time series of the fluorescence intensity in digital counts for three fluorescein sodium salt concentrations.

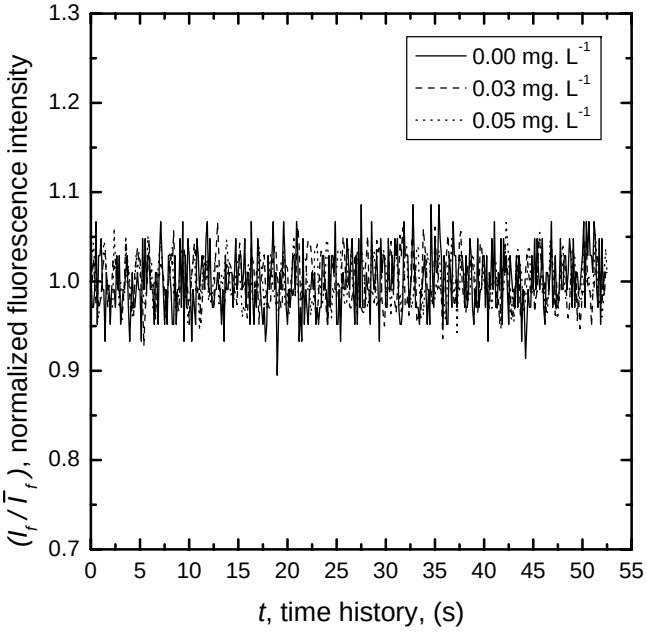

Figure 2.7: Normalized time series of the fluorescence intensity in digital counts for three fluorescein sodium salt concentrations.

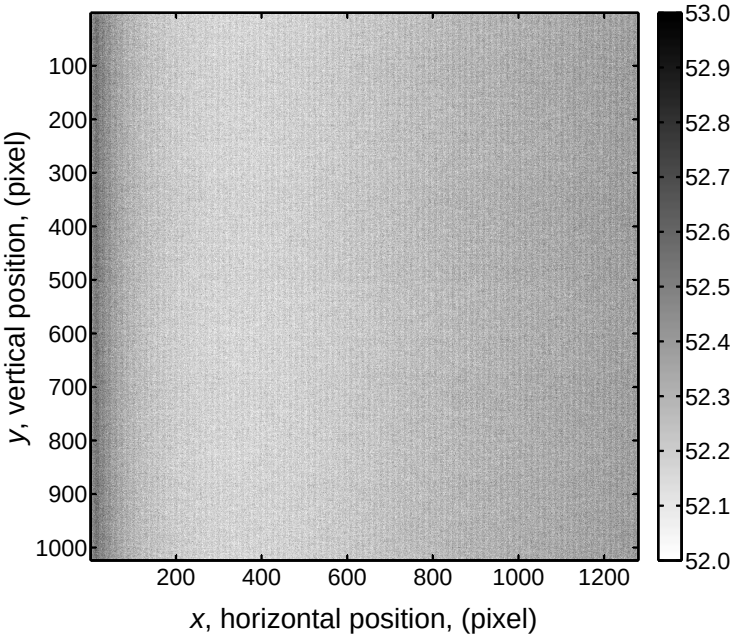

(a)

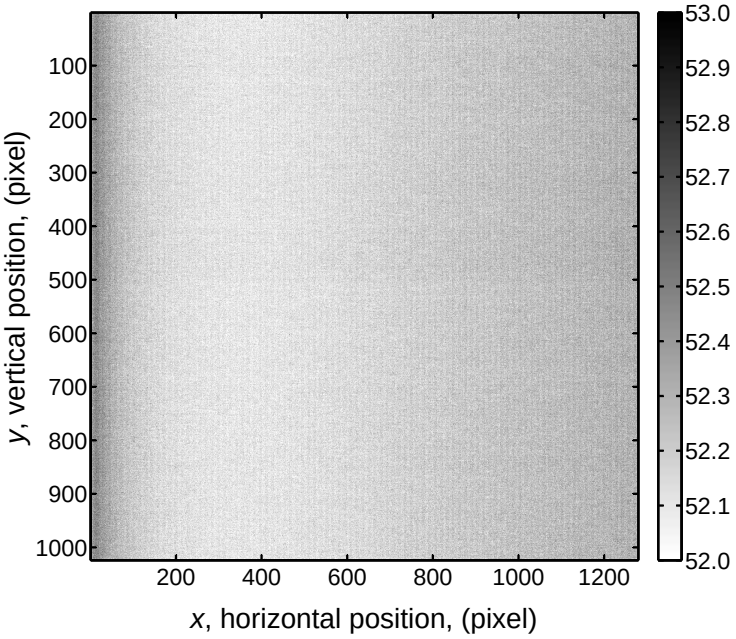

(b)

Figure 2.8: Camera dark response for, (a) camera with no lens and the sensor array covered, and (b) camera with the lens cap on.

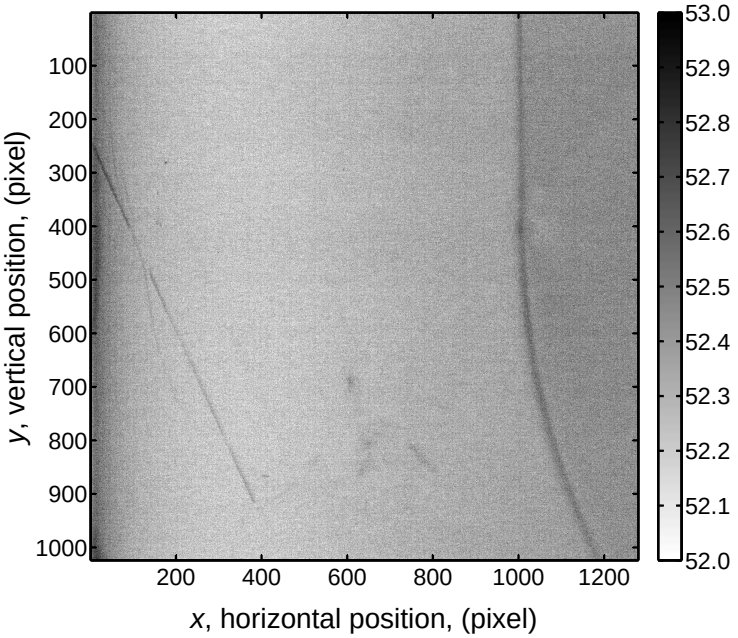

(a)

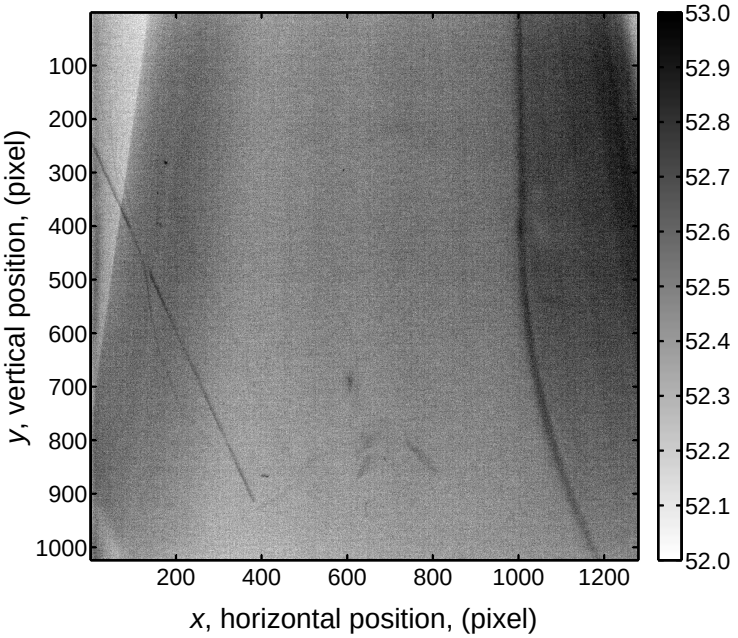

(b)

Figure 2.9: Camera background response for, (a) camera with lens and filter, and (b) camera with lens, filter, and laser on.

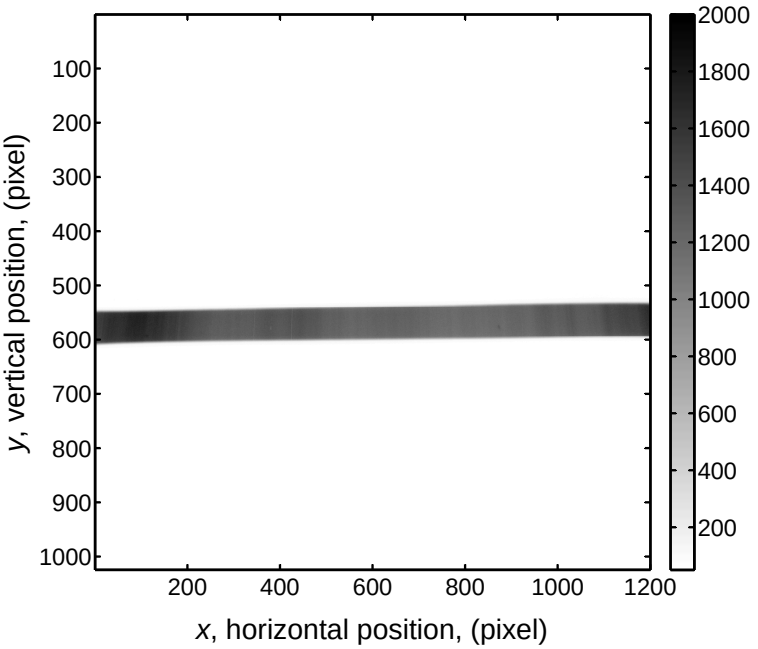

Figure 2.10: Image of one frame of the calibration image sequence used to build the calibration image. The scale shown in the right side of the image corresponds to the I_f in digital counts.

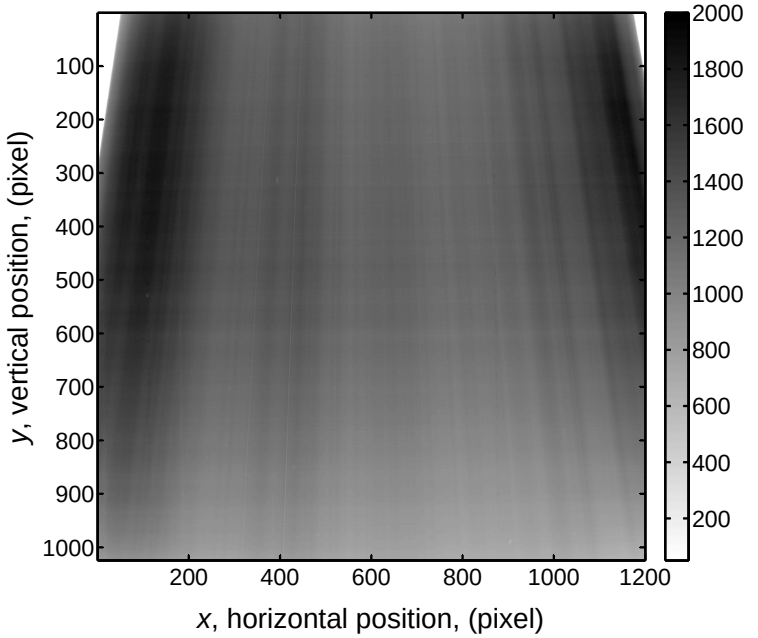

Figure 2.11: Built calibration image obtained from the calibration image sequence (Figure 2.10). The scale shown in the right side of the image corresponds to the I_f in digital counts.

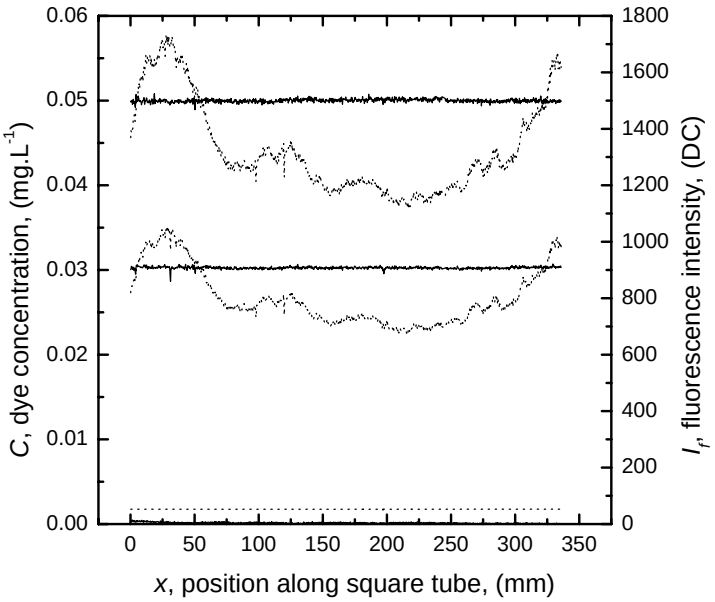

Figure 2.12: Averaged fluorescence light intensity (dotted line) and the corresponding dye concentration (solid line) obtained using the calibration equation (Equation 2.1) along the square tube. Three different concentrations of fluorescein sodium salt were used in this experiment, 0.00, 0.03, and 0.05 mg.L^{-1}.

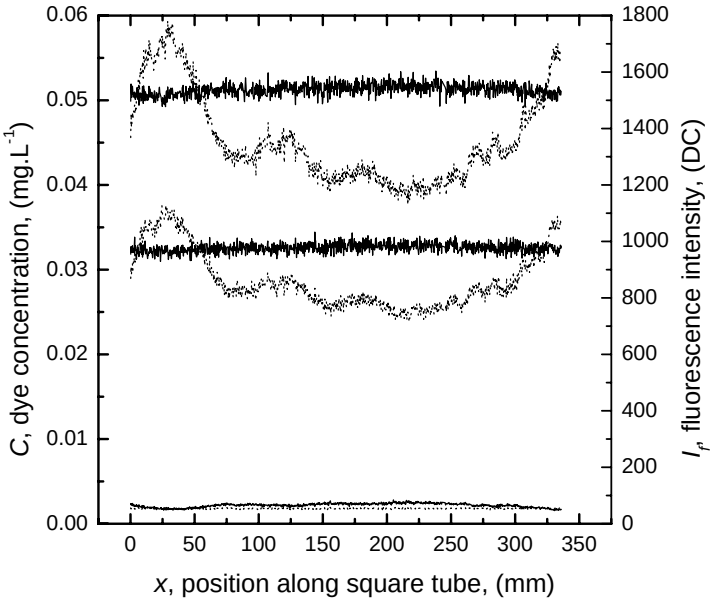

Figure 2.13: Instantaneous fluorescence light intensity (dotted line) and the corresponding dye concentration (solid line) obtained using the calibration equation (Equation 2.1) along the square tube. Three different concentrations of fluorescein sodium salt were used in this experiment, 0.00, 0.03, and 0.05 mg.L^{-1}.

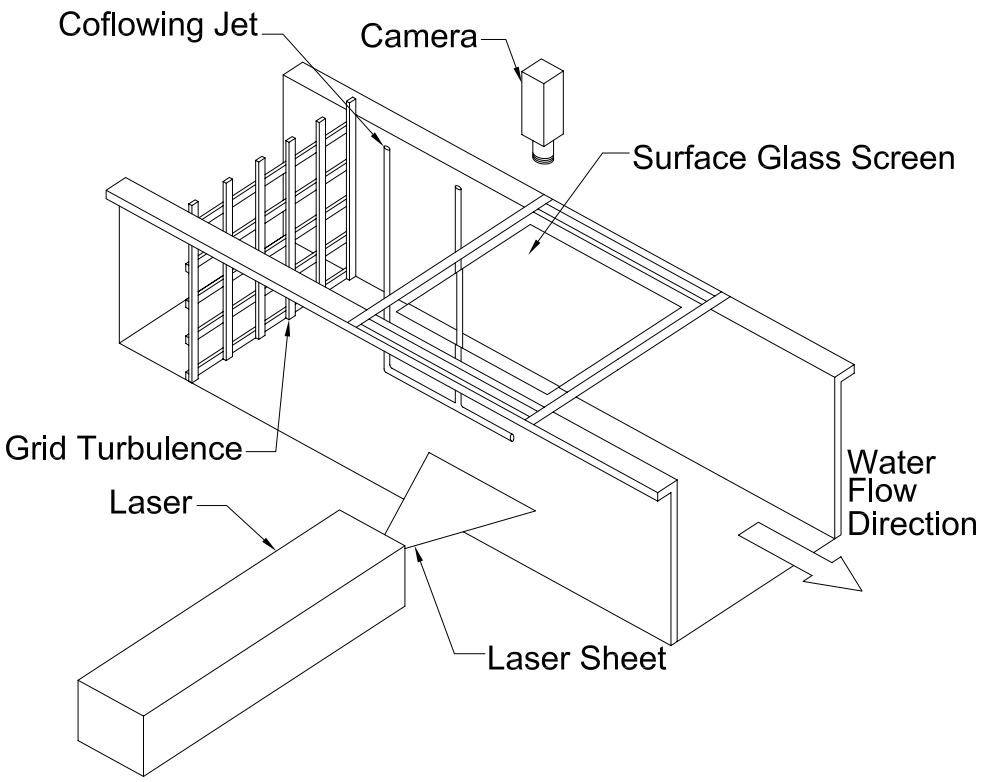

Figure 2.14: Schematic of the experimental set-up used in the application of the developed calibration process to a coflowing jet.

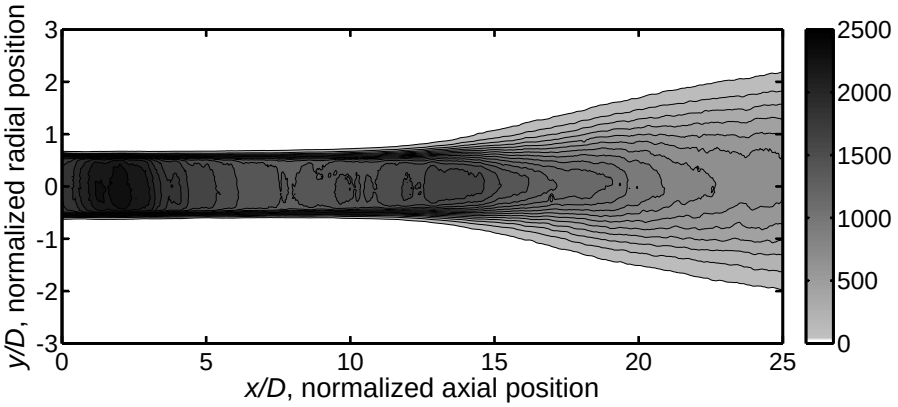

(a)

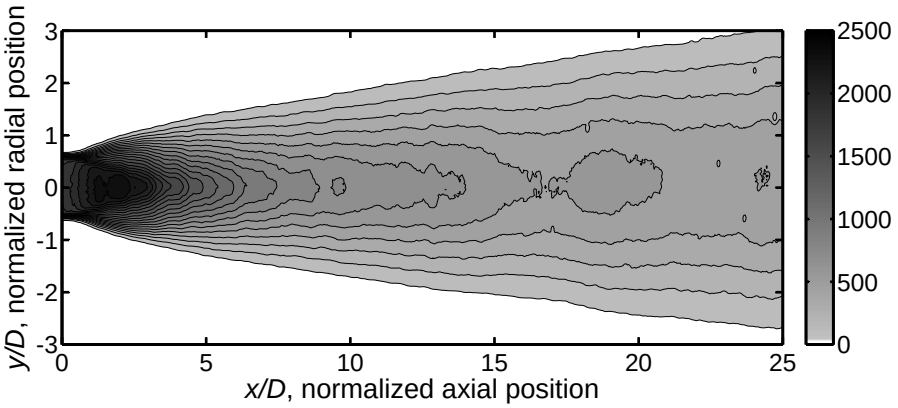

(b)

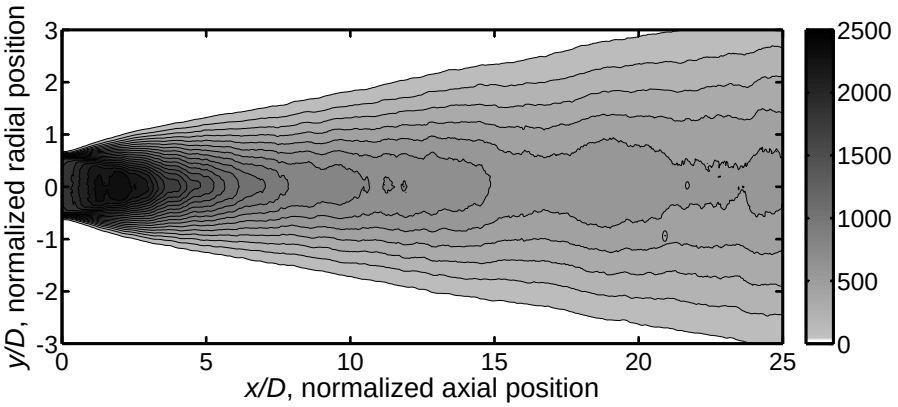

(c)

Figure 2.15: Time averaged light intensity images of the coflowing jet for three jet to coflowing velocity ratios; a) $U_r = 4$, b) $U_r = 8$, and c) $U_r = 14$. Every image was averaged over 1000 frames, approximately 51.8 seconds. Note how uncorrected images can show light intensity structures that do not correspond to concentration field.

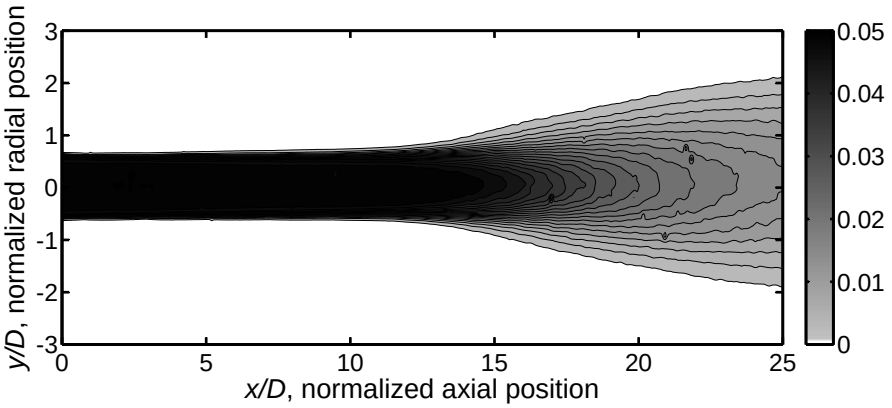

(a)

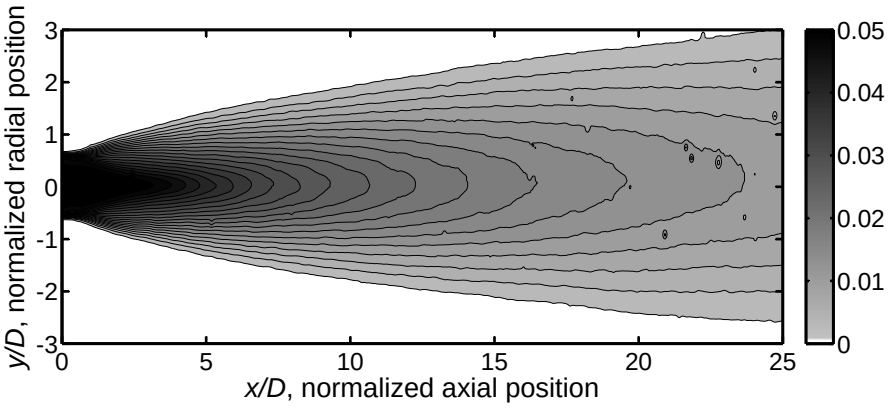

(b)

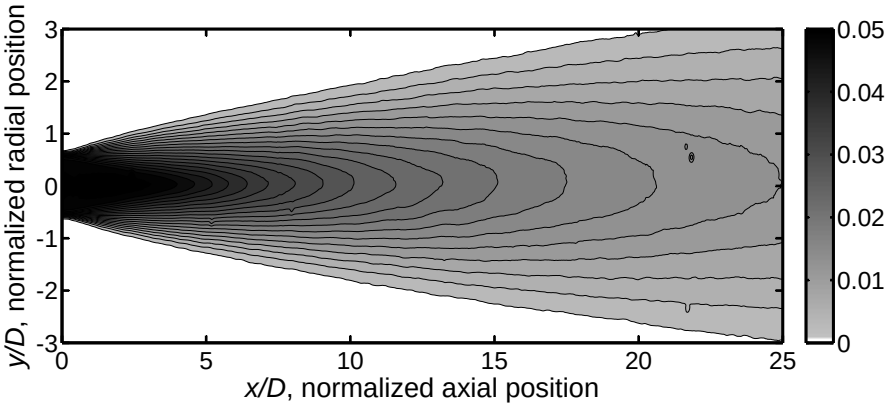

(c)

Figure 2.16: Time averaged scalar concentration field of the coflowing jet for three jet to coflowing velocity ratios; a) $U_r = 4$, b) $U_r = 8$, and c) $U_r = 14$. Every image was averaged over 1000 frames, approximately 51.8 seconds. Note how the light intensity structures shown in Figure 2.12 are corrected by the calibration process.

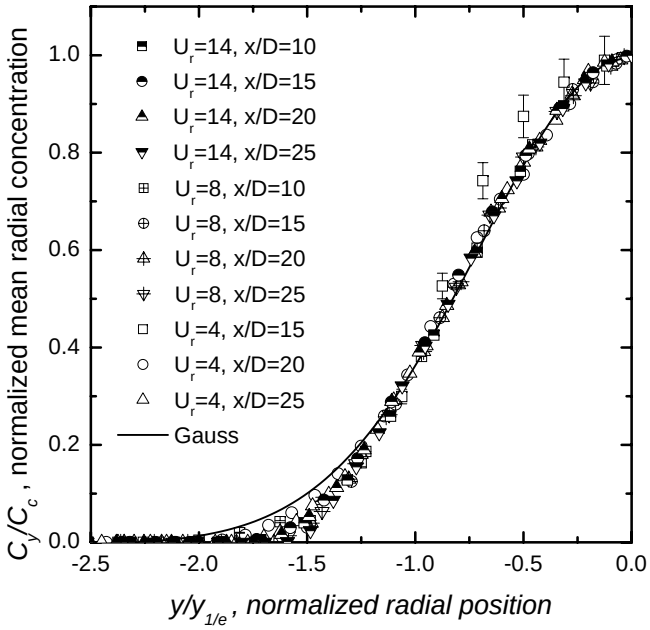

Figure 2.17: Dimensionless radial time averaged concentration profiles of the coflowing jet for three jet to coflowing velocity ratios, $U_r = 4$, $U_r = 8$, and $U_r = 14$.

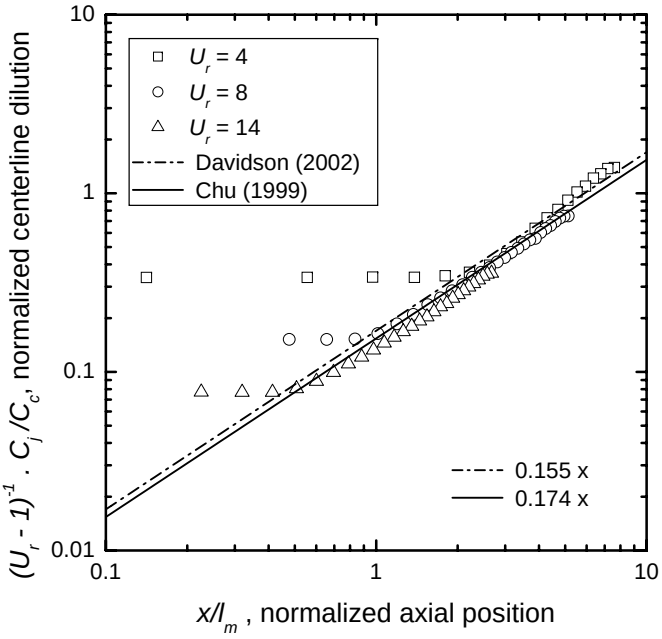

Figure 2.18: Dilution data of the mean axial concentration at three different jet to coflowing velocity ratios. The results compare to the linear variations found by Davidson and Wang (2002) and Chu et al. (1999). The error of the data pints is within the size of the symbols.

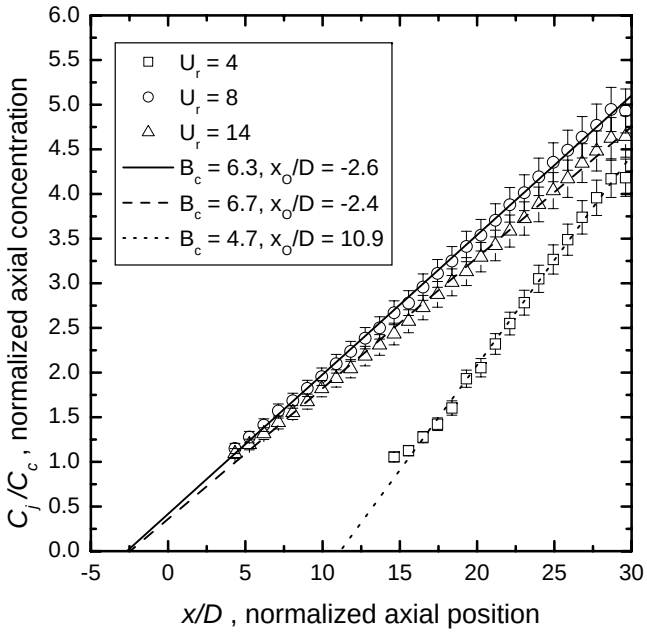

Figure 2.19: Decay of the axial concentration of the coflowing jet for three jet to coflowing velocity ratios, $U_r = 4$, $U_r = 8$, and $U_r = 14$. The functional form of the lines shown in this graph is given by Equation 2.5.

Chapter 3

Centerline concentration of a counterflowing jet: averaged concentration measurements

Abstract

The geometrically similar region of the centerline concentration decay of a counterflowing jet was investigated using planar laser induced fluorescence. The counterflowing jet is defined as a free jet flowing upstream against a uniform counterflow. The jet is investigated for jet to counterflowing velocity ratios (U_r) in the range $4 \leq U_r \leq 19$. New length scales for this flow were studied and used to generate empirical expressions to predict the concentration decay in the established flow zone. These length scales were defined using the 5 % contour of the mean concentration field of the counterflowing jet. Additional experiments for two jet to counterflow velocity ratios were used to validate these empirical expressions. The new empirical expressions correlate well with the concentration decay in the centerline of the counterflowing jet within the free jet-like region. It was found that for some cases, the centerline concentration decay of the counterflowing jet was better predicted considering a decay proportional to $x^{-6/5}$, even though it can also be predicted by assuming a decay with x^{-1}.

3.1 Introduction and Background

Though turbulent jets are probably one of the most studied of shear flows, few investigations on the flow characteristics of a round jet issuing into a uniform counterflow stream apper in the literature (Arendt et al., 1956; Sui, 1961; Timma, 1962; Beltaos and Rajaratnam, 1973; Morgan and Brinkworth, 1976; McDannel et al., 1982; König and Fiedler, 1991b; König and Fiedler, 1991a; Lam and Chan, 1995; Yoda and Fiedler, 1996; Lam and Chan, 1997; Chan and Lam, 1998; Lam and Chan, 2002; Bernero and Fiedler, 2000; Tsunoda and Saruta, 2003). This is true, even considering how counterflowing jets can be found in several industrial and environmental fluid applications (Lam and Chan, 1995). They have been used for the stabilization in afterburners of turbojet engines as well as an enhancer for dispersion and mixing process (Beltaos and Rajaratnam, 1973; Chan, 1999).

The mean flow geometrical parameters for a counterflowing jet are shown in Figure 3.1. The flow of a counterflowing jet is generated by a nozzle of diameter D with a velocity U_j, and in some cases the jet carries a scalar concentration (C_j). Once the jet is in contact with the uniform counterflow stream, with velocity U_o, the mixing process begins.This mixing process creates a decay of the concentration downstream the exit of the jet. In this process there is a momentum exchange, where the uniform counterflow stream is able to stop the flow of the jet that is then carried back with the counter current (Yoda and Fiedler, 1996). The distance from the exit of the jet to the point where zero velocity is reached is known as the jet penetration length (x_p), which also defines the location of the stagnation streamsurface at the centerline of the jet.

Figure 3.1 also shows three regions downstream from the jet exit. The zone of flow establishment (ZFE) contains the iso-concentration core and the transition to the established flow region (EFR). In the EFR the jet flow is the dominant flow and the counterflowing jet behaves similar to a free jet in quiescent surrounding (König and

Fiedler, 1991b; Beltaos et al., 1999; Yoda and Fiedler, 1996). Finally, one can see the mixing zone (MZ) where the flow is dominated by the counterflow stream.

Among the few investigations carried out related to the counterflowing jet, the penetration distance and the centerline velocity decay have been the primary focus. The axial penetration distance of a counterflowing jet has been sufficiently studied for different jet to counterflow velocity ratios (U_r). The studied values of U_r go from 1.3 to 15 (Beltaos and Rajaratnam, 1973; Morgan and Brinkworth, 1976; König and Fiedler, 1991b; Yoda and Fiedler, 1996; Lam and Chan, 1997). These investigations lead to the conclusion that the jet penetration was governed by U_r. It was found that the penetration length had a linear relationship with the velocity ratio. Morgan and Brinkworth (1976) established that this linear relation between the jet penetration and the velocity ratio is valid just for velocity ratios within the "low momentum region". This region is found where the ratio of momentum fluxes is less than 0.5, for higher ratios of momentum fluxes the relationship between jet penetration and velocity ratio is not longer linear. Beltaos and Rajaratnam (1973) studied the velocity scale along the centerline of the counterflowing jet using the penetration length (x_p) as the geometrical scale for the axial velocity decay. Using x_p as the axial scale for the velocity Beltaos and Rajaratnam (1973) demonstrated that the profiles of the centerline velocity collapsed on a single curve for jet to counterflow velocity ratios higher than 4. In the discussion presented by Beltaos et al. (1999) it was found that this universal form of the centerline velocity decay was valid just for axial distances greater than half the total jet penetration, a finding that was supported by the investigation of Chan and Lam (1998). Chan and Lam (1998) presented an investigation of the centerline velocity decay of a counterflowing jet where an analytical model was presented to predict the centerline velocity based on the conservation of mass flux and momentum flux. An analytical model was also presented by Chan (1999) for the centerline concentration decay of a counterflowing jet; this model was obtained based on the velocity field of the counterflowing jet. To the knowledge of the author, no further attempt has been made in order to define new length scales for the centerline

concentration decay in a counterflowing jet.

Therefore, this chapter presents a study on new length scales for the centerline concentration decay of the counterflowing jet throughout planar laser induced fluorescence. Forms of the aspect ratio of the 5 % contour are used as length scales for the centerline concentration decay. These scaling factors are used to generate simple empirical expressions to predict the concentration decay of the counterflowing jet. These expressions are validated with additional experimental data of the mean concentration field of the counterflowing jet.

3.2 Experimental Setup and Techniques

The experiments were carried out in a closed loop water channel facility in the Mechanical Engineering Department at the University of Alberta. The water channel has a cross section of 680 mm wide by 480 mm high, the total length of the water channel is approximately 5000 mm. The jet was produced by using two cylindrical nozzles with an internal diameter of 8.841 and 5.64 mm, hereafter referred to as D_1 and D_2 respectively. These jets were fed from a pressurized stainless steel tank, the gauge pressure in the tank was kept constant at 206.84 kPa. Both jets were designed to have an inlet length of 104D with the aim of having a fully developed flow. The velocity of the jet was controlled by a valve located far upstream the inlet of the jet. A calibrated rotameter was installed at the inlet line of the jet in order to monitor the desired jet velocity, the calibration curves for the different jets diameters can be found in Figure B.1. The counterflowing jet was located at the center of the test section. The test section was located 3200 mm downstream from the inlet of the water channel. The jet was set at approximately 200 mm from the bottom of the water channel in the test section, and the level of water was kept constant at a height of 400 mm for all the experiments. Different jet to counterflow velocity ratios were tested for the two jet diameters, the velocity of the counterflow stream was kept at a constant value of 5 cm.s^{-1} as the velocity of the jet was adjusted to obtain the desired

jet to counterflow velocity ratio. Table 4.1 summarizes the initial jet condition used in the experiments.

Table 3.1: Initial jet conditions for every experiment of the scalar concentration measurements.

D (mm)	U_j (m.s^{-1})	U_r	Re_D
8.81	0.18	4	1580
8.81	0.38	8	3330
8.81	0.53	11	4640
8.81	0.62	12	5430
8.81	0.67	14	5870
5.64	0.38	8	2130
5.64	0.53	11	2970
5.64	0.68	14	3810
5.64	0.81	16	4540
5.64	0.94	19	5270

A uniform grid was place at the inlet of the water channel (see Figure 2.14) built with flat stainless steel bars of 19.2 by 5 mm of cross section area. The total open area was approximately 56 % with a mesh spacing of 76.2 mm. This grid turbulence generates near uniform velocity profile for the streamwise component, with variations found to be within 5 % (Hilderman, 2004). At the test section the turbulence intensity was found to be about 4 % for the mean horizontal (Hilderman, 2004).

The axial (x) mean scalar concentration fields were measured using planar laser induced fluorescence. The dye used for the scalar concentration measurements was fluorescein sodium salt, this dye was added and mixed in the stainless steel tank used to feed the nozzle. The concentration used in all the experiments was 0.05 mg.L^{-1}. The planar laser induced fluorescence system uses an optical arrangement that includes a Powell lens® to generate an approximately uniform thin laser sheet (Powell, 1987). Figure 3.2 depicts the experimental set-up used at the test section. A glass screen placed on the free surface was used to avoid any distortion due to the small waves. The camera was placed at approximately 1200 mm from the axis of the jet.

The laser used in this investigation was a 2.1 W Argon ion laser, which was operated in a single mode at a wavelength of 488 nm. A calibration process was employed before every experiment in order to obtain the scalar concentration field out of digital imaging analysis. Calibration images were obtained by traversing a glass square tube with a known dye concentration along the field of view of the camera while a set of images were being taken. The final calibration images were obtained by taking the average value of the sequence of instantaneous images at the known concentration. A linear fit was used to convert the fluorescent intensity into scalar concentration data (a detailed explanation of the calibration process can be found in Chapter 2). Instantaneous concentration images were recorded using a 12 bit SensiCam high speed CCD system, with a resolution of 1280 x 1024 pixels. At every flow jet condition a set of 500 images as taken at a rate of 19.32 Hz, with the exposure time used in each images of 10 ms. The spatial resolution established for the experiments was approximately 0.3 mm.pixel^{-1}.

3.3 Experimental Results

Average concentration field graphs were obtained by assembling the instantaneous concentration field images, Figures 3.3 and 3.4 depict the time averaged counterflowing jet images for jet to counterflow velocity ratios (U_r) of 4, 8, 11, and 14 for the case of large jet diameter (D_1). Based on previous investigations it is expected that the mean axial penetration of the jet increases proportionally with the jet to counterflow velocity ratio (Rajaratnam, 1976; König and Fiedler, 1991b). Figure 3.5 depicts x_p plotted as a function of U_r. The data shown in this graph correspond to four different experiments, three of the which were done using a jet with diameter D_1 and one with D_2. From Figure 3.5 it is possible to appreciate that the data fit relatively well the linear relation presented by Rajaratnam (1976) and Yoda and Fiedler (1996). Rajaratnam (1976) define the maximum penetration of the the jet as the point of the stagnation surface at the axis of the jet, meanwhile Yoda and Fiedler (1996) defined x_p as the maximum axial penetration distance of the mean fluorescence intensity field.

In this investigation the maximum extension of the 5 % jet concentration contour at the centerline of the jet was observed to agree with the linear relation found by Rajaratnam (1976) and Yoda and Fiedler (1996). Therefore, the geometrical length and scaling factors were defined using the contour of the 5 % concentration at the exit of the jet nozzle.

The geometric length parameters in the jet were computed by considering the 5 % contour of the concentration at the exit of the jet. An example of the measurements for the different geometrical lengths for the counterflowing jet is given in Figure 3.6. In this figure it is possible to observe that the shape of the 5 % contour is not symmetric along the axis of the jet, therefore, the maximum lateral penetration is not the same in both directions, the maximum discrepancy was found to be approximately 20 % for the worst case. Consequently, the value of y_p will be determined by considering the average of the maximum penetration in both directions, this is the maximum half-width of the 5 % contour.

The velocity ratios studied were contained within the "unstable case" defined by König and Fiedler (1991b), this is, for U_r greater than 1.4. In fact, some fluctuations of the jet were observed during the execution of the experiments. These fluctuations were found to be presented along, around, and across the axis of the jet, and were also pointed out in the studies presented by Yoda and Fiedler (1996) and Lam and Chan (1997). One can assume that these fluctuations are caused by the exchange of momentum between the jet flow and the counterflow stream. This exchange of momentum slows the jet, that is stopped and finally convected in the direction of the counterflow stream. The fluctuations along the axis of the jet were observed through the execution of the experiments, and the larger variations were found for greater values of U_r. For instance, at $U_r = 14$ the axial penetration of the jet was found to fluctuate between 20D and 44D for a mean axial penetration of 40D. It is possible to appreciate that instantaneous axial penetrations can be up to 51 % shorter than the mean penetration. Throughout the experiments it was possible to observed that the shortest axial

penetration was registered when the jet was bent out of the plane of the laser as well as a few times in the same plane. Figure 3.7a depicts an example of a bent jet in the same plane of the laser sheet which corresponds to the shortest axial penetration of the jet for $U_r = 8$. The longest instantaneous penetration was found to be approximately 20 % of the mean penetration. The longest instantaneous penetration was found usually when the jet flow was able to penetrate into the counterflow stream following an approximately straight path, which can be seen in Figure 3.7b.

Figure 3.8 depicts the centerline concentration decay for the counterflowing jet with a nozzle diameter of 8.81 mm. From this figure it is possible to appreciate the different length of the established flow region in the counterflowing jet its relationship with U_r. The iso-concentration core region is characterized by having an approximately constant value. In the experimental data shown in this figure, a transition region between the zone of flow establishment and the established flow region is observed. Indicating that the established flow region began at approximately 6 diameters downstream from the exit of the jet (see Figure 3.10). The centerline concentration decay shows a change in the decay rate of the axial concentration, which begins at the location corresponding to the maximum lateral penetration, for instance . This axial distance was defined as x_b. It would appear that at this point the overall behavior changes from a free jet regime to a mixing stagnation region. In the mixing region the counterflow stream is considered to be the dominant flow. This transition region can be also observed in Figure 3.9. The dilution of the centerline concentration of the counterflowing jet with nozzle D_1 is shown in Figure 3.9. In this figure the inverse of the normalized mean axial concentration decay (C_j/C_c) is plotted against the normalized axial location (x/D). Profiles of the dilution in the centerline of the jet are obtained for jet to counterflowing velocity ratios: 4, 8, 11, 12, and 14. The dashed line in the graph shows the 0.25 slope experimentally found by Yoda and Fiedler (1996) for $x/D \leq 10$. However, for a larger downstream distance, a slope of 0.30 (solid line) seems to be more representative of the dilution for the mean centerline concentration. Nevertheless, it is evident that in the counterflowing jet the dilution of the centerline

occurs faster than the jet in a quiescent stream for which the slope is found to be about 0.20 (Dahm and Dimotakis, 1990). Lam and Chan (2002) suggested that a rough collapse of the data into a single curve is observed if C_j/C_c is plotted against x/x_p. With the data available in this investigation, the collapse of the profiles into a single curve was not observed. Figure 3.9 shows that the dilution of the mean concentration is stronger for the low value of U_r, on the other hand, when the velocity ratio U_r is higher, the dilution in the axial concentration resembles the dilution for a free jet.

Mean concentration values along the axis of the jet are plotted in Figure 3.10. In this figure the value of the axial concentration is normalized by the concentration at the exit of the jet (C_j) scaled by the velocity ratio, and plotted against the normalized axial position of the jet. The axial position along the axis of the jet was normalized by the diameter of the jet. Figure 3.10 shows the variation of the jet penetration with U_r. The scaled concentration profiles depict in a more easy manner the "free jet-like" region, for which the counterflowing jet behaves similar to an ordinary jet (König and Fiedler, 1991b; Beltaos et al., 1999; Yoda and Fiedler, 1996). This free jet-like region is defined as the region for which the jet flow is the dominant flow, and its length extends up to approximately 70 % of the total penetration length of the jet (Lam and Chan, 2002). Data collected show that the length of the free jet-like region coincides in most of the experiments with the axial position of the maximum lateral penetration of the jet x_b. The average value of x_b was found to be 69 % of the total penetration length of the jet, the corresponding data can be seen in Table 3.2.

Beltaos and Rajaratnam (1973) suggested that the measurements of the centerline velocity decay of the counterflowing jet collapse on to a single curve for $U_r > 4$ when the axial velocity is plotted using the form

$$\frac{U + U_o}{U_j}\frac{x_p}{D} = f\left(\frac{x}{x_p}\right) \tag{3.1}$$

where U is the centerline value of the velocity. This equation indicates that the

Table 3.2: Penetration distance, length of the established flow region, and lateral penetration of 5 % contour of the jet.

Jet Nozzle	U_r	x_p/D	y_p/D	y_p/x_p	x_b/x_p
8.81 mm	4	16.50	4.21	0.26	0.60
	8	25.00	6.50	0.24	0.68
	11	31.67	7.09	0.22	0.69
	12	34.75	7.56	0.22	0.71
	14	42.00*	9.44	0.23	0.70
5.64 mm	8	20.25	5.50	0.27	0.66
	11	27.25	5.94	0.24	0.66
	14	31.50	7.50	0.24	0.76
	16	43.75	8.38	0.19	0.75
	19	51.50	6.88	0.13	0.71

* This value of x_p was estimated by assuming that x_b was approximately 70 % of the jet penetration, the maximum penetration of the jet for this flow condition was out of the field of view of the camera.

maximum penetration length of the counterflowing jet can be used as the length scale of the centerline concentration decay. However, for the case of the concentration field, the concentration of the counterflow stream is zero. Therefore, Equation 3.1 is written as

$$\frac{C_x}{C_j}\frac{x_p}{D} = f\left(\frac{x}{x_p}\right) \tag{3.2}$$

Figure 3.11 depicts the centerline concentration profiles for the counterflowing jet represented by Equation 3.2. Figure 3.11 shows that the universal form of the axial concentration decay for the counterflowing jet is a good representation for $x/x_p \geq 0.5$ (50 % of the jet penetration). Beltaos and Rajaratnam (1973) indicated that for $U_r > 4$, the data follow a decay proportional to x^{-1}. The function presented by Beltaos and Rajaratnam (1973) is also shown in Figure 3.11. It is important to mention that the function given by Beltaos and Rajaratnam (1973) was generated using the velocity, therefore, this function should not follow the data of the concentration field, the best fit of the data is given by

$$\frac{C_x}{C_j}\frac{x_p}{D} = 3.9\left(\frac{x}{x_p}\right)^{-1} \tag{3.3}$$

The centerline concentration is proportional to x^{-1} as can be observed in Figures 3.10 and 3.11. Even though the curve described in Equation 3.3 shows a better fit for the data, it collapses nice into a single curve for $x/x_p \geq 0.5$. Figure 3.11 shows that the experimental data of the centerline concentration decay collapses into a single curve just for $x \geq 0.5x_p$. Similar results were found in the investigation presented by Chan and Lam (1998). In this investigation was indicated that the centerline velocity decay collapses into a single curve for a short part of the total jet penetration of the counter-flowing jet when it was plotted using Equation 3.1. Therefore, the universal form of the centerline velocity decay is valid for values of x within this range. Although, the function given by Equation 3.2 does not represent a universal curve of the centerline concentration decay it is clear that axial concentration decays proportional to x^{-1} for the range of U_r studied in this investigation.

The maximum half-width of the 5 % contour can be considered as an important scale for the centerline concentration decay. For a conserved scalar would be logical to expect that a higher lateral spread rate would result in a steeper decay in the centerline concentration. To test this, the maximum half-width of of the 5 % contour (y_p) was used instead of the maximum axial penetration length (x_p) in Equation 3.2. Figure 3.12 shows the data of the nozzle of diameter D_1 plotted using the form

$$\frac{C_x}{C_j}\frac{y_p}{D} = f\left(\frac{x}{x_p}\right) \tag{3.4}$$

Figure 3.12 shows the data for the centerline concentration decay collapsing into a single curve for $x/x_p \geq 0.2$. The collapsing range of the centerline concentration shown in this figure, is significantly larger than the one observed in Figure 3.11. The universal form given by Equation 3.4 was found to be valid just for a limited range of U_r. As can be seen in Figures 3.12 and 3.13, this range is limited by $8 \leq U_r \leq 16$. It is clear from Figure 3.13 that the trend of data for the $U_r = 19$ does not drop into

the same curve as is the case of $U_r < 19$. Additionally, it is possible to observe that the equation of the similar curve is not the same as the one as in Figure 3.12. The similar region shown in Figure 3.12 is found to be valid for an axial distance in the range of $0.2 \leq x \leq 0.7$. Within this region, the decay of the centerline concentration was determined to be proportional to $x^{-6/5}$. However, a decent approximation of the axial decay is obtained if the centerline concentration is considered to decay with x^{-1}, which can be seen in Figure 3.12. The fact that the universal form given by Equation 3.4 is not valid for $U_r = 19$ can be explained by looking at the value of the maximum half-width lateral penetration (y_p). From Table 3.2 it is possible to observe that for $U_r = 19$ the value of y_p shows a sudden drop, affecting the similarity of the concentration profiles in Figure 3.13. This suggests that y_p is not the ideal scale for the centerline concentration decay. This would suggest that a relation of the maximum half-width penetration and the maximum axial penetration would be better suited scales for the centerline concentration decay in a counterflowing jet.

Table 3.3 contains the different length ratios for some of the performed experiments. These ratios were used to generate several self similar curves of the centerline concentration decay for the counterflowing jet. In order to simplify the notation new parameters were defined, these are, λ, β, and ϕ, which correspond to y_p/x_b, y_p/x_p, and x_b/x_p respectively. Using these new parameters, it was possible to define new axial distances, for instance x_λ was defined as the axial position for which the centerline concentration was equal to λ times the concentration at the exit of the nozzle of the jet. In similar form the axial distances x_β and x_ϕ were also defined.

Figure 3.14 and Figure 3.15 show the centerline profiles of the concentration decay for the counterflowing jet when these are plotted using the parameters λ and β as the scale of the centerline concentration decay. These profiles were obtained using the parameters λ and β instead of x_p/D in Equation 3.2. Figure 3.14 shows that for velocity ratios equal or higher than 8, the different centerline concentration profiles collapse into a single curve independent of the initial conditions of the jet. In these

Table 3.3: Geometrical scale length using the jet penetration (x_p), maximum half-width lateral penetration (y_p), and the axial location of the maximum lateral penetration (x_b).

Diameter	U_r	y_p/x_b	y_p/x_p	x_b/x_p
8.81 mm	4	0.40	0.23	0.58
	8	0.35	0.24	0.68
	11	0.32	0.22	0.70
	12	0.31	0.22	0.71
	14	0.32	0.23	0.70
5.64 mm	8	0.41	0.27	0.66
	11	0.36	0.24	0.66
	14	0.31	0.24	0.76
	16	0.25	0.19	0.75
	19	0.19	0.13	0.71

figures it is possible to observe that the centerline concentration decays with $x^{-6/5}$. Nevertheless, similar to the case depicted in Figures 3.12 and 3.13 the axial decay can be approximated by considering a decay proportional to x^{-1}. Therefore, it is possible to suggest that the use of λ as a scale for the axial concentration decay offers better results than by using y_p/D and x_p/D. It is important to mention that the data that most departs from the fitted curve corresponds to U_r =14 for which the penetration length x_p was estimated and not experimentally measured, because this axial penetration was out of the range of the camera field of view. A similar behavior of the centreline concentration is observed in Figure 3.15. It can be seen that the scatter of the data when β is used as the scaling factor is significantly higher than for the case of λ. However, the trends of data in Figure 3.15 demonstrate a similar shape for the different jet-to-counterflowing velocity ratios. It is clear from Figure 3.15, that the centerline decay for the counterflowing jet is proportional to the inverse of the axial distance.

The parameters λ and β were used to define forms for which the centerline concentration profiles show a similar behavior within the established flow region. Figures 3.16 and 3.17 show the data of the axial concentration profile collapsing on a single curve.

In these figures, the location of the concentration along the axis of the jet was normalized by the axial distance where the normalized centerline concentration was equal to λ and β times the concentration at the exit of the jet, for Figure 3.16 and Figure 3.17 respectively. In these figures the normalized centerline concentration decay was scaled by the inverse of the length ratios λ and β. Figures 3.16 and 3.17 depict the centerline concentration decay of a counterflowing jet collapsing very nicely onto a single curve. It is possible to see that the decay of the axial concentration can be considered to be inversely proportional to the axial distance x. However, it was found that this concentration decay is better predicted by $x^{-6/5}$, shown as a dashed line in Figures 3.16 and 3.17. From the experimental data studied in this investigation the established flow region was found to be located at approximately 6D downstream of the exit of the jet. At approximately 6D, the concentration value of the jet was about 70 % of the concentration at the nozzle, therefore, it is possible to state that the form of the centerline concentration shown in Figure 3.16 and Figure 3.17 is valid for a significant portion of the zone of established flow. This dimensionless form of the axial concentration fits the experimental data for concentration values between 85 to 11 % of the concentration at the exit of the jet. Note that the zone of established flow is not found immediately after the iso-concentration core zone, in fact, there is a transition region between the iso-concentration core and the zone of established flow (Chan and Lam, 1998).

The parameter ϕ was also used to generate a universal form of the centerline concentration decay for the counterflowing jet, in a similar way that λ and β were used; the results of which can be observed in Figure 3.18. It can be seen that similar to the outcomes obtained in Figure 3.16 and Figure 3.17, the axial concentration decay for the different jet to counterflowing velocity ratios collapsed onto a single curve. Nonetheless, this novel form for the centerline concentration was proven to be conditional upon the inlet condition, since the same result was not obtained for the case of the smaller jet diameter. Therefore, only the results obtained for the larger jet diameter are shown in Figure 3.18.

Another function form for which the centerline concentration decay shows a similarity region was proposed by Lam and Chan (1995). It was suggested that the stagnation surface or dividing surface, as was defined by the authors, was located at the brightness contour for which $L_p = e^{-1}L_m$, where L_m was considered to be the maximum intensity level at the center of the "bright patch" observed in the experiments of this investigation, which was located approximately at the center of the concave shape of the stagnation surface. It is important to point out that the work of Lam and Chan (1995) had similar intent, however, they did not base their findings on calibrated concentration measurements, but on light intensity. The light intensity observed is not directly proportional to scalar concentration as it may be biased by pixel sensitivity, camera field non uniformity and high laser sheet heterogeneity. However, there is a difference between the criterion presented by Lam and Chan (1995) and the one used in this study. Instead of using the location of the intensity contour where the intensity was equal to e^{-1} times the intensity of the "bright patch", we used the location for which the centerline concentration was equal to e^{-1} times the concentration at the exit of the jet. This axial position was defined as $x_{_{1/e}}$. Figure 3.19 depicts the centerline concentration decay of the counterflowing jet against the axial position normalized by the parameter $x_{_{1/e}}$. It can be seen that the axial concentration profiles for different U_r are similar when the axial position of the centerline concentration is normalized by $x_{_{1/e}}$ for U_r greater than 4. In Figure 3.19 we can observe that a single power law fits relatively well to the experimental data. It is possible to state that the normalized concentration follows the function

$$\frac{C_c}{C_j} = 0.35 \left(\frac{x}{x_{_{1/e}}}\right)^{-1} \tag{3.5}$$

In order to completely define the centerline concentration decay for the counterflowing jet, it is important to discus how the new parameters (λ, β) and the new axial distances (x_λ, x_β, and $x_{_{1/e}}$) are related with the jet to counterflowing velocity ra-

tio. Figure 3.20 shows the variations of λ and x_λ with U_r. A linear regression was performed and it was found that the available data responded to a linear relation with U_r. The correlation coefficient found for both the linear regressions were 0.95 and 0.91 for the case of λ and x_λ respectively. It is important to mention that the linear fit obtained for x_λ was forced to go through zero in order to satisfy the physical meaning of this parameter. It can be seen that most of the data drops into the 95 % confidence line shown in Figure 3.20 (dashed line). Figure 3.21 depicts the parameters β and x_β as function of U_r. It can be appreciated that the data shown in this graph can be approximated by a linear function of U_r. The R^2 found for the function that represents a β and x_β were found to be 0.90 and 0.88 respectively. It can be seen from Figure 3.21a that a nonlinear fit can be used to better represent the parameter β as a function of U_r. However no significant improvement in the prediction of the centerlines concentration was observed when using a nonlinear fit (data not presented in this investigation). Similar to x_λ and x_β, the axial position $x_{_{1/e}}$ was found to have a linear dependance on U_r, as can be seen on Figure 3.22. This linear fit has a R^2 of 0.90, therefore it is possible to state the this linear relation represents the real data relatively well.

Since λ, β, x_λ, x_β, and $x_{_{1/e}}$ can be related with U_r, experimental equations can be generated in order to predict the centerline concentration decay for the counterflowing jet. The experimental expressions are valid for the free jet-like region up to approximately 0.70 x_p. From Figures 3.16, 3.17, and 3.19 it is possible to write the centerline concentration decay in the forms

$$\frac{C_c}{C_j} = \lambda \; x_\lambda \left(\frac{1}{x}\right) \tag{3.6}$$

$$\frac{C_c}{C_j} = \beta \; x_\beta \left(\frac{1}{x}\right) \tag{3.7}$$

$$\frac{C_c}{C_j} = 0.35 \; x_{_{1/e}} \left(\frac{1}{x}\right) \tag{3.8}$$

Figures 3.20, 3.21, and 3.22 showed that, λ, β, x_λ, x_β, and $x_{_{1/e}}$ can be written as a function of U_r. Therefore Equations 3.6, 3.7, and 3.8 can be expressed as

$$\frac{C_c}{C_j} = (0.55 \ - \ 0.02\ U_r)\ (1.05\ U_r)\ D\left(\frac{1}{x_o + x}\right) \tag{3.9}$$

$$\frac{C_c}{C_j} = (0.35 \ - \ 0.01\ U_r)\ (1.49 \ + \ 1.27\ U_r)\ D\left(\frac{1}{x_o \ + \ x}\right) \tag{3.10}$$

$$\frac{C_c}{C_j} = 0.35\ (6.91 \ + \ 0.30\ U_r)\ D\left(\frac{1}{x_o \ + \ x}\right) \tag{3.11}$$

x_o represents the axial distance at which the effects of the iso-concentration core can be neglected. It was observed that the value of x_o varies with the jet to counterflow velocity ratio U_r. The higher the value of U_r the longer is x_o. However, the proper value of x_o can be easily computed by finding a x_o that produced C_c/C_j equal to 1 for x equal to zero. In order to validate Equations 3.9, 3.10, and 3.11 experiments at $U_r = 8$ and $U_r = 11$ were repeated using the nozzle with a diameter equal to 8.814 mm and the equations were used to predict the centerline decay of the counterflowing jet at these flow conditions. Figure 3.23 depicts the experimental data of the centerline concentration decay of a counterflowing jet with $U_r = 8$ and diameter 8.814 mm. The predicted value of the axial concentration decay using Equations 3.9, 3.10, and 3.11 are also shown in this figure. The predicted values of C_c using the experimental equations seem to follow well the experimental data for the same flow conditions. The error bars shown in Figure 3.23 correspond to the 10 % error using Equation 3.9, which best predicts the experimental data. The same prediction is found when Equation 3.11 is being used. The prediction of the centerline concentration decay improves at higher jet to counterflow velocity ratio, which can be appreciated in Figure 3.24. The data shown in this figure is significantly well predicted by any of the experimental equations, nonetheless, it is easily to observe that Equation 3.9 shows the best prediction of the data. The error bars in the graph correspond to the 10 % error of the predicted value using Equation 3.9. From the previous discussion, it is possible

to suggest that any of these equations can be used to predict the centerline concentration decay for a counterflowing jet for at least the range of jet to counterflowing velocity ratios tested in the present investigation.

3.4 Conclusion

The centerline concentration decay of a round jet issuing into a uniform counterflowing stream has been investigated using planar laser induced fluorescence. The application of the axial penetration x_p as the scaling length of the mean concentration field has been investigated. Additionally, two forms of the aspect ratio of the 5 % contour and the axial distance $x_{1/e}$ were used as length scales for the centerline concentration decay. The following conclusions were drawn from the quantitative study of these length scales:

1. It was observed that the maximum axial penetration of the counterflowing jet generated a similar form of the centerline concentration for $x/x_p \geq 0.5$ (greater than 50 % of the jet penetration). Figure 3.11 shows that the dimensionless form of the centerline concentration proposed by the work of Beltaos and Rajaratnam (1973) is valid just for axial positions downstream of $x/x_p = 50$.

2. The new scaling factors λ and β were found to produce a universal form of the centerline concentration decay, which can be observed in Figures 3.16 and 3.17. The scaling factors were defined based on the aspect ratio of the 5 % contour of the mean concentration field of the counterflowing jet; λ corresponds to the ratio of the maximum lateral penetration (y_p) to the axial location of the maximum lateral penetration of the jet (x_b), and β is given by the ratio of y_p to the maxium axial penetration of the jet (x_p). It was observed that these scaling factors change linearly with the jet to counterflow velocity ratio U_r. Simple empirical equations were proposed to predict the axial centerline concentration of the counterflowing jet.

3. $x_{1/e}$ was shown to be a scale factor of the centerline concentration decay. A

universal form of the centerline concentration decay was obtained when the axial location was scaled with $x_{1/e}$, these results are depicted on Figure 3.19. The length scale $x_{1/e}$ was found to change linearly with U_r, and an empirical equation to predict the centerline concentration of a counterflowing jet was develop using $x_{1/e}$ as the scale of the axial location.

4. The simple empirical equations developed in this investigation were found to predict relatively well the centerline concentration decay in the established flow zone. These expressions are given by the Equations 3.9, 3.10 and 3.11. It is important to notice that these empirical expressions were obtained based just in the mean concentration field of the counterflowing jet. With the results obtained from the empirical expressions it is possible to consider that the prediction of the centerline concentration of the counterflowing jet improved for higher values of jet to counterflowing velocity ratios as can be seen by comparing Figures 3.23 and 3.24.

References

Arendt, J., Babcock, H. A., and Schuster, J. C. (1956). Penetration of a jet into counterflow. *Proc. ASCE Journal Hydraulics Division 82*, pages 1038 – 8 – 11.

Beltaos, S., Brinkworth, B. J., Lam, K. M., and Chan, H. C. (1999). Round jet in ambient counterflowing stream. *Journal of Hydraulic Engineering*, 125(4):428 – 432.

Beltaos, S. and Rajaratnam, N. (1973). Circular turbulent jet in an opposing infinite stream. *First Canadian Hydraulics Conference, Edmonton.*

Bernero, S. and Fiedler, H. E. (2000). Application of particle image velocimetry and proper orthogonal decomposition to the study of a jet in a counterflow. *Experiments in Fluids*, pages S274 – S281.

Chan, H. C. (1999). *Investigation of a round jet into a counterflow*. PhD thesis, Dept. of Civil Engineering, University of Hong Kong.

Chan, H. C. and Lam, K. M. (1998). Centerline velocity decay of a circular jet in a counterflowing stream. *Physics of Fluids*, 10(3):637 – 644.

Dahm, W. J. A. and Dimotakis, P. E. (1990). Mixing at large schmidt number in the self-similar far field of turbulent jets. *Journal of Fluid Mechanics*, 217:299 – 330.

Hilderman, T. L. (2004). *Measurement, modelling, and stochastic simulation of concentration fluctuations in a shear flow*. PhD thesis, University of Alberta.

König, O. and Fiedler, H. E. (1991a). On the asymptotic behaviour of axisymmetric turbulent jets in an ambient stream under arbitrary inclination angles. *Zeitschrift für Flugwissenschaften und Weltraumforschung*, 15(2):103 – 106.

König, O. and Fiedler, H. E. (1991b). The structure of round turbulent jets in counterflow: a flow visualization study. *Advances in turbulence 3*, pages 61 – 66.

Lam, K. M. and Chan, C. H. C. (2002). Time-averaged mixing behavior of circular jet in counterflow: Velocity and concentration measurements. *Journal of Hydraulic Engineering*, 128(9):861 – 865.

Lam, K. M. and Chan, H. C. (1995). Investigation of turbulent jets issuing into a counterflowing stream using digital image processing. *Experiments in Fluids*, 18:210 – 222.

Lam, K. M. and Chan, H. C. (1997). Round jet in ambient counterflowing stream. *Journal of Hydraulic Engineering*, 123(10):895 – 903.

McDannel, M. D., Peterson, P. R., and Samuelsen, G. S. (1982). Species concentration and temperature measurements in a lean premixed flow stabilized by a reverse jet. *Combustion Science and Technology*, 28:211 – 224.

Morgan, W. D. and Brinkworth, B. J. (1976). Upstream penetration of an enclosed counterflowing jet. *Industrial and Engineering Chemistry Fundamentals*, 15(2):125 – 127.

Powell, I. (1987). Design of a laser beam line expander. *Applied Optics*, 26(17):3705 – 3709.

Rajaratnam, N. (1976). *Turbulent jets*, volume 5 of *Developments in Water Science*. Elsevier Science Ltd.

Sui, K. N. (1961). The investigation of the development of circular and planar jets in parallel and opposing streams. *Eesti NSV teaduste akadeemia, Tallin, Toimetised, Isvestia Fuusika - matemaatika - ja technikateaduste seeria. Seeria fiziko - matimaticheskikh nouk.*, 10:215 – 223.

Timma, E. (1962). Turbulent circular and falt streams developing in a counterflow. *Russian periodical, Adakemii Nauk. Estonskoy SSr, Seriya Fiziko - Matamaticheskikh i Tekhnicheskikh Nauk*, 4:253 – 262.

Tsunoda, H. and Saruta, M. (2003). Planal laser-induced fluorescence study on the diffusion field of a round jet in a uniform couter-flow. *Journal of Turbulence*, 4(013).

Yoda, M. and Fiedler, H. E. (1996). The round jet in a uniform counterflow: flow visualization and mean concentration measurements. *Experiments in Fluids*, 21(6):427 – 436.

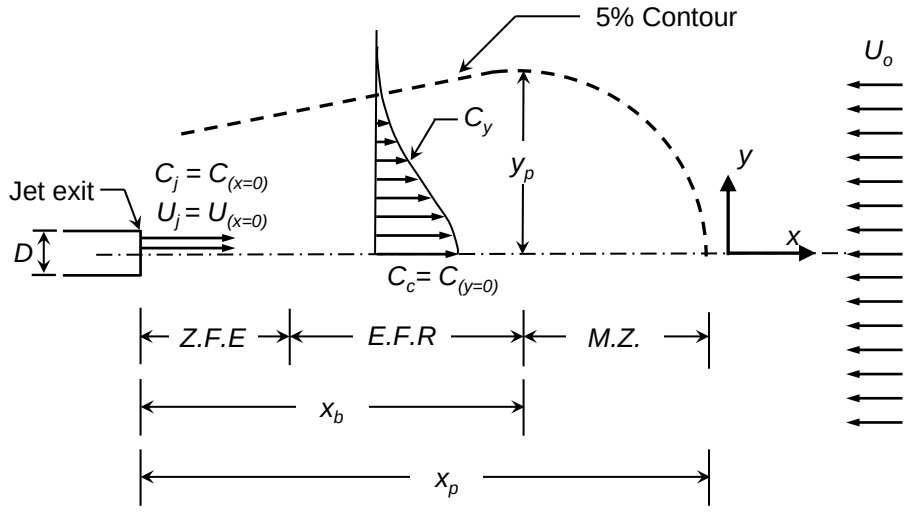

Figure 3.1: Schematic of the geometric parameters in the counterflowing jet (after Beltaos and Rajaratnam (1973), Yoda and Fiedler (1996), and Chan (1999)). Three different regions can be identified: the zone of flow establishment (ZFE), the established flow region (EFR), and the mixing zone (MZ).

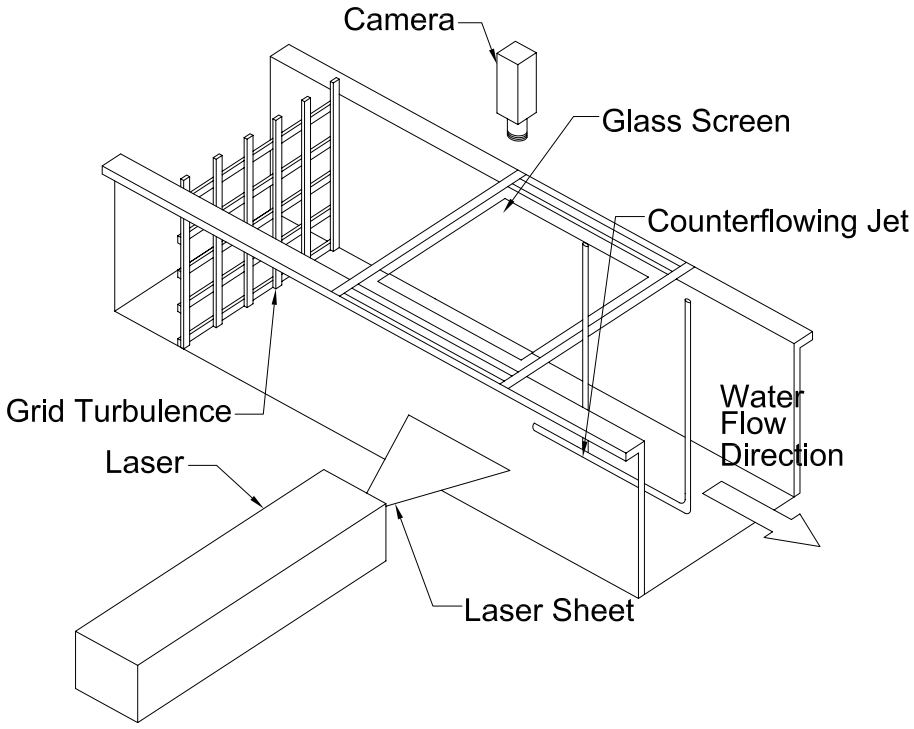

Figure 3.2: Schematic of the experimental setting used to measure the concentration field of the counterflowing jet.

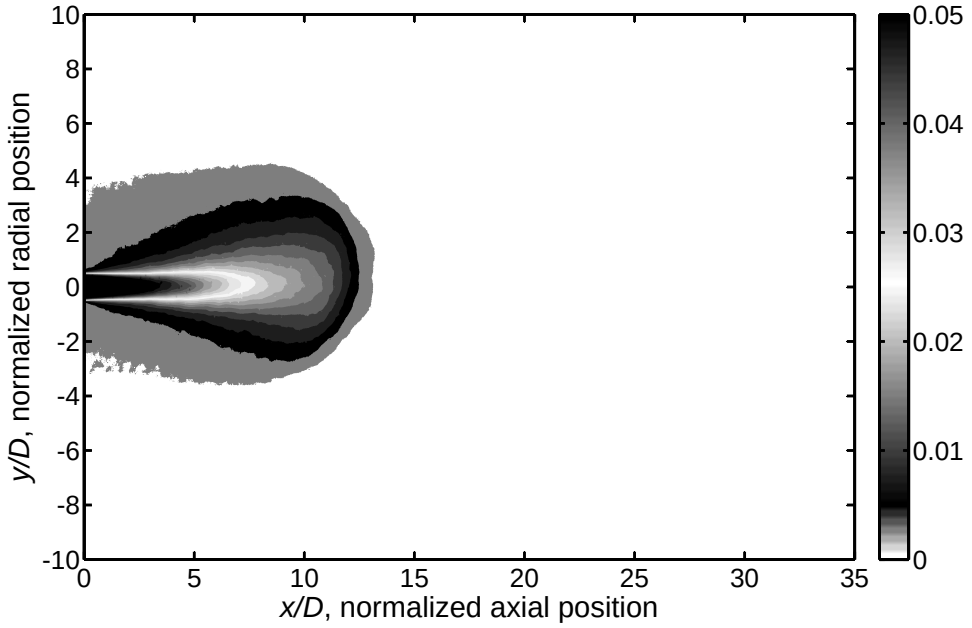

(a)

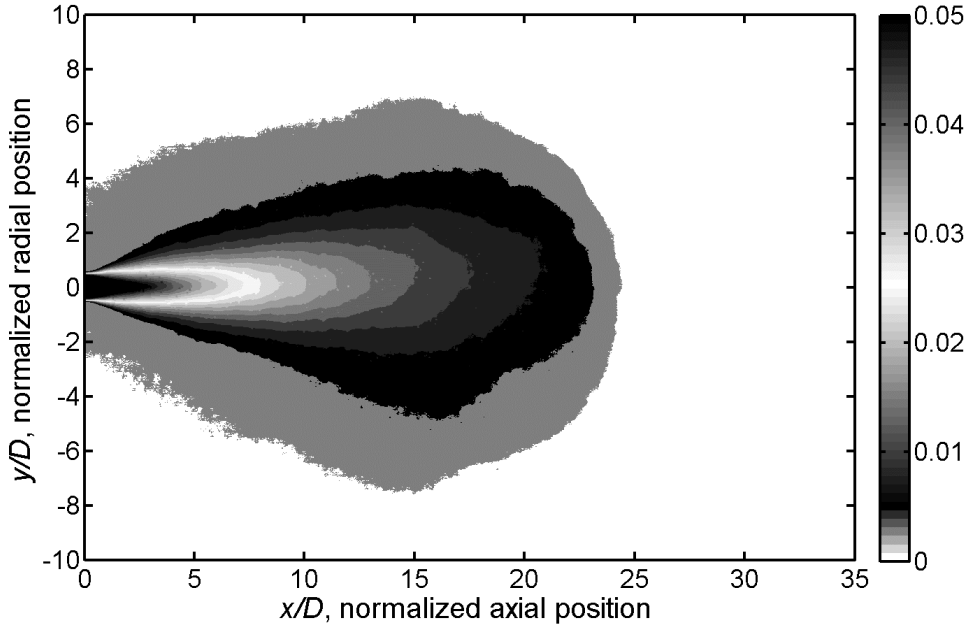

(b)

Figure 3.3: Time average of the scalar concentration field for the counterflowing jet at $Ur = 4$ (a) and $Ur = 8$ (b). The jet diameter of the nozzle used for these experiments was equal to 8.81 mm. The first contour corresponds to a concentration equal to or greater than 5 % of the concentration at the exit of the jet. The color scale of the figure corresponds to the concentration in mg.L^{-1}.

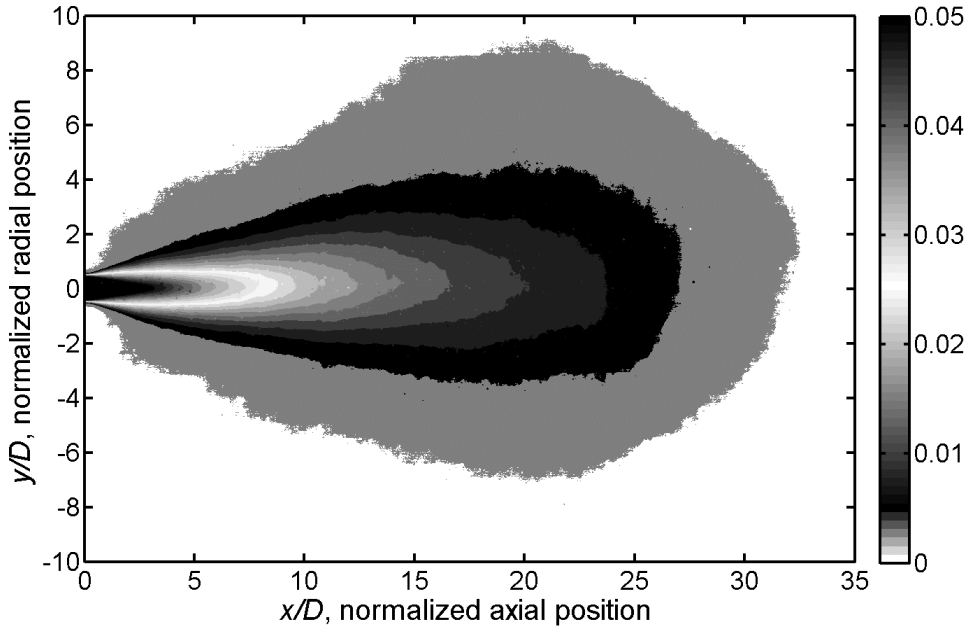

(a)

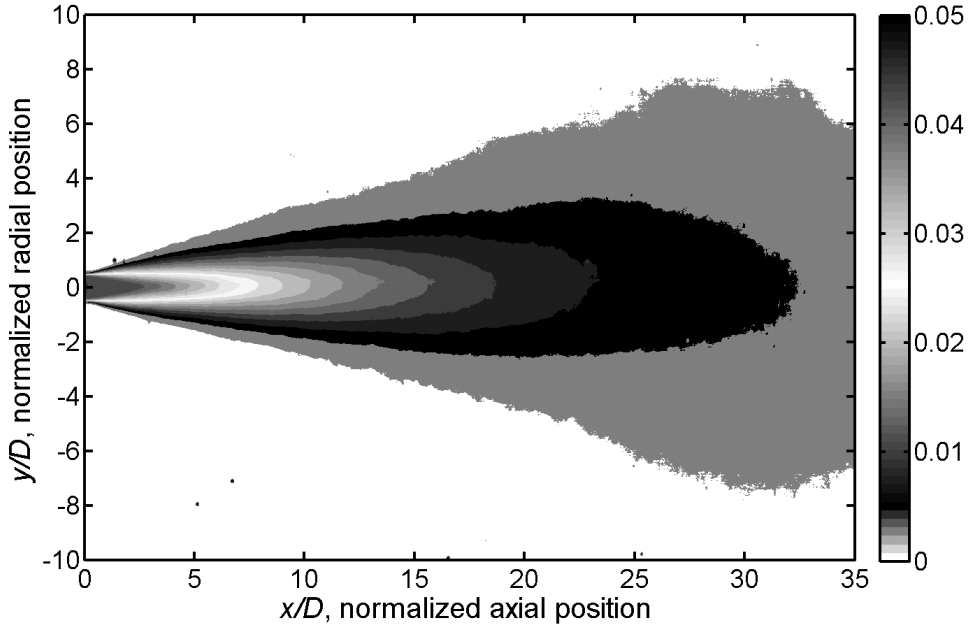

(b)

Figure 3.4: Time averaged of the scalar concentration field for the counterflowing jet at $Ur = 11$ (a) and $Ur = 14$ (b). The jet diameter of the nozzle used for these experiments was equal to 8.81 mm. The first contour corresponds to a concentration equal to or greater than 5 % of the concentration at the exit of the jet. The color scale of the figure corresponds to the concentration in mg.L^{-1}.

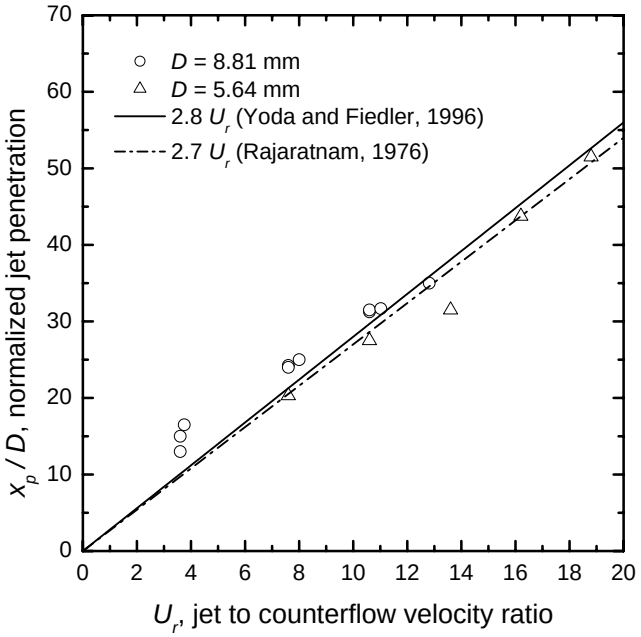

Figure 3.5: Maximum mean axial penetration of the counterflowing jet normalized by the jet diameter against the jet to counterflowing velocity ratio U_r. The data shown in this graph fits relatively well with the linear relation presented by Yoda and Fiedler (1996) and Rajaratnam (1976).

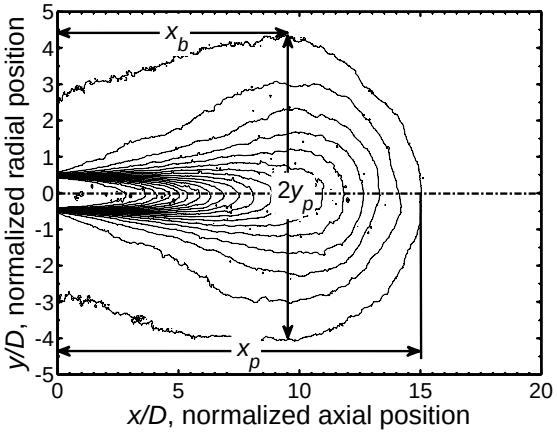

Figure 3.6: Example of the length parameters measured using the 5 % concentration contour for the counterflowing jet for $U_r = 4$, with a jet diameter D_1.

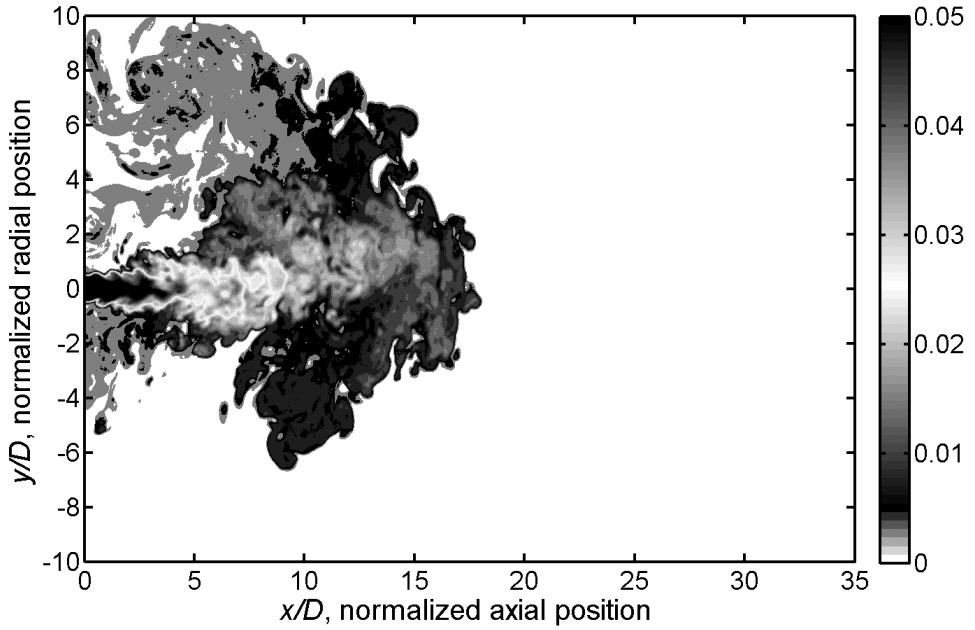

(a)

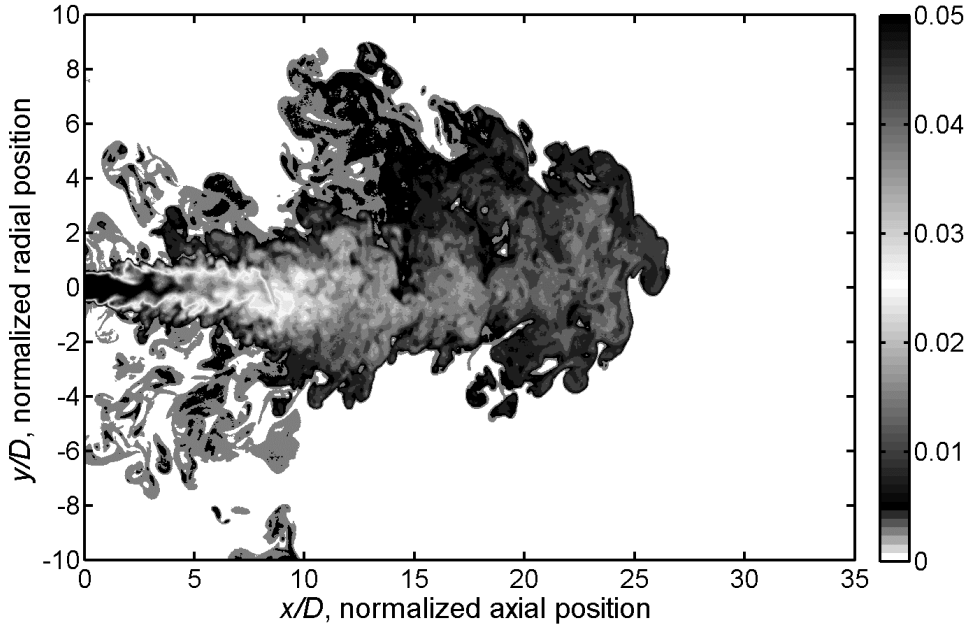

(b)

Figure 3.7: Instantaneous scalar concentration field for the shortest (a) and longest (b) instantaneous axial penetration of the counterflowing jet at $Ur = 8$. The jet diameter used in this configuration was equal to 8.81 mm. The first contour corresponds to a concentration equal to or greater than 5 % of the concentration at the exit of the jet. The color scale of the figure corresponds to the concentration in mg.L^{-1}.

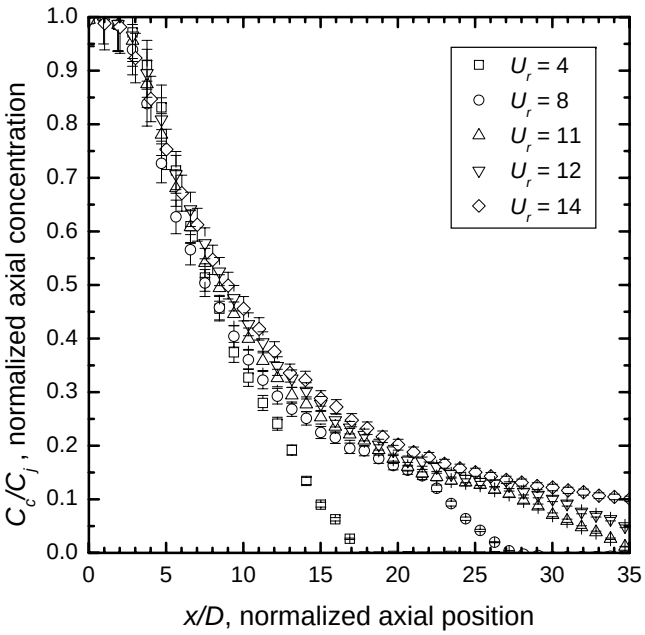

Figure 3.8: Centerline mean concentration decay for the counterflowing jet with nozzle diameter of 8.81 mm.

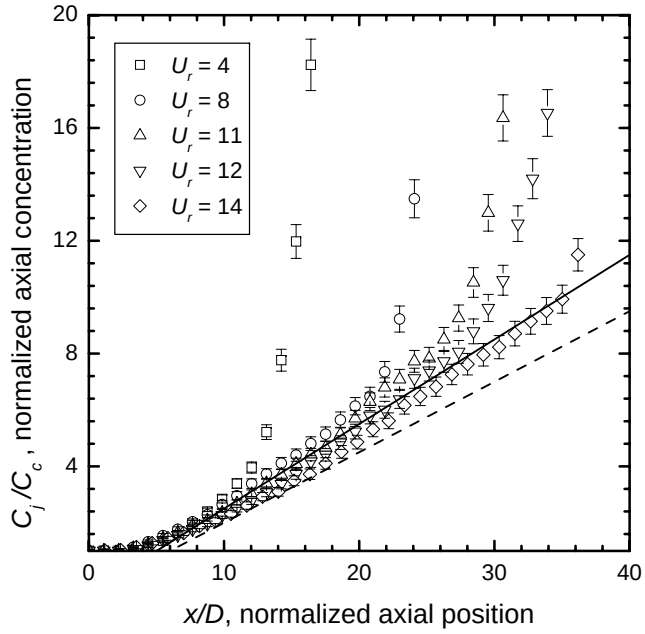

Figure 3.9: Centerline mean concentration dilution for a counterflowing jet with D = 8.81 mm. The dashed line represents the slope of 0.25 found by Yoda and Fiedler (1996) for $x/D \leq 10$. Solid line shows the slope of 0.3 for the data found in the present study.

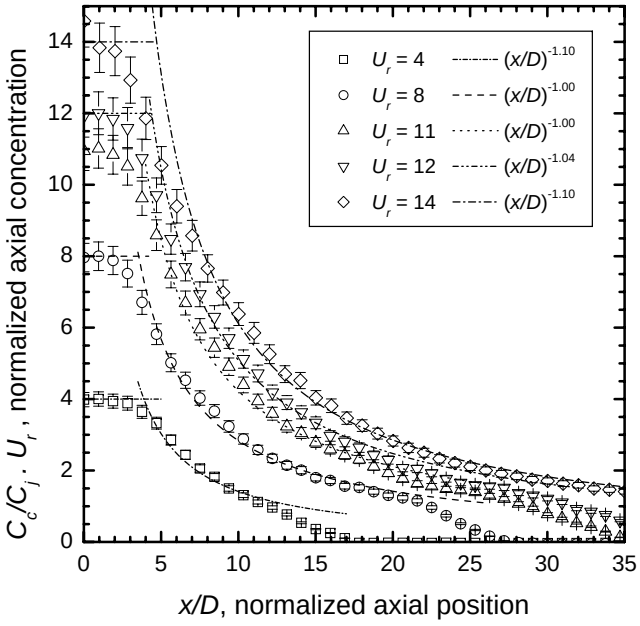

Figure 3.10: The normalized centerline mean concentration at different jet to counterflow velocity ratios. The jet diameter for this experiment was equal to 8.81 mm.

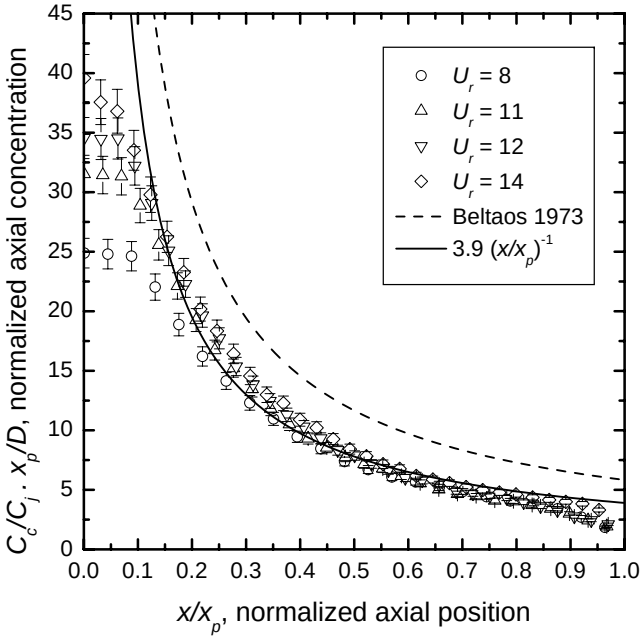

Figure 3.11: Centerline concentration decay of the counterflowing jet plotted using the universal form presented by Beltaos and Rajaratnam (1973) for the centerline velocity decay of a jet in a counterflow stream.

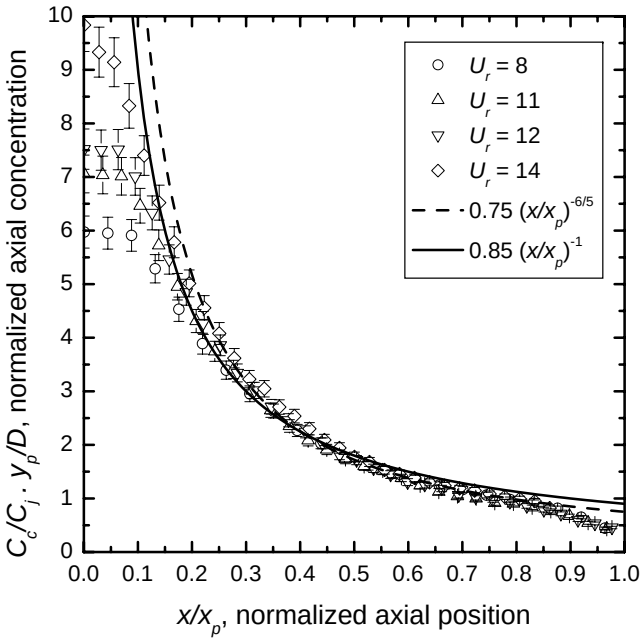

Figure 3.12: Centerline concentration decay of the counterflowing jet plotted using the modified version of the universal form presented by Beltaos and Rajaratnam (1973) for the nozzle of diameter D_1.

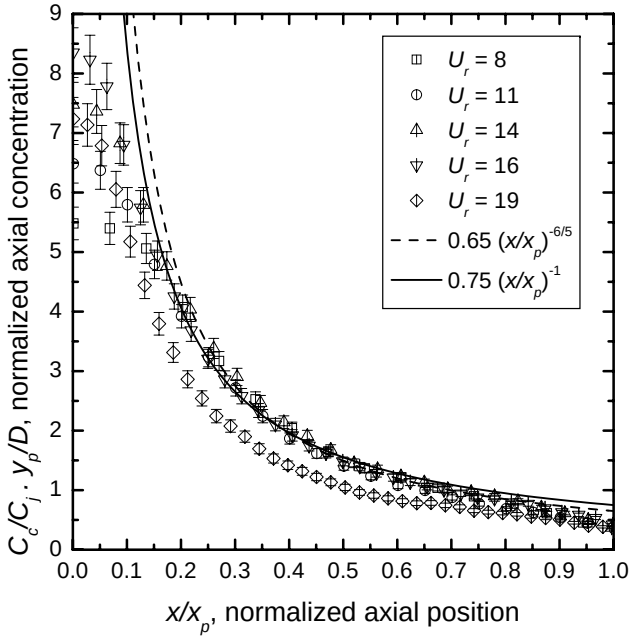

Figure 3.13: Centerline concentration decay of the counterflowing jet plotted using the modified version of the universal form presented by Beltaos and Rajaratnam (1973) for the nozzle of diameter D_2.

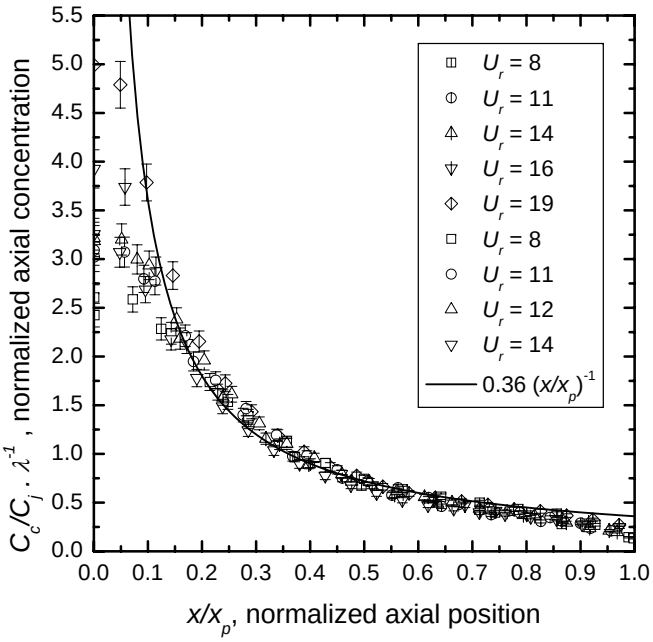

Figure 3.14: Centerline concentration profiles of the counterflowing jet. λ^{-1} was used as the scale factor for the axial concentration. Open blank symbols correspond to D_1 and the crossed symbols to D_2.

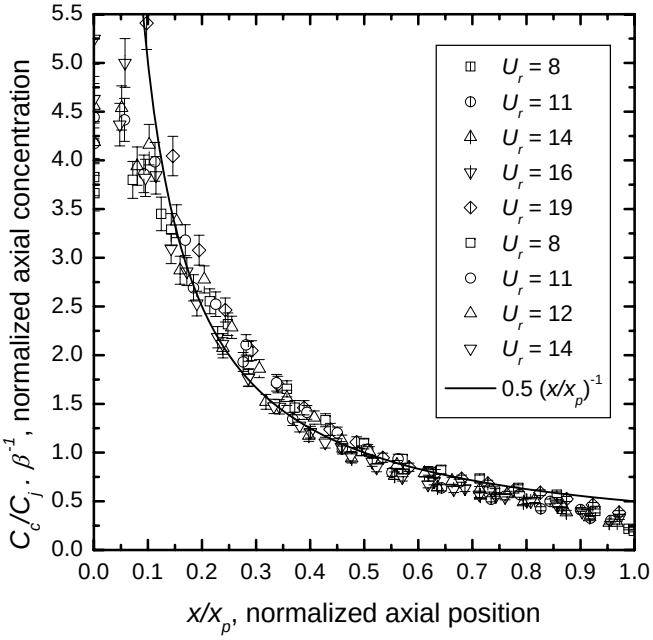

Figure 3.15: Centerline concentration profiles of the counterflowing jet. β^{-1} was used as the scale factor for the axial concentration. Open blank symbols correspond to D_1 and the crossed symbols to D_2.

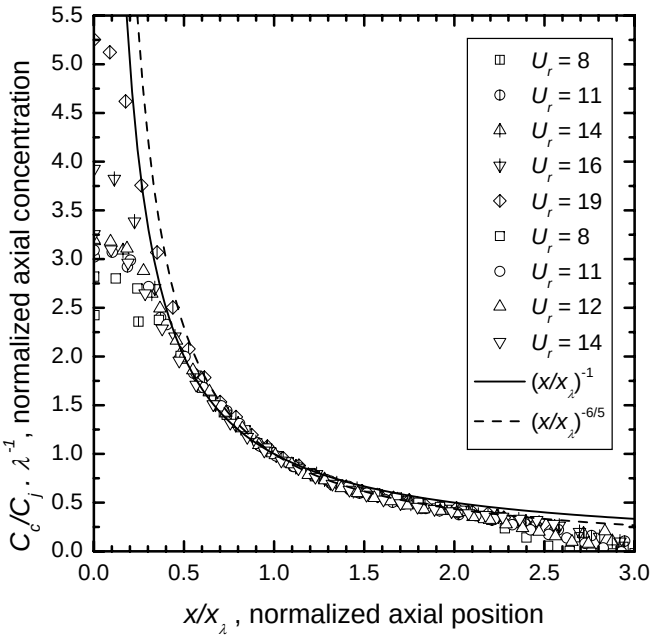

Figure 3.16: Centerline concentration profiles of the counterflowing jet. λ^{-1} and x_λ were used as the scale factor C_c/C_j and x respectively. Open blank symbols correspond to D_1 and the crossed symbols to D_2.

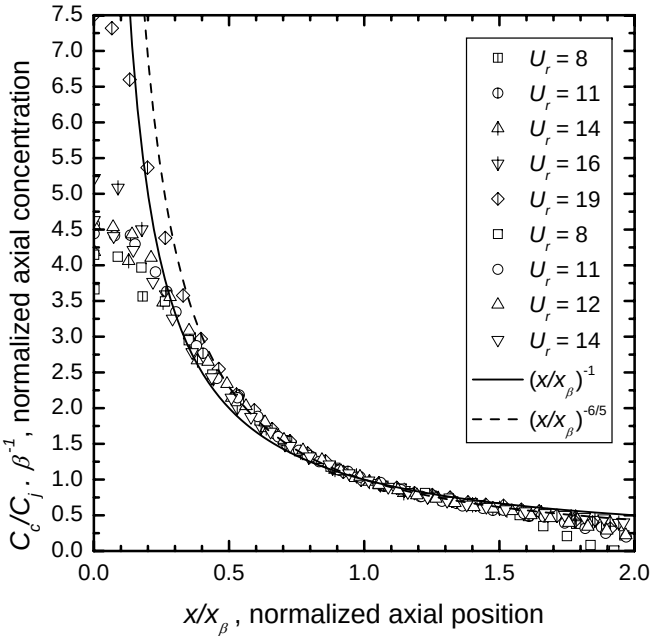

Figure 3.17: Centerline concentration profiles of the counterflowing jet. β^{-1} and x_β were used as the scale factor C_c/C_j and x respectively. Open blank symbols correspond to D_1 and the crossed symbols to D_2.

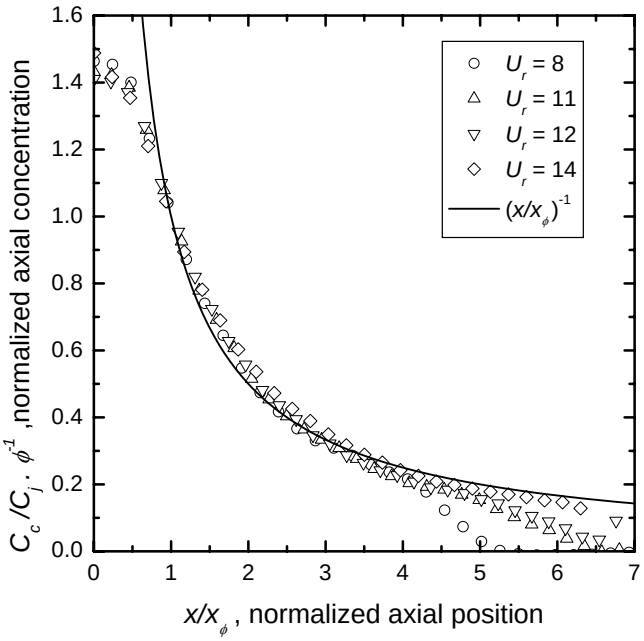

Figure 3.18: Centerline concentration profiles of the counterflowing jet. ϕ^{-1} and x_ϕ were used as the scale factor C_c/C_j and x respectively. Experiments correspond to the large jet nozzle D_1.

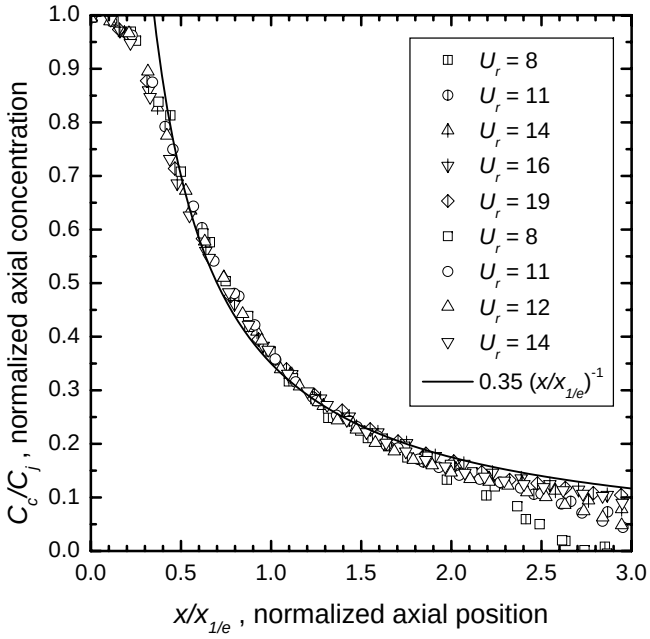

Figure 3.19: Centerline concentration decay of the counterflowing jet. The axial position is normalized by the axial distance for which $C_c = e^{-1} C_j$. Open blank symbols correspond to D_1 and the crossed symbols to D_2.

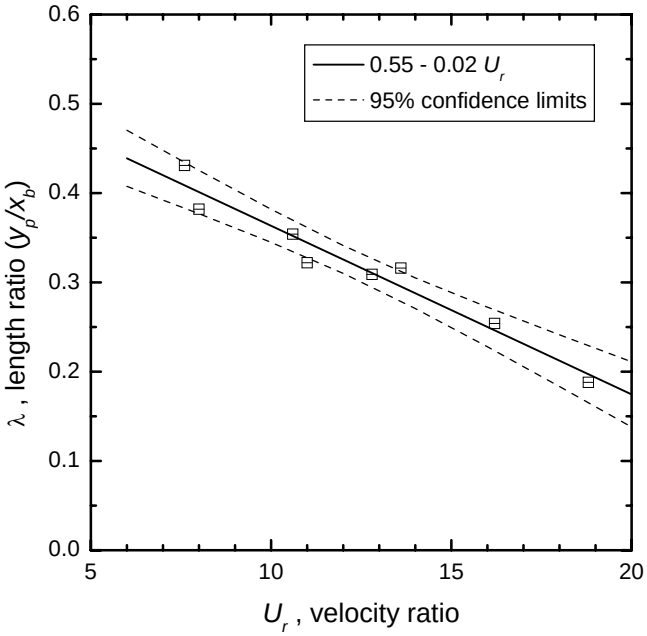

(a)

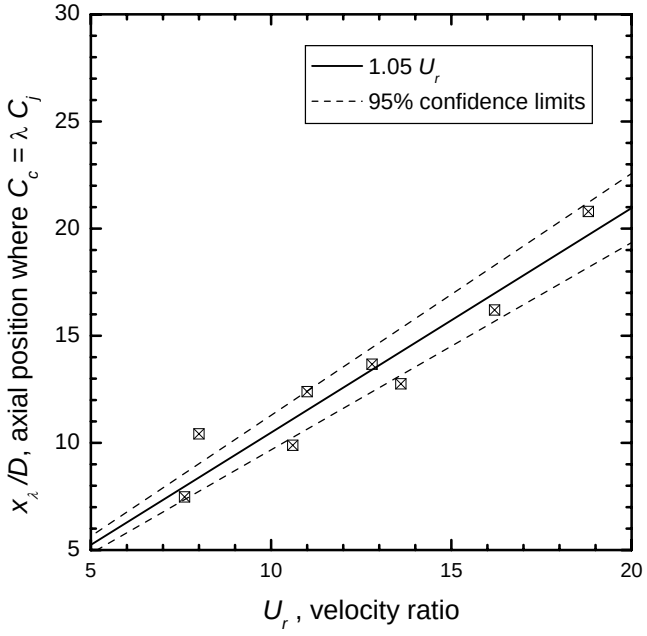

(b)

Figure 3.20: Variation of the new parameters λ (a) and x_λ (b) with the jet to counterflowing velocity ratio U_r.

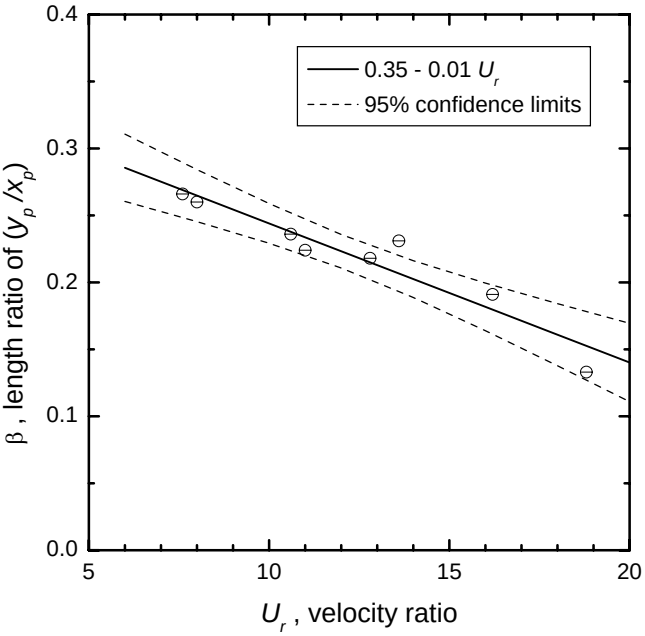

(a)

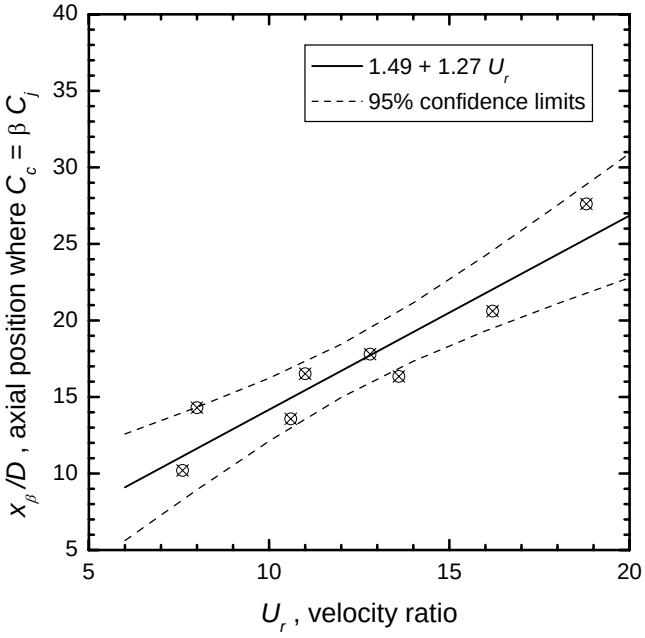

(b)

Figure 3.21: Variation of the new parameters β (a) and x_β (b) with the jet to counterflowing velocity ratio U_r.

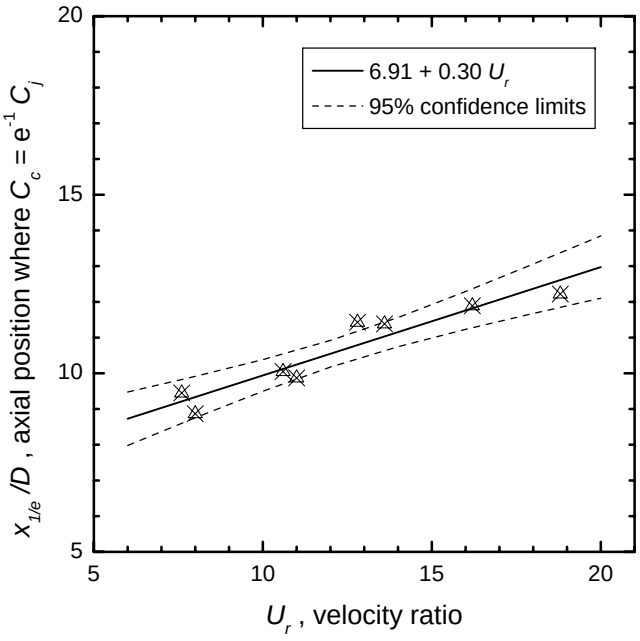

Figure 3.22: Axial distance $x_{1/e}$ as a function of the jet to counterflowing velocity ratio U_r.

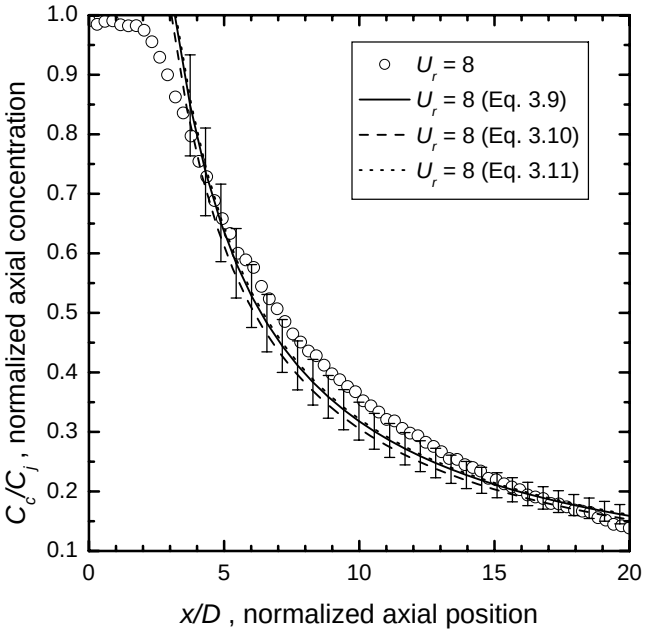

Figure 3.23: Centerline concentration decay for a counterflowing jet with $U_r = 8$. The lines show the predicted value based on the developed experimental equations.

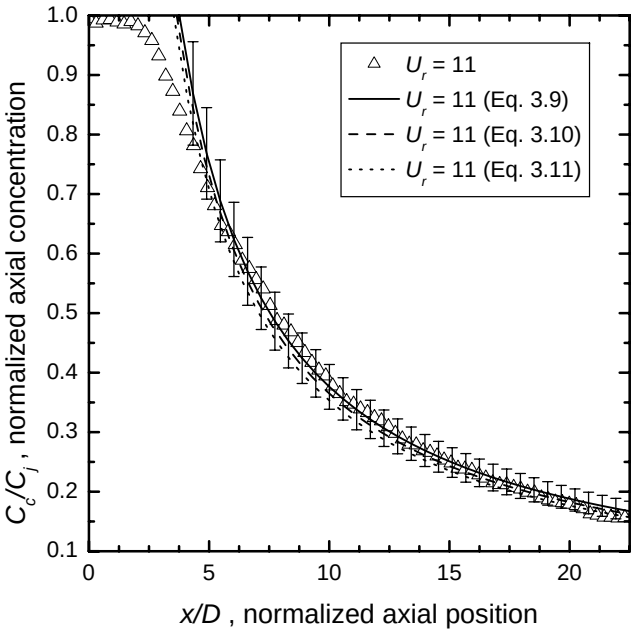

Figure 3.24: Centerline concentration decay for a counterflowing jet with jet to counterflow velocity ratio of 11. The lines show the predicted value based on the developed experimental equations.

Chapter 4

Radial profiles of a counterflowing jet: averaged concentration measurements

Abstract

The time averaged radial concentration fields have been measured in a water counterflowing jet. Fluorescein sodium salt has been used as the tracer and planar laser induced fluorescence method was employed to obtain the information of the concentration field. A correction process was used to obtain the data of the concentration field from the raw data. Five different jet to counterflow velocity ratios were tested. Radial concentration profiles of the mean concentration field for the established flow region and the mixing zone of the counterflowing jet are presented in this investigation. The growth of the concentration jet width of different flow conditions was investigated. An attempt to find new length scales for the radial spreading of the jet is presented in this study. The similarity region was found in the inner region of the radial spreading of the counterflowing jet. It was found that the growth of the concentration jet width can be divided into two different regions, the linear growth region and the power law growth region.

4.1 Introduction and Background

The flow of a counterflowing jet is generated by a nozzle of diameter D with a velocity U_j, and concentration C_j. Once the jet is in contact with the uniform counterflowing stream, of velocity U_o, a momentum exchange process begins. This process creates a decay of the velocity and concentration downstream from the exit of the jet nozzle. The counterflow stream mixes with the jet flow and is able to bend and stop the jet that is then carried backward with this opposite current (Yoda and Fiedler, 1996). The distance from the nozzle of the jet to the point where the jet stops, is known as the jet penetration length, which also defines the location of the stagnation streamsurface at the centerline of the jet. There are also important parameters such as the maximum lateral penetration and the axial distance of this maximum lateral penetration. The mean flow geometrical parameters for a counterflowing jet are shown in Figure 4.1. Figure 4.1 also shows three regions downstream from the jet exit. The zone of flow establishment (ZFE) contains the iso-concentration core and the transition to the established flow region (EFR). In the established flow region the jet flow is the dominant flow and the counterflowing jet behaves like an ordinary jet (König and Fiedler, 1991; Beltaos et al., 1999; Yoda and Fiedler, 1996). Finally, the mixing zone (MZ) where the flow is dominated by the counterflow stream. It is important to mention that there is a transition between the established flow region and the mixing zone that has not been clearly defined by previous investigations.

Jets in a counterflow stream are commonly found in industrial applications that requires enhancing of mixing, as is the case of environmental fluid applications (Beltaos and Rajaratnam, 1973; Lam and Chan, 1995; Chan, 1999). Despite this fact, the characteristics of this flow have been the subject of few investigations. Among the few investigations carried out in relation to the counterflowing jet, the penetration distance and the centerline velocity decay of a counterflowing jet have been the object of the majority of efforts while very few are related to the radial spreading of the jet. Beltaos and Rajaratnam (1973) presented a similarity function of the radial

velocity profiles based on a theoretical analysis of a potential flow solution. Lam and Chan (2002) also studied the radial spreading of a circular jet in a counterflow stream. These authors found that the similarity function presented by Beltaos and Rajaratnam (1973) was in fact valid for the mean velocity field within the range of jet to counterflow velocity ratios studied. Lam and Chan (2002), employed the similarity function in the averaged concentration field of the counterflowing jet. It was found that the radial concentration data at the studied velocity ratios collapsed into a single curve up to 50 % of the centerline concentration. Beyond this point, the radial profiles did not collapse into a single curve. As was suggested by Yoda and Fiedler (1996) and pointed out by Lam and Chan (2002) "the flow of a jet in a counterflow can be divided into an inner [radial location smaller than the jet width] region where the forward jet flow dominates and an outer flow region [radial location greater than the jet width] where the effect of the backward counterflow is important". This explains the fact that only the inner region of the radial concentration profiles follows the similarity function whereas the radial concentrations in the outer zone were found to exceed the values of the Gaussian fit used for a jet in quiescent surroundings Lam and Chan (2002).

The previous chapter (Chapter 3) showed that two forms of the aspect ratio of the 5 % contour and the axial distance $x_{1/e}$ can be used as length scales for the centerline concentration decay, generating a universal form of the centerline concentration decay of the counterflowing jet. In this chapter, these new length scales are used in the radial concentration profiles attempting to find new similarity forms of the profiles in the radial direction. Planar laser induced fluorescence is used to obtain the data of the instantaneous mean concentration field of the counterflowing jet. An investigation of the physical properties of the mean concentration radial profiles in the established flow region and mixing zone of the counterflowing jet is presented in this Chapter. In the established flow region the flow behaves as a jet in quiescent surroundings and the jet is the dominant flow. In the mixing zone the properties of the flow are dominated by the counterflow stream. The different rates of the growth of the jet width in

the regions of the counterflowing jet are investigated and empirical expressions to estimate the width of the jet are given.

4.2 Experimental Setup and Techniques

A closed loop water channel facility in the Mechanical Engineering Department at the University of Alberta was used as the experimental facility. The water channel has a cross section 680 mm wide by 480 mm high with a total length of 5000 mm. Two different cylindrical nozzles were used to produce the counterflowing jet. The diameter of these two nozzles were 8.84 and 5.64 mm, hereafter referred to as D_1 and D_2 respectively. The source of the jet was a pressurized stainless steel tank with a constant gauge pressure of 206.84 kPa. Both jets were designed to have a inlet length of 104D with the aim of having a fully developed flow. A system of valve rotameter was installed at the inlet line of the jet in order to monitor and control the desired jet velocity. The calibration curves for the different jets diameters can be found in Figure B.1. The nozzle of the jet was located in the center of the water channel cross section at approximately 3200 mm downstream of the inlet of the water channel. The jet was set at approximately 200 mmm from the bottom of the water channel keeping a constant water level of 400 mm for all the experiments. Different jet to counterflow velocity ratios were tested for the two jet diameters, the velocity of the counterflow stream was kept at a constant value of 5 cm.s^{-1} as the velocity of the jet was adjusted to obtain the desired jet to counterflow velocity ratio. Table 4.1 resumes the approximate initial jet conditions investigated in this study.

Figure 4.2 depicts the schematic of the experimental set-up used to measure the concentration field of the counterflowing jet. A uniform grid was place at the inlet of the water channel (see Figure 2.14) built with flat stainless steel bars of 19.2 by 5 mm of cross section area. The total open area was approximately 56 % with a mesh spacing of 76.2 mm. This grid turbulence generates near uniform velocity profile for the streamwise component, with variations found to be within 5 % (Hilderman, 2004).

Table 4.1: Initial jet conditions for every experiment of the scalar concentration measurements.

D (mm)	U_j (m.s^{-1})	U_r	Re_D
8.81	0.18	4	1580
8.81	0.38	8	3330
8.81	0.53	11	4640
8.81	0.62	12	5430
8.81	0.67	14	5870
5.64	0.38	8	2130
5.64	0.53	11	2970
5.64	0.68	14	3810
5.64	0.81	16	4540
5.64	0.94	19	5270

At the test section the turbulence intensity was found to be about 4 % for the mean horizontal (Hilderman, 2004). A glass screen placed on the free surface was used to avoid any distortion due to the small waves generated at the surface. The laser sheet was obtained using the optical arrangement depicted in Figure 2.4. The camera was placed at approximately 1200 mm from the axis of the jet.

Planar laser induced fluorescein was used as the technique to measure the concentration for the scalar field of the counterflowing jet. Fluorescein sodium salt was used as the scalar species in the jet. The fluorescein sodium salt was added to the pressurized stainless steel tank. The amount of dye added to the tank was selected in order to obtain a final dye concentration of 0.05 mg.L^{-1}. This concentration was kept constant for all the experiments. An optical arrangement that includes a Powell lens® was used to generate an approximately uniform thin laser sheet (Powell, 1987). The laser used was a 2.1 W Argon ion laser, the laser was operated in a single mode at a wavelength of 488 nm, which corresponds to the proper wavelength for the fluorescein sodium salt (Walker, 1987). A calibration process was employed before every experiment in order to obtain the scalar concentration field out of digital imaging analysis. The calibration images were obtained by traversing a glass square tube with a known dye concentration along the field of view of the camera while a set of images

were being taken. Then, the final calibration images were obtained by processing the sequence of instantaneous images at the known concentration. A first degree polynomial was used to convert the fluorescent intensity into scalar concentration data (a detailed explanation of the calibration process can be found in Chapter 2). Images were recorded using a 12 bit SensiCam high speed CCD system, with a resolution of 1280 x 1024 pixels. At every flow jet condition a set of 500 images were taken at a rate of 19.32 Hz, the exposure time used in these images was 10 ms. The spatial resolution established for the experiments was approximately 0.3 mm.pixel^{-1}.

4.3 Experimental Results

The study of the spreading of the counterflowing jet was focused on the two main regions downstream the exit of the jet. These two regions are: the established flow region where the jet is the dominant flow and the mixing zone where the counterflow stream dominates the jet flow (see Figure 4.1). The established flow region is found to be downstream from the zone of flow establishment (Figure 4.1) up to approximately 70 % of the total penetration of the jet. The mixing zone can be found at axial distances greater than 70 % of the maximum axial penetration.

The mean geometric length parameters of the counterflowing jet were computed by considering the 5 % contour of the concentration at the exit of the jet. An example of the measurements for the different geometrical lengths for the counterflowing jet is given in Figure 4.3. The mean geometric length parameters are: maximum penetration length (x_p), axial location of the maximum lateral penetration (x_b), and the maximum lateral penetration (y_p). From Figure 4.3 it is possible to notice that the shape of the 5 % contour is not perfectly symmetric along the axis of the jet, therefore, the maximum lateral penetration is not the same in both directions. Consequently, the value of y_p was determined by considering the average of the maximum penetration in both directions; this is the maximum half-width of the 5 % concentration contour. Table 4.2 resumes the values of the mean geometric length obtained from

the different flow conditions of the experiments.

Table 4.2: Penetration distance, length of the established flow region, and lateral penetration of 5 % concentration contour of the jet.

Jet Nozzle	U_r	x_p/D	y_p/D	y_p/x_p	x_b/x_p
8.81 mm	4	16.50	4.21	0.26	0.60
	8	25.00	6.50	0.24	0.68
	11	31.67	7.09	0.22	0.69
	12	34.75	7.56	0.22	0.71
	14	42.00*	9.44	0.23	0.70
5.64 mm	8	20.25	5.50	0.27	0.66
	11	27.25	5.94	0.24	0.66
	14	31.50	7.50	0.24	0.76
	16	43.75	8.38	0.19	0.75
	19	51.50	6.88	0.13	0.71

* This value of x_p was estimated by assuming that x_b was approximately 70 % of the jet penetration. This was average experimental value found through the analysis of the data for the other flow conditions. The maximum penetration of the jet for this flow condition was out of the field of view of the camera.

4.3.1 Counterflowing jet spreading in the established flow region

Figure 4.4 depicts the normalized radial concentration profiles at different axial locations. The data of the profiles at U_r =12 for the nozzle diameter equal to 8.81 mm were not included since the resulting data at this jet to counterflowing velocity ratio were very similar to the data obtained for U_r =11. The radial profiles were obtained for location within the established flow region, downstream of $x/D \geq 6$ (Chan and Lam, 1998; Lam and Chan, 2002)and upstream of $0.70x_p$. For axial distances $x/D \geq 6$ the iso-concentration core effects in the radial profiles were found to be negligible for the velocity ratios studied in this investigation. As can be seen, at x/D =6 the axial concentration was found to be approximately $0.65C_j$. This shows the fast decay of the axial concentration of a counterflowing jet. It is possible to appreciate that the greater the velocity ratio the lower the concentration level at the beginning of the

mixing zone. It appears that the radial concentration resembles a Gaussian distribution, that is commonly found in the case of mean velocity profiles in turbulent round jets (Pope, 2000). Figure 4.4 shows that the radial concentration profiles reach the zero concentration level at radial distances greater than the case of a jet in a stagnant ambient and a coflowing jet. For the case of U_r =4 (Figure 4.4a) the zero concentration level was reached at approximately 7D from the center of the nozzle. At U_r =8 (Figure 4.4b) this zero concentration level was obtained at approximately 12D in the radial direction. The distance where the radial concentration is equal to zero, was found to increase with the jet to counterflow velocity ratio. The concentration levels presented at the tail of the profiles correspond to the dye of the jet that is being carried back by the counterflow stream. High values of U_r result in a larger penetration of the jet and in an increment of the fluctuations of the jet flow, therefore the dye is diluted into the upcoming stream further downstream that is the case of low values of U_r.

In order to study the similarity region for the radial spreading of the counterflowing jet, the radial concentration profiles were plotted in a dimensionless form. The mean concentration along the radial direction (C_y) was normalized by the concentration at the centerline of the jet in the axial location of the profile (C_c). The location of the concentration in the radial position y was normalized by the location at which the local mean concentration was equal to half the concentration at the centerline of the jet, this is $C_y = 0.5C_c$ (this distance was denoted as $y_{_{1/2}}$). Figure 4.5 depicts the dimensionless form of the radial concentration profiles at different locations along the centerline of the counterflowing jet. The dimensionless concentration profiles in Figure 4.5 do not include the corresponding data for U_r =12, since the results are very similar to those found for U_r =11.

As can be seen in Figure 4.5 the dimensionless radial concentration profiles obtained for axial positions within the EFZ collapse into a single curve for a specific length of the radial location of the concentration profile. The length of the collapsing region

seems to be affected by U_r. In Figure 4.5a, which corresponds to a U_r =4, the region was found for $y/y_{_{1/2}} \leq 1.25$. A larger region was observed for the case of U_r =8 (Figure 4.5b) where the collapsing region was found for $y/y_{_{1/2}} \leq 1.5$. Nonetheless, from Figure 4.5c it is possible to appreciate that the region for which the concentration profiles collapsed into a single curve at U_r =11 is approximately equal to the one found for U_r =4. Figure 4.5d depicts the dimensionless profiles for U_r =14, the collapsing region at this velocity ratio was found for $y/y_{_{1/2}} \leq 1$.

Lam and Chan (2002) presented radial profiles for a counterflowing jet for velocity ratios equal to 3, 5, 7.5, and 10, in their results, the concentration data show a similar region just for $y/y_{_{1/2}} < 1$ (r/b_c within the article). Therefore, the length for which the radial concentration profiles show a universal form in the present study, was found to be larger than the one obtained by Lam and Chan (2002). In the region greater than $y/y_{_{1/2}} = 1$ Lam and Chan (2002) reported that the concentration data were found to be above the Gaussian distribution, which can be also observed in Figure 4.5. However, there is a significant difference between the results shown by Lam and Chan (2002) and the present investigation. It is possible to see from Figure 4.5, that the dimensionless radial profiles better resemble the Gaussian distribution for profiles closer to the exit of the jet. The closer to the exit of the jet the more dominant the jet flow, therefore it is expected that for positions closer to the nozzle, the dimensionless data should show a behavior similar to the one observed in free jets. The difference between the dimensionless concentration data and the Gaussian distribution at the tails increases systematically with the axial distance until the mixing zone is approached and the instabilities of this region start affecting this pattern; this can be seen in Figure 4.5. This systematic behavior is not observed in the graphs shown by Lam and Chan (2002), in fact it is interesting how their profiles further from the jet exit better resemble a Gaussian distribution. This is very curious, because the greater the distance downstream from the jet exit, the bigger the effect of the counterflowing stream on the jet profile. Furthermore, one would expect the relative impact of the counterflow scalar to have relatively less effect on the normalized profiles near the jet

exit where the peak centreline concentration is highest.

Figure 4.6 depicts the dimensionless radial concentration profiles for the jet with a nozzle diameter equal to 5.64 mm (D_2). Similar to the result observed for D_1, the dimensionless radial concentration profiles also show a universal form for an inner region of the radial spreading, this is $y/y_{_{1/2}} < 1$. This region was also observed by Lam and Chan (2002). As the smaller jet diameter showed results very similar to the larger, it is possible to suggest that the similarity region of the dimensionless radial concentration profiles within the established flow region is independent of the initial condition of the jet, at least for the two conditions studied in the present investigation. Similar to Figure 4.5 it can be appreciated that for the smaller diameter, the greater scatter of the radial data was found for concentration profiles close to the interface between the established flow region and the mixing zone. It would appear that there is a different shape for the concentration profiles in the mixing zone, which would account for the apparent break from the trend in profiles when passing from the established flow region to the mixing zone. From Figures 4.5 and 4.6 it is possible to infer that there is a limit for which the effects of the counterflow stream on the dimensionless radial concentrations profiles can be neglected. This limit was found to be approximately 50 % of the total penetration length. Therefore, hereafter the radial concentration profiles will be studied just for $x < 0.5\ x_p$.

A different form employed to obtain similar profiles within the self preservative region of jets and plumes is obtained when the radial position is normalized by the distance at which the radial concentration takes the value of e^{-1} times ($\approx$0.37) the concentration at the center line (Fischer et al. 1979; Wood 1993; Lee and Chu 2003). The radial position for which $C_y = e^{-1}\ C_c$ is identified, in the present investigation, as is $y_{_{1/e}}$.

Figure 4.7 depicts the normalized concentration profiles obtained using $y_{_{1/e}}$ as the

scale for the radial location. As can be seen, these results are very similar to those generated when using the jet half-width ($y_{1/2}$) as the length scale for the radial position. The inner region of the radial profiles ($y/y_{1/e} < 1$) collapse into a universal form for the radial spreading of the jet. It is also possible to observe that the effects of the mixing zone on the radial profiles are not present for the axial locations shown in Figure 4.7. This is because, all the concentration profiles shown in this figure are contained within the range of $x < 0.5\ x_p$. Even though Figure 4.5 and Figure 4.7 show a very good collapse of the radial concentration profiles for $y/y_{1/2} < 1$ and $y/y_{1/e} < 1$ respectively, it is important to recall that $y_{1/e} < y_{1/2}$. Consequently, using $y_{1/e}$ as the scale of the radial position will result in a wider range of the radial concentration profiles that are represented by the curve shown in Figure 4.7. The Gaussian distribution depicted in Figures 4.5 and 4.7 are respectively given by the equations

$$\frac{C_y}{C_c} = \exp\left[-\frac{4}{5}\left(\frac{y}{y_{1/2}}\right)^2\right] \tag{4.1}$$

$$\frac{C_y}{C_c} = \exp\left[-\frac{6}{5}\left(\frac{y}{y_{1/e}}\right)^2\right] \tag{4.2}$$

In a previous chapter (Chapter 3), two scales were used to successfully obtain a universal function for the centerline concentration decay of the counterflowing jet. These scales originated from the ratio of y_p/x_b and y_p/x_p, indicated by the Greek letters λ and β respectively. Figures 4.8 and 4.9 depict the dimensionless radial concentration profiles of the concentration for axial locations within $x < 0.5\ x_p$. Where y_λ and y_β are the value of y at which the radial concentration C_y is equal to λC_c and βC_c respectively. Figure 4.8 shows how the data of the radial concentration collapse onto a single curve for $y/y_\lambda < 1.25$ however, it is important to notice that the Gaussian distribution used to represent the radial data is different for every graph contained in Figure 4.8. Therefore, y_λ should not be seen as a scale for the spreading of the counterflowing jet in the radial direction since a universal form was not observed. In

a similar manner Figure 4.9 depicts the radial concentration profiles for $x < 0.5\ x_p$ using y_β as the scale factor for the radial position. It is possible to observe that the radial concentration profiles in Figure 4.9c and Figure 4.9d do not collapse into a single curve as was shown previously in Figures 4.5 and 4.7. Additionally when using y_β as the scale for the location in the radial direction, the resulting Gaussian distribution has a dependance on U_r, as different distributions were obtained (see Figure 4.9). As a result it would appear that neither y_λ nor y_β are ideal scaling factors for the spreading of the counterflowing jet in the radial direction.

The effect that U_r has in the dimensionless concentration profiles shown in Figures 4.5 and 4.7 was studied by plotting the dimensionless radial concentration profiles at the same axial distance for different jet to counterflowing velocity ratios. Figures 4.10 and 4.11 depict the dimensionless radial concentration at $x/D = 6$ using $y_{_{1/2}}$ and $y_{_{1/e}}$ for different jet to counterflow velocity ratios. The data shown in Figures 4.10 and 4.11 correspond to the jet with nozzle diameter D_1. As U_r increases the radial profiles resemble the Gaussian distribution shown in the graph. This behaviour shows that the higher U_r, the less significant are the effects of the counterflow stream. For the highest value of U_r the radial concentration distribution best fit the Gaussian distribution upstream the mixing zone (shown in a solid line).

For the simple jet, the variation of $y_{_{1/2}}$ and $y_{_{1/e}}$ with the axial distance downstream from the exit of the jet have been shown to be linear (Fischer et al., 1979). Figure 4.12 shows the growth of the jet width $y_{_{1/2}}$, for different jet to counterflowing velocity ratios. This line represented the growth rate of the jet width found by Kiser (1963) for the case of a free axisymmetric turbulent water jets. As can be seen, the data of the highest jet to counterflow velocity ratio ($U_r = 14$) fall well into the the linear growth rate given by the solid line ($y_{_{1/2}}/x = 0.104$) up to approximately $x/x_p < 0.3$. Lam and Chan (2002) presented an experimental investigation on the time-averaged concentration field of a counterflowing jet, where the growth of the counterflowing jet was shown to follow the linear growth rate of a simple jet for $x/x_p < 0.5$.It was

stated that the data of high jet to counterflow velocity ratios (U_r = 10 and 12), within $x/x_p < 0.5$, were well represented by the slope of 0.127, given by Fischer et al. (1979). Interestingly, the definition used by Fischer et al. (1979) for the width of the jet was not the same as the definition used by Lam and Chan (2002). Fischer et al. (1979) defined the width of the jet as the radial position at which C takes the value of e^{-1} C_c, where C_c is the concentration at the centerline of the jet, defined in this investigation as $y_{_{1/e}}$. Lam and Chan (2002) defined the width of the jet as the radial position at which C takes the value of 0.5 C_c ($y_{_{1/2}}$,). Therefore, the data presented by Lam and Chan (2002) should not be compared with the mean value of the slope for a simple jet presented by Fischer et al. (1979).

Figure 4.13 shows the variation of the jet width $y_{_{1/2}}$ with the axial direction x. In this figure the maximum penetration of the jet (x_p) is used as the scaled factor of both the width of the jet and the axial location. This figure shows that the data of the different jet to counterflow velocity ratios for the two jet diameters roughly collapse onto a single curve for $x/x_p < 0.5$ for the different values of U_r. The open symbols represent the data of the nozzle diameter D_1 and the cross symbols the data of D_2.

Beltaos and Rajaratnam (1973) suggested an equation that represents the momentum jet growth, which was obtained based on a dimensional analysis. The equation proposed by Beltaos and Rajaratnam (1973) is

$$\frac{y_{_{1/2}}}{x_p} = \frac{0.20\ x/x_p}{\sqrt{\left(\frac{2.24}{x/x_p}\right)^{2/3} - 1}} \tag{4.3}$$

the previous equation was substantiated by the data of the velocity field of the counterflowing jet presented in the work of Beltaos and Rajaratnam (1973). In order to use this equation with the experimental data obtained for the growth of the concentration half width of the jet ($y_{_{1/2}}$), the factor that represents the ratio of the jet width for the mean concentration profile to the mean velocity profile is introduced to

Equation 4.3. Therefore, the previous equation can be written as

$$\frac{y_{1/2}}{x_p} = \eta \frac{0.20\ x/x_p}{\sqrt{\left(\frac{2.24}{x/x_p}\right)^{2/3} - 1}} \tag{4.4}$$

where the average value of η has been estimated to be approximately 1.19 (Fischer et al., 1979). The solid line shown in Figure 4.13 represents the modified empirical equation suggested by Beltaos and Rajaratnam (1973) (Equation 4.4). Equation 4.4 does not represent the data of the width of the jet for $x < 0.3x_p$. In this region the flow of the jet is considered to be the dominant flow, therefore one can expect the width of jet to be linearly proportional to the axial distance x. Figure 4.13 also depicts the result of the linear regression performed in the data for only 30 % of the total penetration. This region can be considered as the linear growth region of the counterflowing jet's half width. In the linear growth region the growth of the jet width of the combined data was found to follow a linear function given by

$$\frac{y_{1/2}}{x_p} = 0.003 + 0.126\left(\frac{x}{x_p}\right) \tag{4.5}$$

This equation is shown in Figure 4.13 by the broken line. For $x > 0.3x_p$ the growth of the jet width was found to be better represented by a power law equation of the form

$$\frac{y_{1/2}}{x_p} = 0.027 + 0.32\left(\frac{x}{x_p}\right)^{2.5} \tag{4.6}$$

The previous equation is depicted in Figure 4.13 by the dash-dot line. It is possible to divide the growth of the jet width of a counterflowing jet into two different regions. The first region, the linear growth region that was found for $x < 0.3x_p$, and the second, the power law growth region that was observed for axial distances within $0.3x_p < x < 0.6x_p$.

Based on Figure 4.13 it is possible to suggest that the growth of the counterflowing

jet is proportional to x^1 up to 30 % of the total penetration length, which is the typical growth rate of a circular jet in a quiescent surroundings (Schlichting, 1979). Then, the rate of growth of the counterflowing jet shows a significant increment. This can be justified by the fact that at this point the flow of the jet has been decelerated by the counterflowing stream giving this more time for the jet flow to mix with the counterflowing stream. Additionally, the pressure field decelerates the jet fluid down as it approaches the stagnation point at the penetration distance x_p. This causes the jet streamlines to diverge as the jet slows down and produces radial spreading even in the absence of entrainment of fluid from the counterflow stream.

In the linear growth region, the slope of the jet width growth for the combined data was found to agree with the value presented in the investigation carried out by Wilson and Danckwerts (1964) for the concentration field of a simple turbulent jet. In this investigation the slope of the jet width growth was found to be 0.130. Despite the fact that the slope of the combined data in the linear growth region follows the linear growth of a simple jet, it is important to mention that the data in this region showed a significant amount of scatter around the linear regression. This can be observed in Figure 4.14 which depicts the jet width data in the linear growth region. A linear regression was performed for every jet to counterflow velocity ratio with the nozzle diameter D_1, and it was found that the individual slopes of every U_r for the jet width growth were found to be within the range of values given by the investigations of Kiser (1963), Wilson and Danckwerts (1964), and Becker et al. (1967).

As was mentioned previously, the jet width is also commonly defined by $y_{1/e}$ (Fischer et al., 1979). Therefore, the variation of $y_{1/e}$ with x at different jet to counterflowing velocity ratios was investigated. Figure 4.15 shows the variation of the jet width $y_{1/e}$ along the centerline of the jet, normalized by the maximum axial penetration. It is possible to observe from Figure 4.15 that the data collapsed into a single curve with slightly less scatter than the one shown in Figure 4.13. However, similar to the data shown in Figure 4.13, the growth of the jet width showed both linear and power law

growth regimes. The linear growth region of the jet width $y_{1/e}$ is represented by the function of the form

$$\frac{y_{1/e}}{x_p} = 0.004 + 0.158\left(\frac{x}{x_p}\right) \tag{4.7}$$

while the equation of the power law function that represents the growth of the jet width for $x > 0.3x_p$ up to $x = 0.6x_p$ is given by

$$\frac{y_{1/e}}{x_p} = 0.031 + 0.46\left(\frac{x}{x_p}\right)^{2.5} \tag{4.8}$$

The slope of the linear fit given by Equation 4.7 agrees with some of the values presented in Fischer et al. (1979). Fischer et al. (1979) presented a list with the slope of the jet width growth obtained by several investigators, in this list the values of the slope of the jet width growth goes from 0.101 to 0.156. Individual fits at every jet to counterflow velocity ratio were obtained within the linear growth region. Most of the slopes found for $y_{1/e}/x$ at every U_r fall well into the range of values given by Fischer et al. (1979). For the case of the nozzle diameter D_2 and $U_r = 8$, the value of the rate of growth for $y_{1/2}/x$ was found to be slightly above the reported values for a simple jet. This value can be compared with the one presented by Wilson and Danckwerts (1964), which was approximately 0.130. Another discrepancy was observed for the rate of growth of $y_{1/e}$ for the jet with nozzle diameter D_2 and U_r equal to 8 and 11 respectively. The slopes at these conditions were found to be above the maximum slope reported by Fischer et al. (1979). However, it is important to indicate that the values of the slopes found for $y_{1/2}$ and $y_{1/e}$ using the combined data are comparable to that of a simple jet (Wilson and Danckwerts 1964; Fischer et al. 1979). The calculated values of slopes for every flow condition can be found in Table 4.3.

Table 4.3: Slopes of the growth rate concentration jet width within the linear growth region for the counterflowing jet.

Jet Nozzle	U_r	$y_{1/2}/x$	$y_{1/e}/x$
8.81 mm	4	0.119	0.156
	8	0.127	0.156
	11	0.108	0.135
	12	0.109	0.132
	14	0.109	0.136
5.64 mm	8	0.148	0.182
	11	0.127	0.170
	14	0.123	0.152
	16	0.113	0.146
	19	0.117	0.148
Combined data$^+$		0.126	0.158

$^+$ The values of the slope found were obtained by doing a linear regression considering the data of the two different jet diameters, in order to obtain an overall slope for the growth of the jet width.

4.3.2 Counterflowing jet spreading in the mixing zone

Figure 4.16 depicts the normalized radial concentration profiles at different axial locations within the mixing zone. In this figure the data of the profiles at $U_r = 12$ were not included, since the properties of the profiles obtained at this U_r, are very similar to the one found at $U_r = 11$. The radial profiles shown in Figure 4.16 were obtained in the mixing zone, this is for axial locations within $0.7x_p < x < x_p$. In this figure it is possible to observe that the concentration level at the beginning of the mixing zone decreases for higher values of U_r. It can be seen that for the case of $U_r = 4$ the concentration at the initial region of the mixing zone is approximately 30 % of the concentration at the exit of the jet. Meanwhile, for the case of U_r equal to 8, 11, and 14, the concentration levels were found to be 18, 14 and 11 % of the the concentration at the exit of the jet. Unlike the case of the established flow region, the radial profiles of the concentrations at $U_r = 4$ do not resemble a Gaussian distribution. The approximate Gaussian form is lost while increasing the jet to counterflowing velocity ratio, Figure 4.16d shows that the radial profiles can be represented by a linear equation. From Figure 4.16 it is possible to observe that the radial spread of the mixing zone is

affected by the value of U_r, the higher the value of U_r the wider is the mixing zone.

Similar to the profiles of the established flow region, the profiles obtained within the mixing zone were plotted in a dimensionless form. The radial concentration was normalized by the concentration at the centerline of the jet and the radial location was normalized by $y_{_{1/2}}$. Figure 4.17 depicts the dimensionless radial concentration profiles of the counterflowing jet in the mixing zone. For the case of $U_r = 4$ the radial concentration profiles collapse onto a single curve for radial distances of $y_{_{1/2}} < 1.25$. At a higher jet to counterflowing velocity ratio, $U_r = 8$, the data roughly fell into a single curve for $y_{_{1/2}} < 1.5$. It was surprising to observe the corresponding data for $U_r = 11$ scattering around a single curve for the total length of the radial profile. However, for the case of $U_r = 14$ the dimensional radial concentration profiles collapsed into what seemed to be a linear equation instead of the Gaussian form presented in Figure 4.17a, 4.17b, and 4.17c. This Gaussian distribution is given by

$$\frac{C_y}{C_c} = \exp\left[-\frac{3}{5}\left(\frac{y}{y_{_{1/2}}}\right)^2\right] \tag{4.9}$$

from Figure 4.17 it is possible to appreciate that the data in the mixing zone collapses into a Gaussian distribution similar to the one observed in the established flow region. The unstable nature of the mixing zone significantly affects the quality of the data and the results obtained in this region, which can be observed in Figure 4.16 and Figure 4.17. It is possible to speculate that the quality of the data in this region should improve if the sample rate corresponds to the frequency of the fluctuations and if the integration time is long enough to overcome the effect of these fluctuations.

4.4 Conclusion

This is study has experimentally investigated the spreading of the counterflowing jets on the established flow region and the mixing zone. Several length scales have been proposed for the characterization of the jet spread. They include, among others, the

axial penetration x_p, which has been the primary focus of previous studies cited in the literature. The following conclusions may be drawn from the quantitative comparison of the length scales studied here:

1. The new geometrical scales were able to generate a universal form of the spreading of the jet for a significant distance in the radial direction, which has been previously defined as the inner region of the jet.

2. The growth of the concentration jet width of the counterflowing jet was found to be divided into two regions: the linear growth region, and the power law growth region. In the linear growth region the jet width grows linearly with the axial distance downstream from the exit of the jet, up to 30 % of the total jet penetration. In average the values of the slope in the linear growth region were found to be similar to the rate of growth of a free jet, with a value of 0.126. The power law growth region was found at axial distances $0.3\ x_p < x \leq 0.6\ x_p$, and the jet width growth is given by a power law function with a $x^{2.5}$ dependence.

3. The spreading of the jet in the mixing zone was found to be affected by the fluctuations of the counterflowing jet. Although the trend in radial concentration is incomparable for all velocity ratios, there is clearly a portion of the data that follows a Gaussian distribution.

References

Becker, H. A., Hottel, H. C., and Williams, G. C. (1967). The nozzle-fluid concentration field of the round turbulent, free jet. *Journal of Fluid Mechanics*, 30(2):285 – 303.

Beltaos, S., Brinkworth, B. J., Lam, K. M., and Chan, H. C. (1999). Round jet in ambient counterflowing stream. *Journal of Hydraulic Engineering*, 125(4):428 – 432.

Beltaos, S. and Rajaratnam, N. (1973). Circular turbulent jet in an opposing infinite stream. *First Canadian Hydraulics Conference, Edmonton*.

Chan, H. C. (1999). *Investigation of a round jet into a counterflow*. PhD thesis, Dept. of Civil Engineering, University of Hong Kong.

Chan, H. C. and Lam, K. M. (1998). Centerline velocity decay of a circular jet in a counterflowing stream. *Physics of Fluids*, 10(3):637 – 644.

Fischer, H. B., List, E. J., Imberger, J., and Brooks, N. H. (1979). *Mixing in inland and coastal waters*. Academic Press, Inc.

Hilderman, T. L. (2004). *Measurement, modelling, and stochastic simulation of concentration fluctuations in a shear flow*. PhD thesis, University of Alberta.

Kiser, K. M. (1963). Material and momentum transport in axisymmetric turbulent jets of water. *A.I.Ch.E. Journal*, 9(3):386 – 390.

König, O. and Fiedler, H. E. (1991). The structure of round turbulent jets in counterflow: a flow visualization study. *Advances in turbulence 3*, pages 61 – 66.

Lam, K. M. and Chan, C. H. C. (2002). Time-averaged mixing behavior of circular jet in counterflow: Velocity and concentration measurements. *Journal of Hydraulic Engineering*, 128(9):861 – 865.

Lam, K. M. and Chan, H. C. (1995). Investigation of turbulent jets issuing into a counterflowing stream using digital image processing. *Experiments in Fluids*, 18:210 – 222.

Lee, J. H. W. and Chu, V. H. (2003). *Turbulent jets and plumes: a Lagrangian approach*. Kluwer Academic Publishers.

Pope, S. B. (2000). *Turbulent flows*. Cambridge University Press, 4th edition.

Powell, I. (1987). Design of a laser beam line expander. *Applied Optics*, 26(17):3705 – 3709.

Schlichting, H. (1979). *Boundary-layer theory.* McGraw-Hill, Inc.

Walker, D. A. (1987). A fluorescence technique for measurement of concentration in mixing liquids. *Journal of Physics E Scientific Instruments*, 20:217 – 224.

Wilson, R. A. M. and Danckwerts, P. V. (1964). Studies in turbulent mixing - II. *Chemical Engineering Science*, 19(11):885 – 895.

Wood, I. R. (1993). Asymptotic solutions and behavior of outfall plumes. *Journal of Hydraulic Engineering*, 119(5):555 – 580.

Yoda, M. and Fiedler, H. E. (1996). The round jet in a uniform counterflow: flow visualization and mean concentration measurements. *Experiments in Fluids*, 21(6):427 – 436.

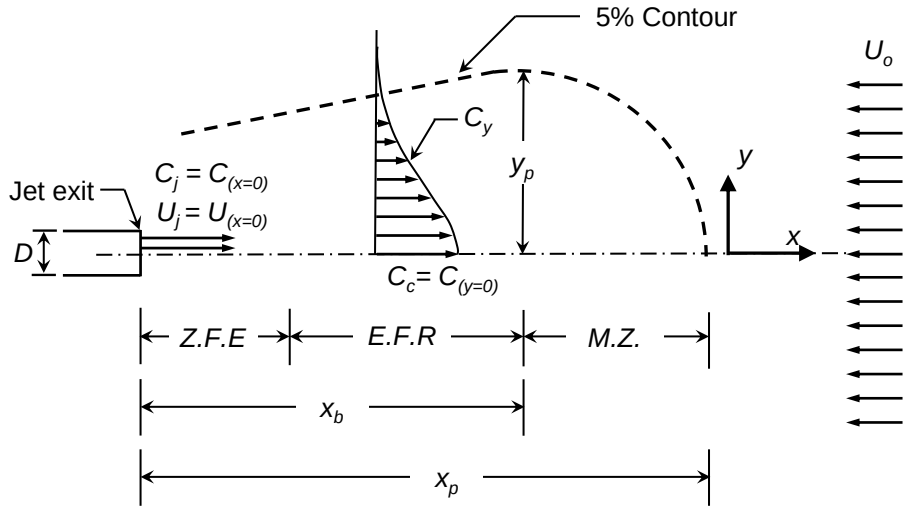

Figure 4.1: Schematic of the geometric parameters in the counterflowing jet (after Beltaos and Rajaratnam (1973), Yoda and Fiedler (1996), and Chan (1999)). Three different regions can be identified: the zone of flow establishment (ZFE), the established flow region (EFR), and the mixing zone (MZ).

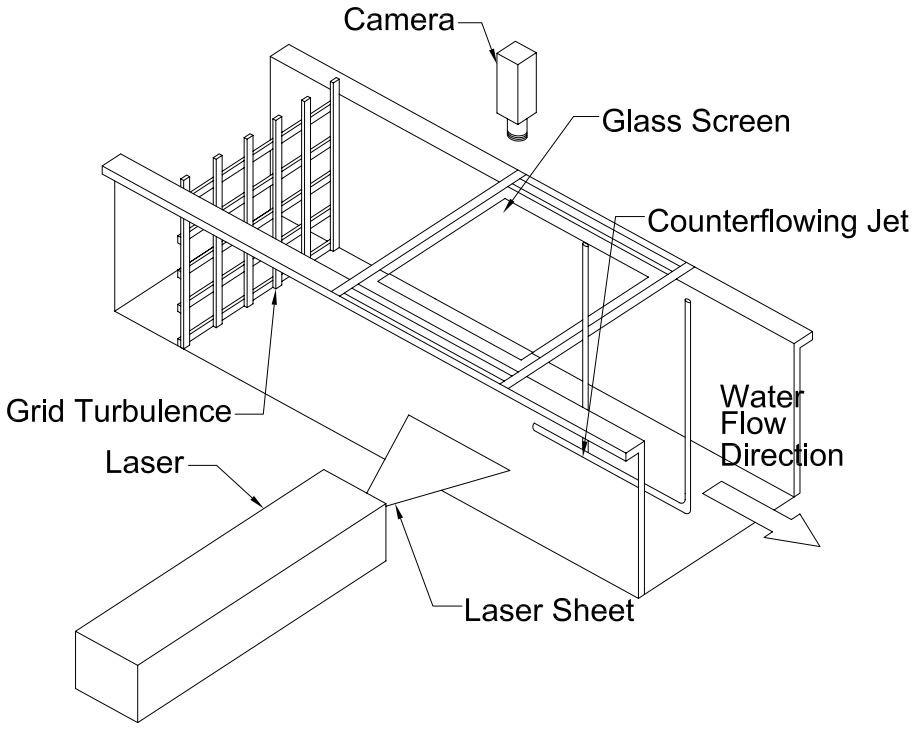

Figure 4.2: Schematic of the experimental setting used to measure the concentration field of the counterflowing jet.

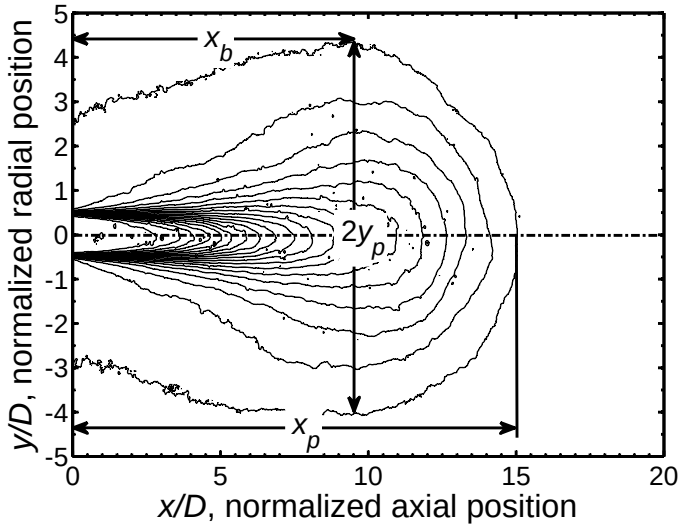

Figure 4.3: Example of the length parameters measured using the 5 % concentration contour for the counterflowing jet for $U_r = 4$, with a jet diameter D_1.

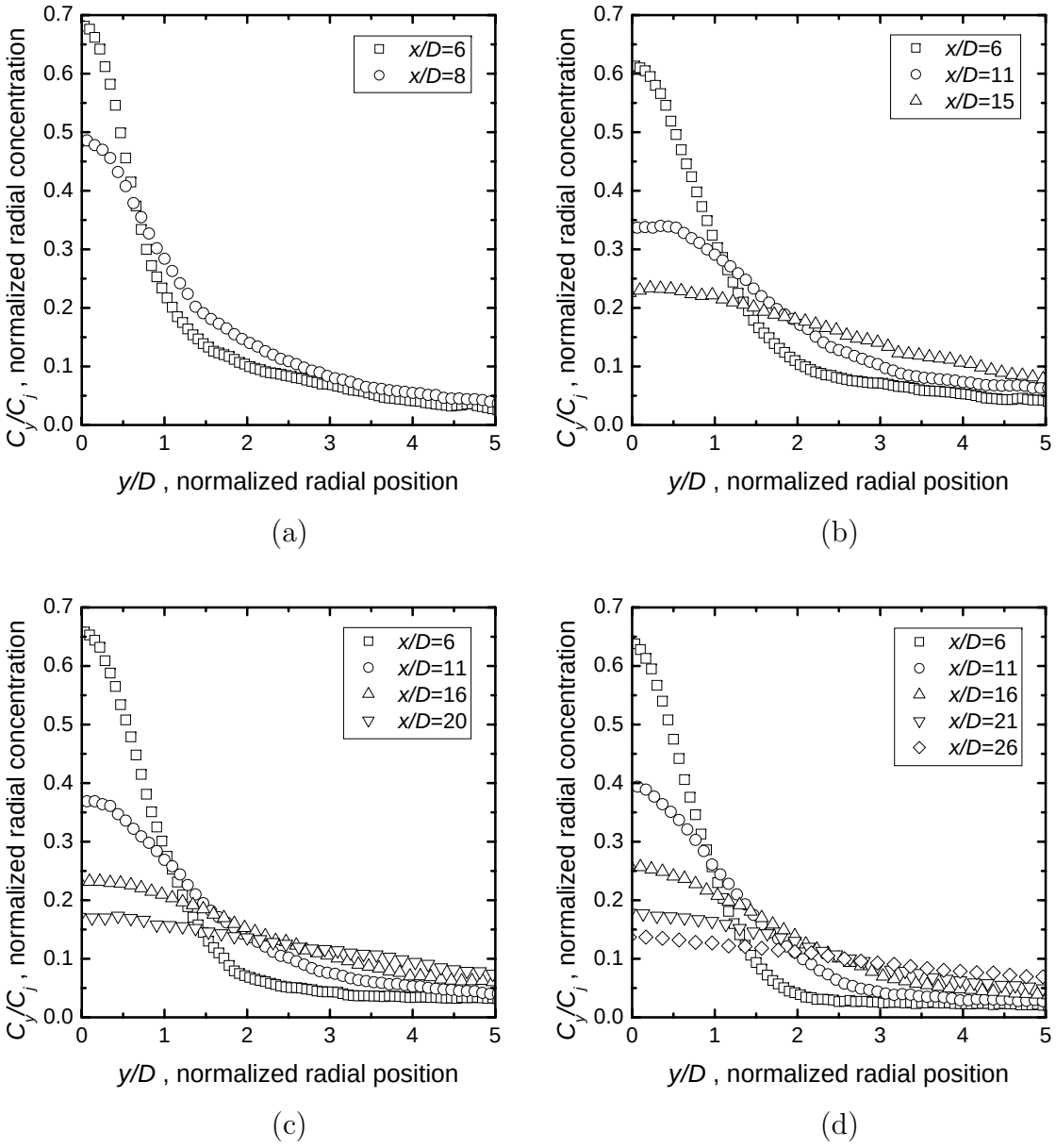

Figure 4.4: Radial concentration profile of the counterflowing jet at $Ur = 4$ (a), $Ur = 8$ (b), $Ur = 11$ (c) and $Ur = 14$ (d). The jet diameter of the nozzle used was 8.81 mm. The radial concentration is normalized by the concentration at the exit of the nozzle. The profiles are obtained within the established flow region of the counterflowing jet.

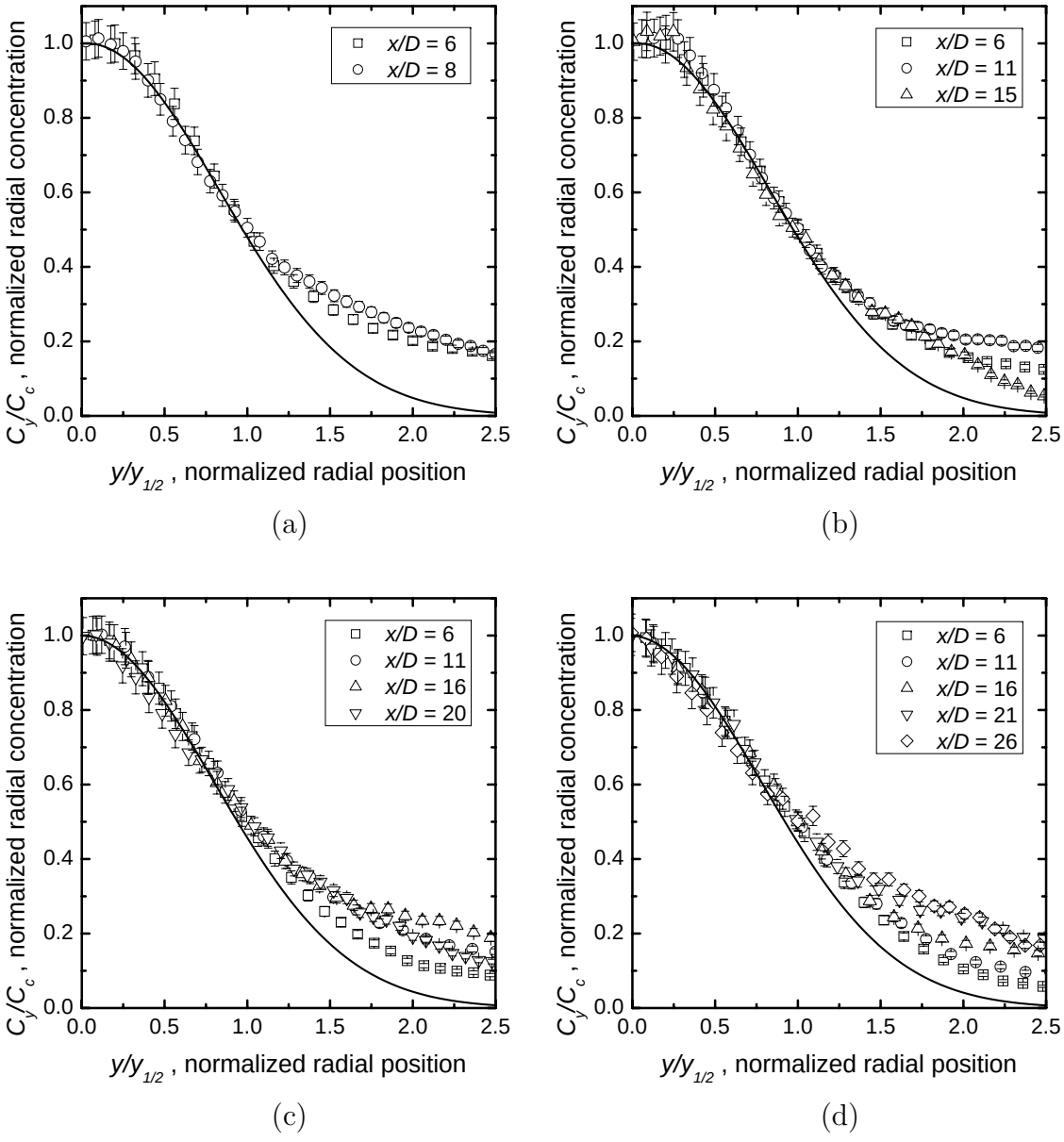

Figure 4.5: Self similarity of the radial concentration profiles of the counterflowing jet at $Ur = 4$ (a), $Ur = 8$ (b), $Ur = 11$ (c) and $Ur = 14$ (d). The jet diameter of the nozzle used was 8.81 mm. The radial concentration is normalized by the concentration at the geometrical centerline of the nozzle. The radial coordinates are normalized by the the jet width, which correspond to the location at which the radial concentration is equal to half the centerline concentration. The solid curve represents a Gaussian distribution.

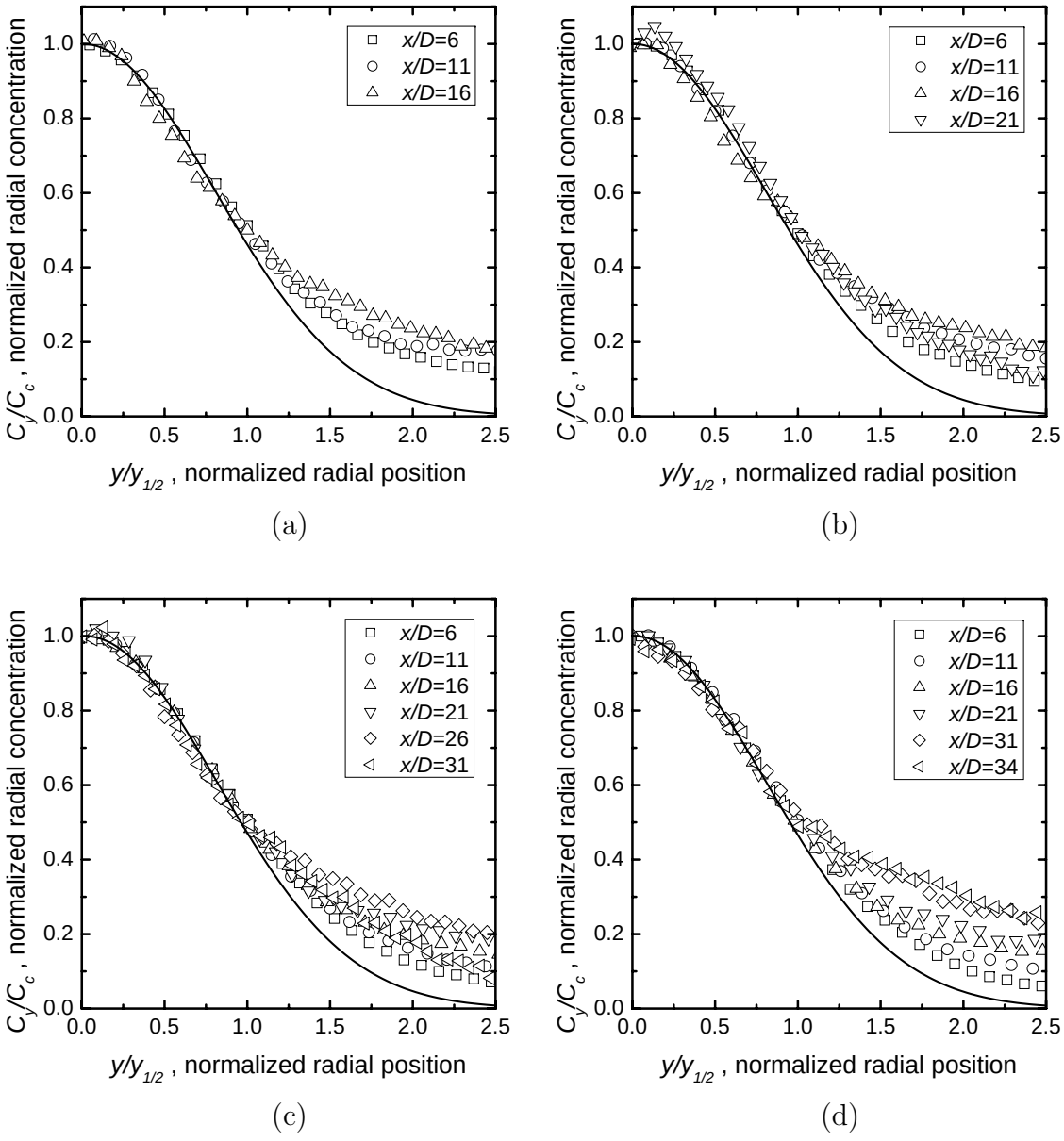

Figure 4.6: Self similarity of the radial concentration profiles of the counterflowing jet at $Ur = 11$ (a), $Ur = 14$ (b), $Ur = 16$ (c) and $Ur = 19$ (d). The jet diameter of the nozzle used was 5.64 mm. The radial concentration is normalized by the concentration at the geometrical centerline of the nozzle. The radial coordinates are normalized by the jet width, which correspond to the location at which the radial concentration is equal to half the centerline concentration. The solid curve represents a Gaussian distribution. The error bars of the data are approximately the size of the symbols; an example of this can be seen in Figure 4.5.

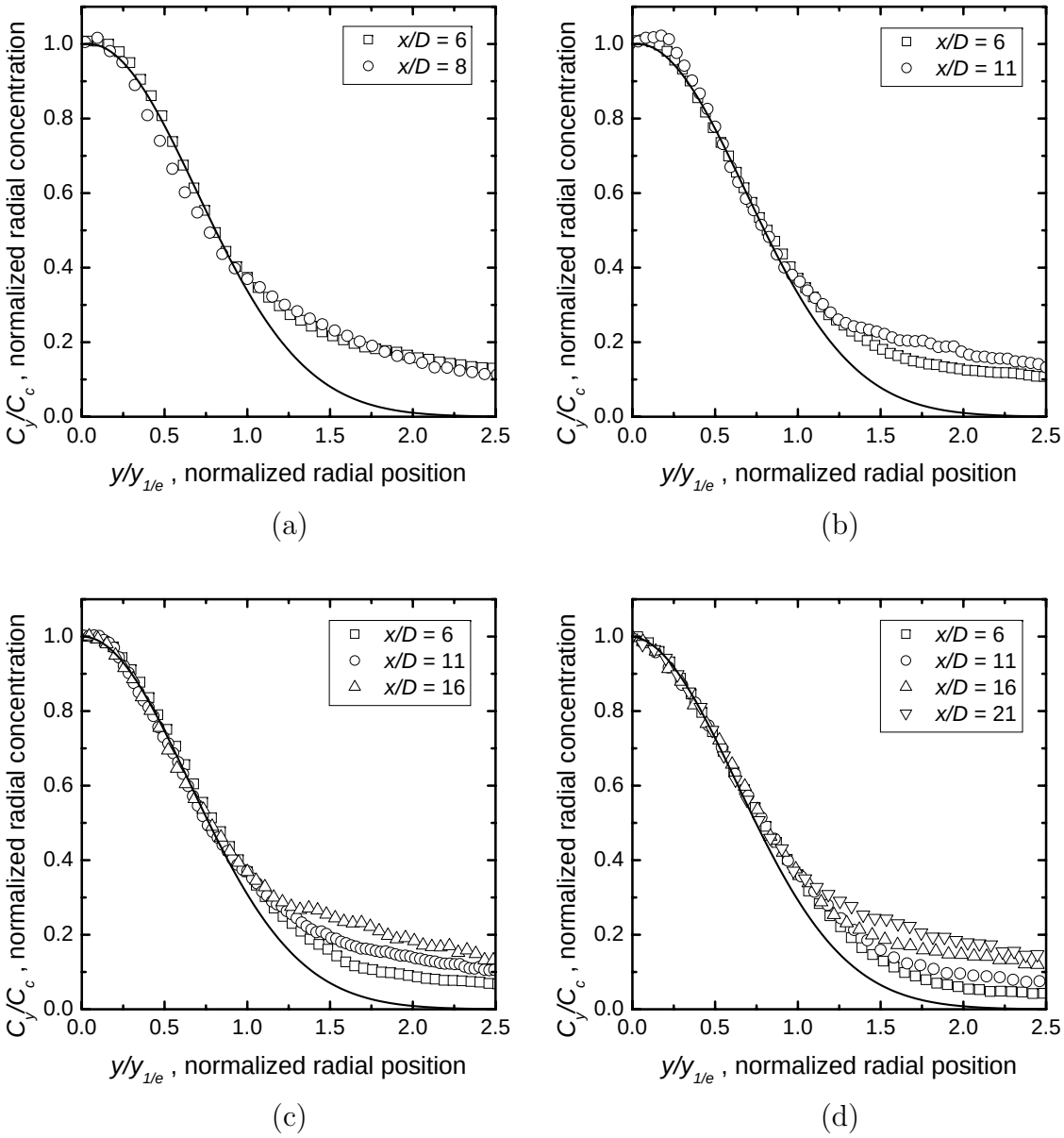

Figure 4.7: Self similarity of the radial concentration profiles of the counterflowing jet at $Ur = 4$ (a), $Ur = 8$ (b), $Ur = 11$ (c) and $Ur = 14$ (d). The jet diameter of the nozzle used was 8.81 mm. The radial concentration is normalized by the concentration at the geometrical centerline of the nozzle. The radial coordinates are normalized by the distance at which the concentration is equal to e^{-1} times the concentration at the centerline. The solid curve represents a Gaussian distribution. The error bars of the data are approximately the size of the symbols; an example of this can be seen in Figure 4.5.

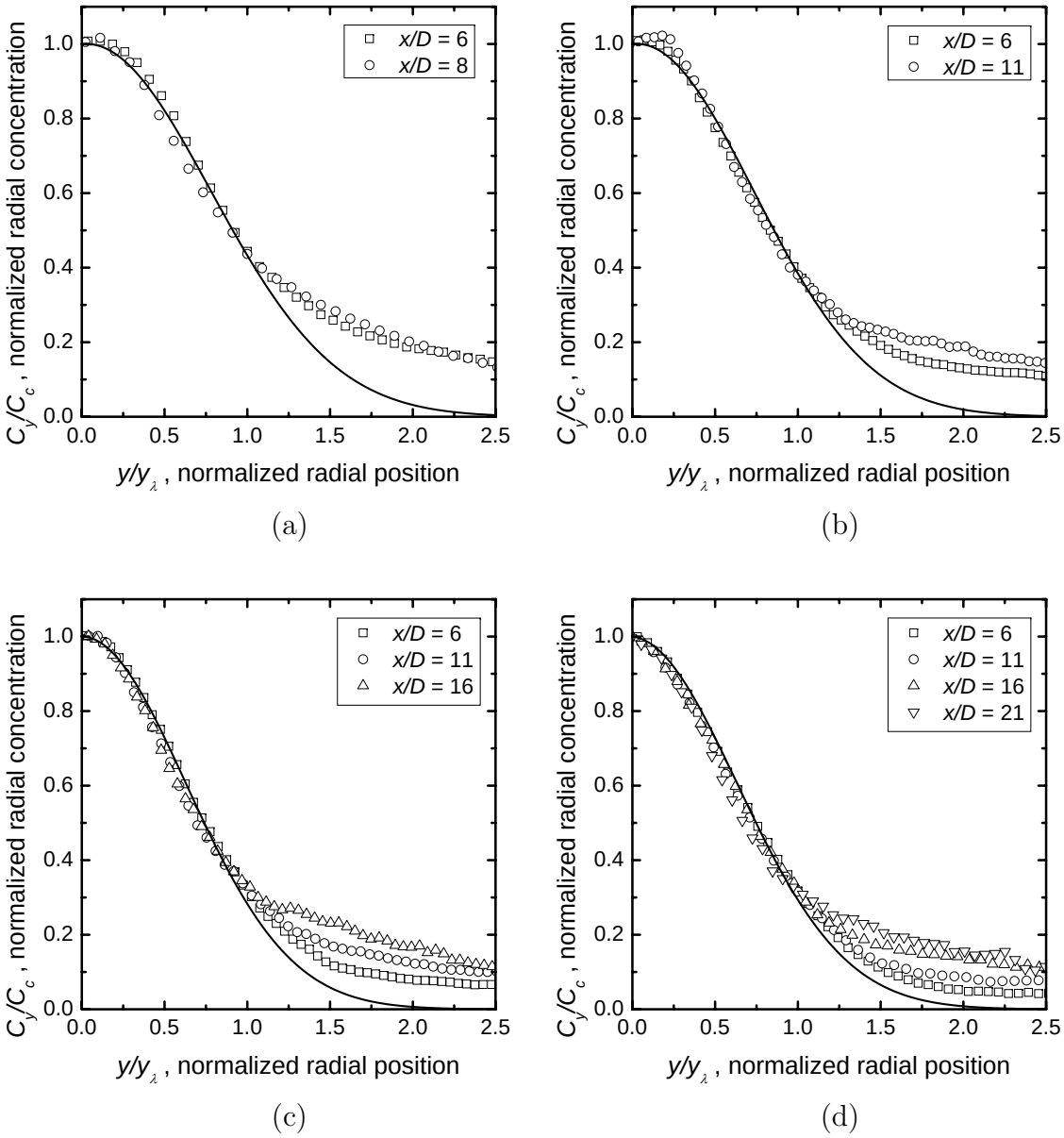

Figure 4.8: Self similarity of the radial concentration profiles of the counterflowing jet at $Ur = 4$ (a), $Ur = 8$ (b), $Ur = 11$ (c) and $Ur = 14$ (d). The jet diameter of the nozzle used was 8.81 mm. The radial concentration is normalized by the concentration at the geometrical centerline of the nozzle. The radial coordinates are normalized by the distance at which the concentration is equal to λ times the concentration at the centerline. The solid curve represents a Gaussian distribution. The error bars of the data are approximately the size of the symbols; an example of this can be seen in Figure 4.5.

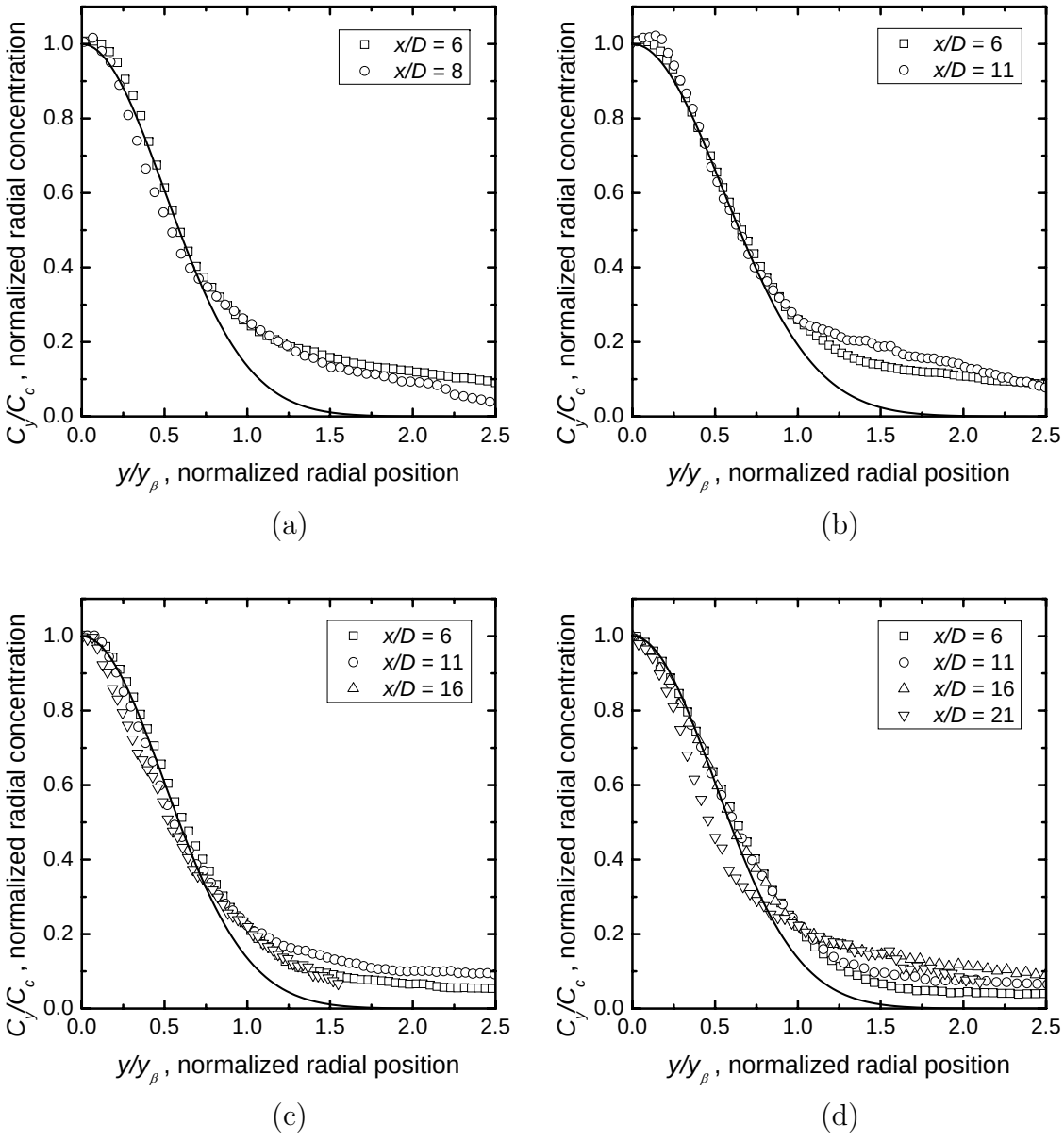

Figure 4.9: Self similarity of the radial concentration profiles of the counterflowing jet at $Ur = 4$ (a), $Ur = 8$ (b), $Ur = 11$ (c) and $Ur = 14$ (d). The jet diameter of the nozzle used was 8.81 mm. The radial concentration is normalized by the concentration at the geometrical centerline of the nozzle. The radial coordinates are normalized by the distance at which the concentration is equal to β times the concentration at the centerline. The solid curve represents a Gaussian distribution. The error bars of the data are approximately the size of the symbols; an example of this can be seen in Figure 4.5.

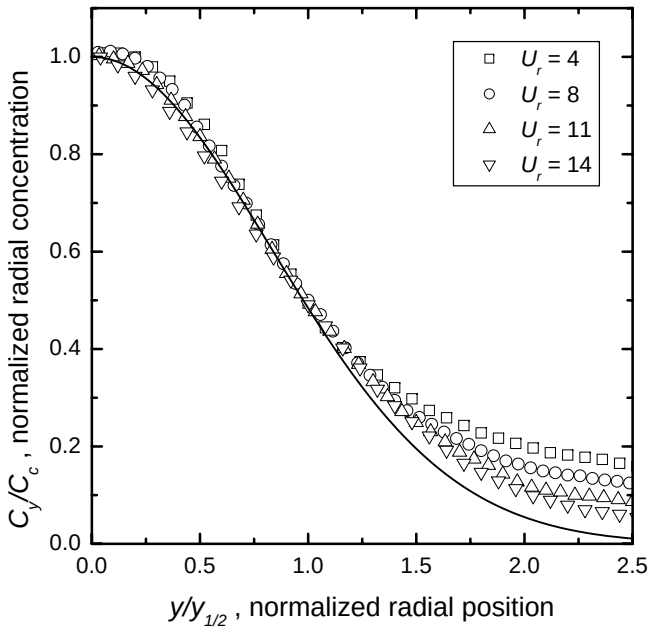

Figure 4.10: Dimensionless radial concentration profiles of the counterflowing jet at 6D downstream from the exit of the jet; $y_{1/2}$ is used as the scale for the radial location. The error bars of the data are approximately the size of the symbols, an example of this can be seen in Figure 4.5.

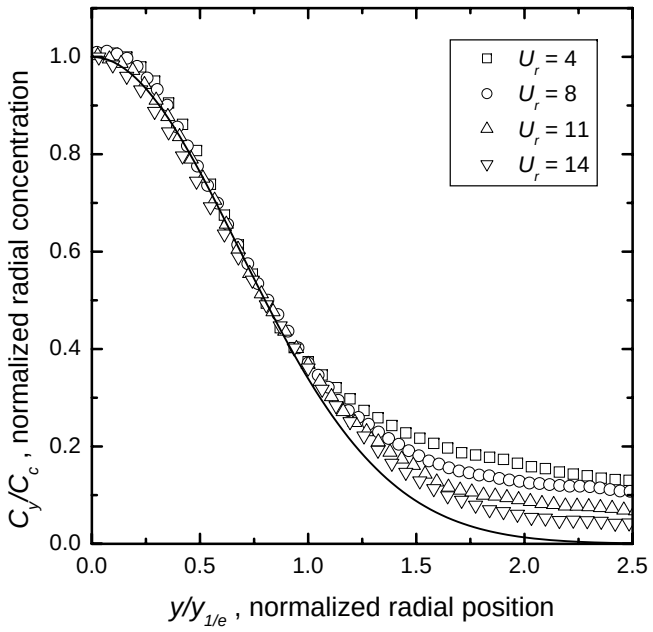

Figure 4.11: Dimensionless radial concentration profiles of the counterflowing jet at 6D downstream from the exit of the jet; $y_{1/e}$ is used as the scale for the radial location. The error bars of the data are approximately the size of the symbols, an example of this can be seen in Figure 4.5.

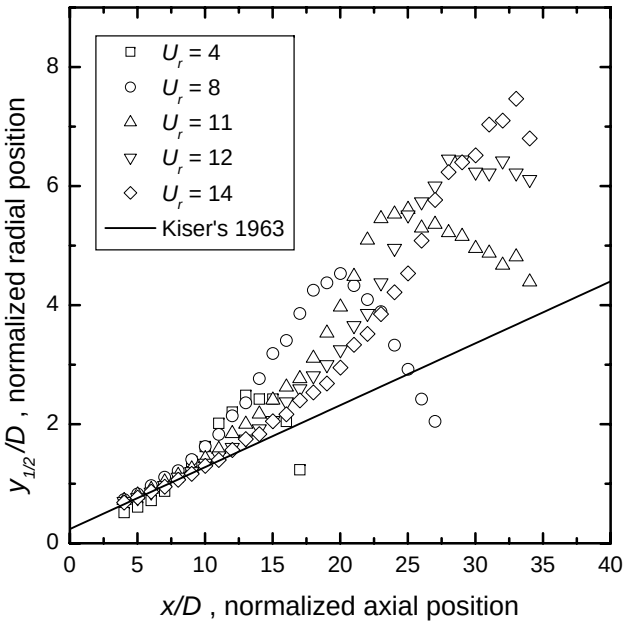

Figure 4.12: Concentration jet width ($y_{1/2}$) of the counterflowing jet at different U_r. The diameter of the nozzle used was equal to 8.81 mm (D_1). The solid line corresponds to the growth rate found by Kiser (1963).

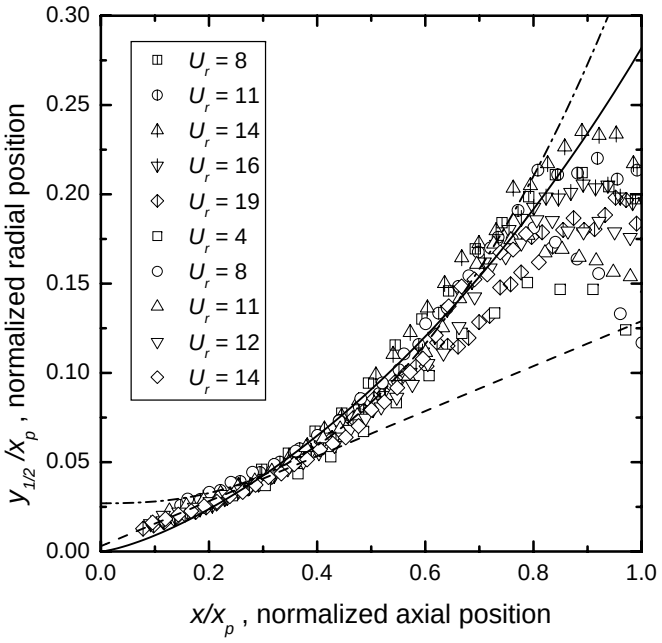

Figure 4.13: Concentration jet width ($y_{1/2}$) of the counterflowing jet at different U_r. Solid line represents the modified empirical equation given by Beltaos and Rajaratnam (1973). The broken line corresponds to the linear equation found for the linear growth region of the counterflowing jet (Equation 4.5). The dash-doted line is the experimental equation obtained for the power law growth region of the jet (Equation 4.6). Open symbols D = 8.81 mm and cross symbols D = 6.54 mm.

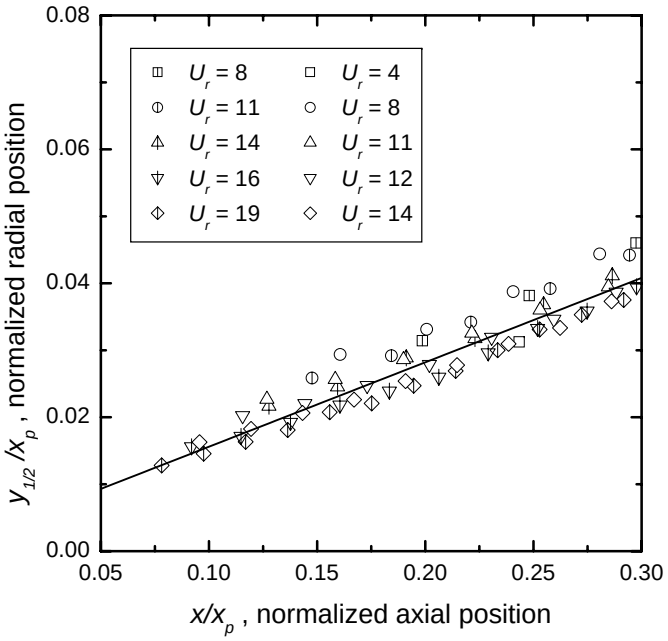

Figure 4.14: Concentration jet width ($y_{1/2}$) of the counterflowing jet at different U_r in the linear growth region. The solid line is given by Equation 4.5. Open symbols D = 8.81 mm and cross symbols D = 6.54 mm.

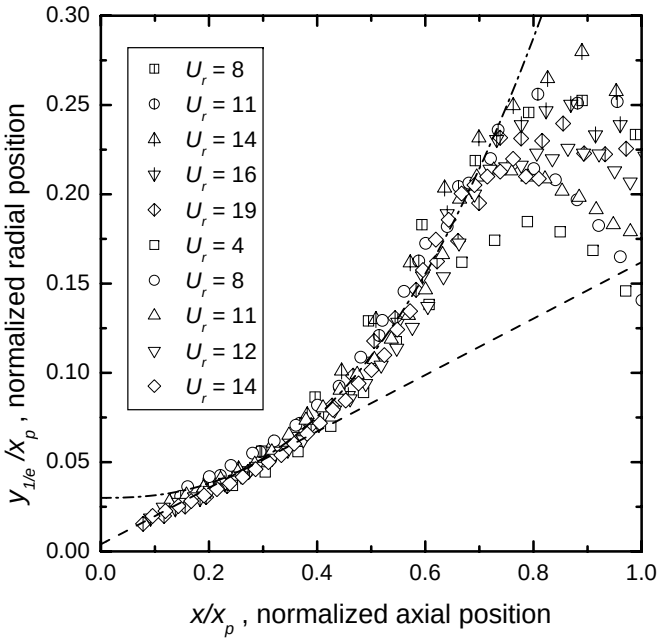

Figure 4.15: Concentration jet width ($y_{1/e}$) of the counterflowing jet at different U_r. The broken line corresponds to the linear equation found for the linear growth region of the counterflowing jet (Equation 4.7). The dash-doted line is the experimental equation obtained for the power law growth region of the jet (Equation 4.8). Open symbols represent the data of jet with diameter D = 8.81 mm and cross symbols the nozzle with D = 6.54 mm.

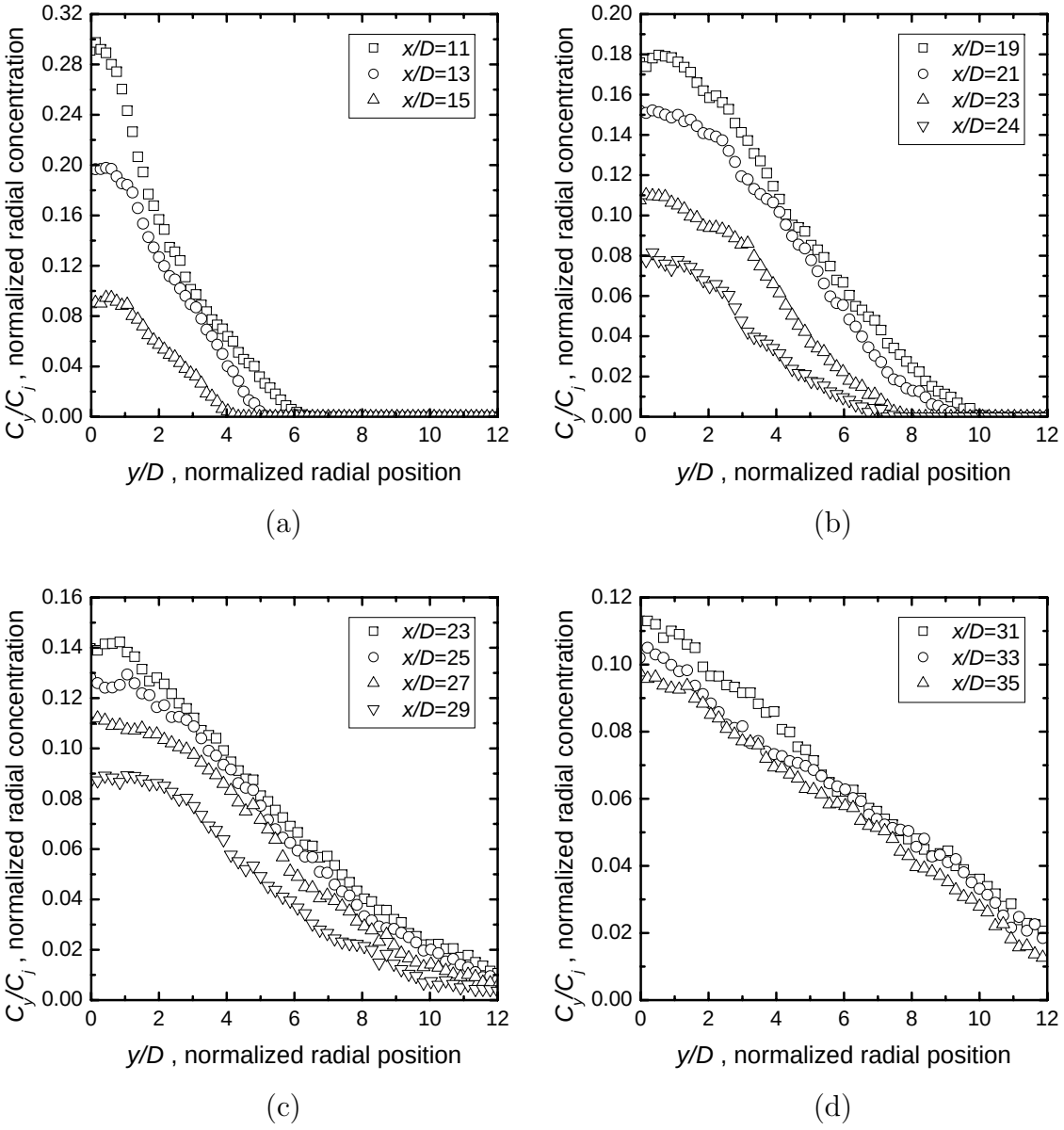

Figure 4.16: Radial concentration profiles of the counterflowing jet at $Ur = 4$ (a), $Ur = 8$ (b), $Ur = 11$ (c) and $Ur = 14$ (d). The jet diameter of the nozzle used was 8.81 mm. The radial concentration is normalized by the concentration at the exit of the nozzle. The profiles are obtained within the mixing zone of the counterflowing jet. The error bars of the data are approximately the size of the symbols; an example of this can be seen in Figure 4.5.

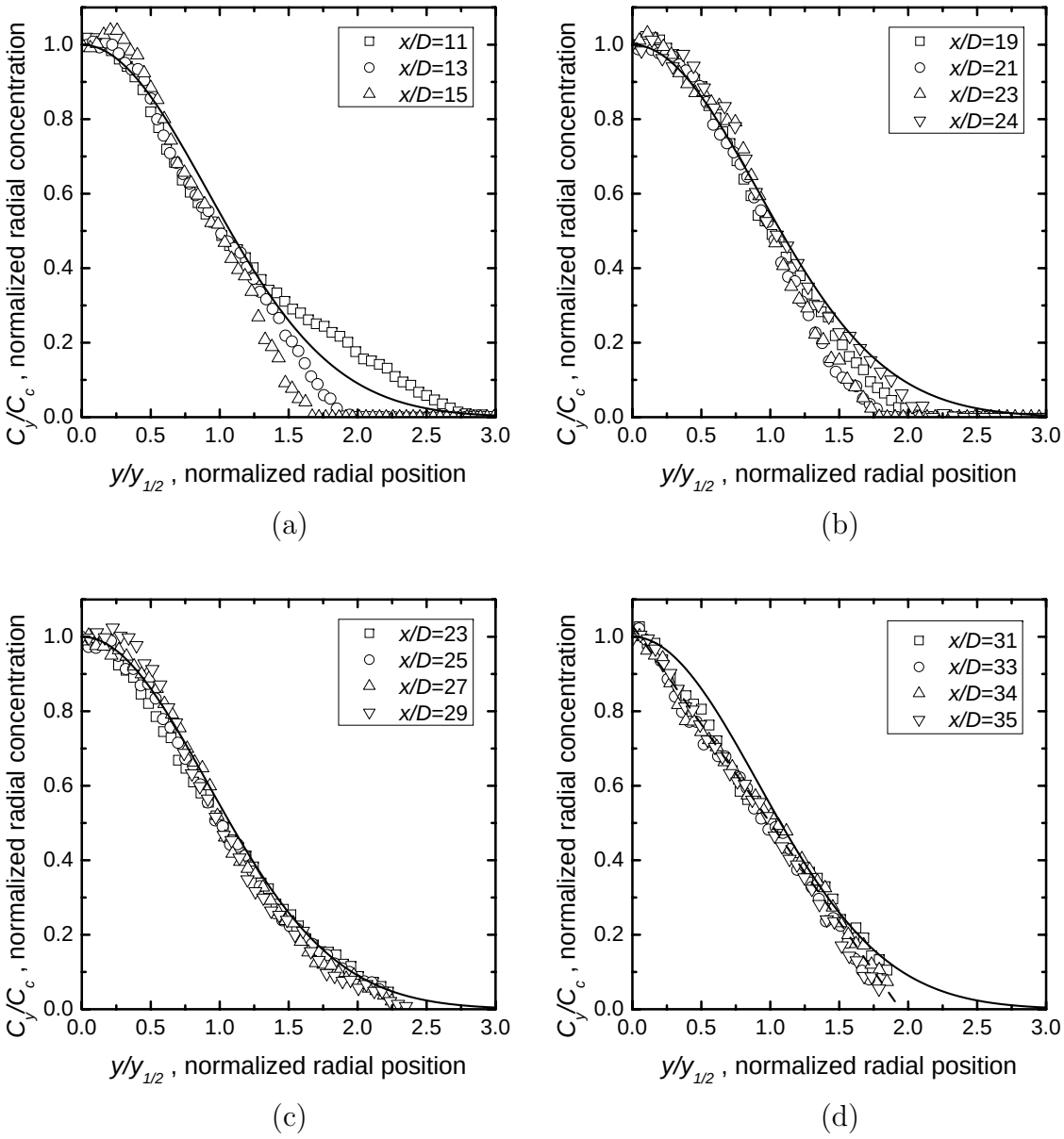

Figure 4.17: Self similarity of the radial concentration profiles of the counterflowing jet at $Ur = 4$ (a), $Ur = 8$ (b), $Ur = 11$ (c) and $Ur = 14$ (d). The data were obtained using the nozzle with diameter D = 8.81 mm. The solid curve represents a Gaussian distribution. The error bars of the data are approximately the size of the symbols; an example of this can be seen in Figure 4.5.

Chapter 5

Experimental study of small inlet yaw angle effect in the flow of the counterflowing jet

Abstract

The effects of small inlet yaw angles in the mean concentration field of an axisymmetric round jet in a uniform counterflow was investigated using planar laser induced fluorescence. The concentration field was studied at different jet to counterflow velocity ratios ranging from 4 to 19, using two different diameters of the jet nozzle. The velocity ratios were chosen to be in the low jet to counterflow momentum ratio. The universal form of the centerline concentration decay and the similarity region of the counterflowing jet were investigated.

It was found that the inlet yaw angles of the jet had a significant influence on the penetration length of the jet. The centerline of the jet was found to be affected by the yaw angle, as well as the direction of the fluctuations of the jet. The centerline concentration decay of the counterflowing jet with small inlet yaw angles showed similar characteristics as a jet with no inlet yaw angle, when the location is normalized by the penetration length. The mean field radial spreading and axial penetration of the counterflowing jet are investigated with respect to the jet to counterflow velocity ratios.

5.1 Introduction

The counterflowing jet can be defined as the flow created by a jet issuing into a uniform opposed stream. This jet is known for its ability to enhance the mixing efficiency when it is compared with the well known jets in co and cross flow (Beltaos and Rajaratnam, 1973; Bernero and Fiedler, 2000). Jets in a counterflow stream are commonly found in industrial applications that require enhanced mixing, as is the case in environmental fluid applications (Beltaos and Rajaratnam, 1973; Lam and Chan, 1995; Chan, 1999). Despite this fact, the characteristics of this flow have been the subject of few investigations. Within them, the most common investigations are related to the study of the penetration length, jet fluctuations, spreading of the jet in the radial direction and centerline concentration decay. These studies can be found in the investigations presented by Timma (1962), Beltaos and Rajaratnam (1973), Morgan and Brinkworth (1976), König and Fiedler (1991), Chan (1999), within others. The effects of small inclination of the jet nozzle (inlet yaw angle) of a water jet has not been sufficiently studied. An investigation into the effects of slight inclinations of the jet with respect to the counterflowing jet is presented by Yoda and Fiedler (1996). Yoda and Fiedler (1996) employed planar laser induced fluorescence to obtain information of mean concentration measurement of the jet in a uniform counterflow stream. However, no information on the effect on the centerline concentration decay nor the spreading of the jet are given in the work presented by Yoda and Fiedler (1996). In this study the effects of the small yaw angles were focused in the penetration length of the jet and the effect on the fluctuations of the jet.

In this chapter, planar laser induced fluorescence is used to investigate the effect of small yaw angles in the penetration length, in order to investigate and understand the sensitivity to small changes as is the case of discharge into rivers. Counterflowing jets with inlet yaw angles of 4 and 8 degrees are compared with the counterflowing jet with a yaw angle of zero (aligned with counterflow stream). This study shows the effects of the yaw angle in the penetration length, centerline concentration decay,

and radial spreading of the counterflowing jet. The effects of the yaw angles are investigated for several jet to counterflowing velocity ratios, ranging from 4 to 19. The present investigation includes data from two different jet diameters: 8.81 mm and 5.64 mm. The data of the penetration length, centerline concentration decay and radial profiles of the mean concentration field of the jet with inlet yaw angles equal to 4 and 8 degrees are presented. The universal form of the centerline concentration decay as well as the similarity region of the radial profiles of the counterflowing jet is investigated for the counterflowing jet with small inlet yaw angle. In this chapter the applicability of the scaling factors used in the counterflowing jet with small inlet yaw angles is shown. The investigation of the effects of small inlet yaw angles

5.2 Experiment Setup and Techniques

A closed loop water channel was used as the experimental facility for all the experiments. This facility is located in the Mechanical Engineering Department at the University of Alberta. The channel has a total length of approximately 5000 mm, with a cross section of 680 mm wide by 480 mm high. The flow of the jet was generated by a cylindrical nozzle, that was located at approximately 3200 mm downstream from the inlet of the water channel. The jet was produced by using two cylindrical nozzles with an internal diameter of 8.841 and 5.64 mm, hereafter referred to as D_1 and D_2 respectively. The jets were designed to have an inlet length of 104D in order to obtain a fully developed flow at the exit of the nozzle. The jets were mounted in a rotating system that allows the jet to rotate around the vertical axis (perpendicular to the bottom of the water channel). The resolution given by the rotating system was found to be 0.5 degrees. A pressurized tank was used as the source for the jets. The gauge pressure in the tank was kept constant at 206.84 kPa. A calibrated rotameter was located at the inlet of the jet to obtain the desired velocity at the exit of the jet, the calibration curves for every jet diameter can be found in Figure B.1. The velocity of the counterflow stream was kept at a constant value of 5 $cm.s^{-1}$, therefore, just the velocity of the jet was modified in order to obtain the desired jet to counterflow

velocity ratios. The center of the jet nozzle was placed at approximately 200 mm from the bottom of the water channel. The level of the water in the channel was kept at a constant height of 400 mm.

A uniform grid was place at the inlet of the water channel (see Figure 2.14) built with flat stainless steel bars of 19.2 by 5 mm of cross section area. The total open area was approximately 56 % with a mesh spacing of 76.2 mm. This grid turbulence generates near uniform velocity profile for the streamwise component, with variations found to be within 5 % (Hilderman, 2004). At the test section the turbulence intensity was found to be about 4 % for the mean horizontal (Hilderman, 2004).

Planar laser induced fluorescein, was used to measure the axial and radial mean scalar concentration field. Fluorescein sodium salt was used as the tracer for all the experiments. The fluorescein sodium salt was added and mixed in the stainless steel tank that was used as the source for the jet. A fixed concentration of 0.05 $mg.L^{-1}$was used for all the experiments. The laser sheet of the planar laser induced fluorescence system was generated by a optical arrangement that includes a Powell lens®. The Powell lens®was able to generate a laser sheet with an approximately uniform distribution of the the light intensity. The thickness of the laser sheet was found to be approximately 1.6 mm. In order to avoid any distortion due to the waves generated at the suface of the water channel, a glass screen was place at the surface of the water (see Figure 5.1). A 12 bit SensiCam high speed CCD system was used as a light detector, with a resolution of 1280 x 1024 pixels. The specifications of this camera are shown in Table A.1. The maximum quantum efficiency of the camera is found to be approximately 500 nm, which is close to the spectrum emission of fluorescein sodium salt . The laser used in this investigation was a 2.1 W Argon ion laser, which was operated in a single mode at a wavelength of 488 nm. the wavelength used in the laser corresponds to the excitation wavelength of the fluorescein sodium salt. The system was calibrated before every experiment in order to obtain the correct information of the concentration field. This was obtained by using images of known tracer

concentrations that were produced by averaging a sequence of images of a specific dye concentration. These sequences were obtained by traversing a glass squared tube with a known concentration of dye along the camera field of view. As a result, a first degree polynomial was used to convert the fluorescent intensity into scalar concentration data (a detailed explanation of the calibration process can be found in Chapter 2).

Different jet to counterflow velocity ratios were tested for the two jets, D_1 and D_2. The velocity of the counterflow stream was kept at a constant value of 5 cm.s^{-1} as the velocity of the jet was adjusted to obtain the desired jet to counterflow velocity ratio. The angle of the jet with respect to the direction of the counterflow stream, the yaw angle, was also modified for every flow condition. These flow conditions were studied at inlet yaw angles equal to 0°, 4°, and 8°, which were conveniently chosen based on setup limitations. Table 5.1 resumes the initial jet conditions analyzed in this study. At every flow jet condition a set of 500 images was taken at a rate of 19.32 Hz, with a exposure time of 10 ms. The spatial resolution established for the experiments was approximately 0.3 mm.pixel^{-1}.

Table 5.1: Initial jet conditions of the counterflowing jet. These flow conditions were tested at yaw angles equal to 0°, 4°, and 8°.

D (mm)	U_j (m.s^{-1})	U_r	Re_D
8.81	0.18	4	1580
8.81	0.38	8	3330
8.81	0.53	11	4640
8.81	0.62	12	5430
8.81	0.67	14	5870
5.64	0.38	8	2130
5.64	0.53	11	2970
5.64	0.68	14	3810
5.64	0.81	16	4540
5.64	0.94	19	5270

5.3 Experimental Results

Time averaged concentration information was obtained from a sequence of 500 images taken from the instantaneous concentration field of the counterflowing jet. These average images were used to define the mean geometrical length of the counterflowing jet. Figure 5.2 depicts a schematic of the mean parameters of the counterflowing jet. These parameters were defined by the 5 % concentration contour. The 5 % contour was conveniently chosen since the maximum penetration distances defined by this contour were in good agreement with values found by previous authors (Beltaos and Rajaratnam 1973; König and Fiedler 1991; Yoda and Fiedler (1996)). As can be seen in Figure 5.2 the jet penetration x_p was defined by the maximum penetration of the jet at the physical centerline of the jet nozzle, therefore, the axial direction x was chosen to coincide with the centerline of the jet nozzle. The maximum lateral penetration of the jet (y_p) was given by the average of the largest penetration perpendicular to the centerline in both sides of the jet, which was selected to be parallel to the direction of the y axis direction. The origin of the coordinate system was located at the exit of the jet nozzle and at the center of the nozzle cross section. The inlet yaw angles (θ) was defined as the angle formed between the centerline of the jet and the direction of the counterflow stream. As was mentioned previously, five different jet to counterflow velocity ratios were tested for the two jets, D_1 and D_2. For every jet to counterflow velocity ratio the data of the concentration field was measured at three different inlet yaw angles, that is, 0^o, 4^o, and 8^o. Table 5.2 presents the values of the geometrical parameters shown in Figure 5.2 for every flow condition.

Table 5.2 shows the ratio of the mean geometrical length in the counterflowing jet, that is, λ and β. These ratios have been used as length scales of the axial concentration decay of a counterflowing jet with inlet yaw angles equal to zero. Therefore, these ratios, as well as x_p, y_p, and x_b, are used to measure the effect of the small inlet yaw angles in the counterflowing jet. These effects will be characterized in the axial and radial spreading of the jet.

Table 5.2: Experimental data of the geometrical parameters of a counterflowing jet at different flow conditions.

θ (deg)	D (mm)	U_r	x_p/D	x_b/D	y_p/D	λ (y_p/x_b)	β (y_p/x_p)
0	8.81	4	16.50	9.5	4.21	0.443	0.255
		8	25.00	17.0	6.50	0.382	0.260
		11	31.67	22.0	7.09	0.322	0.224
		12	34.75	24.5	7.56	0.309	0.218
		14	42.00*	29.50	9.44	0.320	0.225
0	5.64	8	20.25	13.4	5.50	0.411	0.272
		11	27.25	18.0	5.94	0.330	0.218
		14	31.50	24.0	7.50	0.313	0.238
		16	43.75	33.0	8.37	0.254	0.191
		19	51.50	36.5	6.87	0.188	0.133
4	8.81	4	13.50	8.6	3.75	0.435	0.283
		8	20.25	14.0	4.63	0.330	0.228
		11	28.25	23.3	5.75	0.247	0.204
		12	32.00	21.5	5.38	0.250	0.168
		14	33.50	26.0	5.25	0.202	0.157
4	5.64	8	24.00	17.0	5.75	0.338	0.240
		11	25.75	18.6	6.25	0.336	0.243
		14	34.75	24.5	6.75	0.276	0.194
		16	36.50	27.8	6.75	0.185	0.243
		19	45.00	35.0	7.75	0.221	0.172
8	8.81	4	12.50	7.8	4.13	0.532	0.330
		8	21.75	13.0	6.25	0.481	0.287
		11	27.50	19.0	6.75	0.355	0.245
		12	28.25	19.8	5.38	0.272	0.190
		14	30.25	19.8	5.88	0.297	0.194
8	5.64	8	20.75	13.1	6.13	0.467	0.295
		11	23.75	15.8	5.38	0.341	0.226
		14	32.25	23.3	6.50	0.280	0.202
		16	36.50	26.0	6.38	0.245	0.168
		19	36.50	24.0	6.13	0.255	0.168

* This value of x_p was estimated by assuming that x_b was approximately 70 % of the jet penetration. This was the average experimental value found through the analysis of the data for the other flow conditions. The maximum penetration of the jet for this flow condition was out of the field of view of the camera.

5.3.1 Centerline penetration and concentration decay for small yaw angles

As was shown previously (Chapter 3), the centerline penetration depth of a counterflowing jet with inlet yaw angles (θ) equal to zero is proportional to U_r (jet to counterflow velocity ratio), for $4 \leq U_r \leq 19$. For the U_r studied in this investigation this relation between U_r and x_p was found to be linear. Figure 5.3 depicts the maximum centerline penetration (x_p) plotted as a function of U_r. The solid symbols in this figure correspond to the data of the counterflowing jet of diameter D_1 and D_2 with a $\theta = 0^o$. As can be observed, the solid symbols follow the linear relationship found by Yoda and Fiedler (1996). For the case of θ equal to 4^o and 8^o, the data of the centerline penetration length follows the line function just for $U_r \leq 8$. From Figure 5.3 it is clear that the centerline penetration of the counterflowing jet decreases for θ different than zero. As can be observed from Figure 5.3 the data of the centerline penetration depth of the counterflowing jet with θ equal to 4^o and 8^o, has to be represented by a different function than in the case of $\theta = 0^o$. Figure 5.3 depicts the function obtained from a linear regression performed on the data of the penetration length of the counterflowing jet with non-zero θ. It was found that these data follow a function of the form

$$\frac{x_p}{D} = 4.5 \; {U_r}^{3/4} \tag{5.1}$$

from Figure 5.3 it is evident the effect of the inlet yaw angles on the penetration length of the jet. The effects of the inlet yaw angles on the decay of the centerline concentration can be observed on Figure 5.4. This figure depicts the centerline concentration decay of the counterflowing jet with nozzle diameter D_1 for different inlet yaw angles. This figure shows the effect of the inlet yaw angles at different jet to counterflow velocity ratios: $Ur = 4$ (a), $Ur = 8$ (b), $Ur = 12$ (c) and $Ur = 14$ (d). The differences between the centerline decay of the counterflowing jet are not as significant when the axial location is normalized by the maximum axial penetration of the jet. Figure 5.5 depicts the axial concentration decay of the counterflowing

jets at four different jet to counterflow velocity ratios. It is clear that the effects of the small inlet yaw angles in the counterflowing are slight when the axial location is normalized by the centerline penetration length. The data of the profiles at $U_r = 11$ were not included in Figure 5.5, since very similar information can be drawn from the data obtained at $U_r = 12$. Any differences between the profiles shown in Figure 5.5 occur after $0.70x_p$, which has been suggested to be approximately the limit between the established flow region and the mixing zone (Lam and Chan, 2002). Therefore, it is possible to state that the effects of the inlet yaw angles are subtle in the established flow region when x_p is used as the normalizing length scale in the axial location.

It has been shown that the centerline concentration decay of the counterflowing jet with $\theta = 0^{\text{o}}$ collapses into a single curve if the axial location is normalized by the length $x_{_{1/e}}$ (see Chapter 3). The length $x_{_{1/e}}$ is defined as the axial position where the axial concentration takes the value of $e^{-1}C_j$, where C_j is the concentration at the exit of the jet (37 % of the peak inlet value). Figure 5.6 shows the dimensionless centerline concentration decay of the counterflowing jet for two different inlet yaw angles and diameters D_1 and D_2. It can be seen that the centerline concentration profile has a similar behavior when the axial location is normalized by $x_{_{1/e}}$. The solid line shown in Figure 5.6 represents the function found for a counterflowing jet with inlet yaw angles equal to zero, which represents a decay proportional to x^{-1}; details of this can be found in Chapter 3. It was observed that the similar form of the centerline concentration profile was independent of θ for the values tested in this investigation. This universal form is valid just for axial locations within the establish flow region, since the data of the centerline concentration are observed to diverge from the universal form once the mixing zone has been reached. It is also important to point out that there is a slightly steeper decay of the concentration for centerline locations greater than $x/x_{_{1/e}} = 1.75$. Nonetheless, it is possible to state that the results shown in Figure 5.6 are comparable with those obtained from the counterflowing jet with inlet yaw angles equal to zero. Despite the fact that the data of the centerline decay of the counterflowing jet can be represented by a function proportional to x^{-1}, a better

approximation of the centerline decay is found if the function is considered to be proportional to $x^{-6/5}$, as is shown by the broken line in Figure 5.6.

Table 5.2 contains the values of the length ratio λ and β. It has been shown that those ratios can be used to generate universal forms of the centerline concentration decay of the counterflowing jet (see Chapter 3). Figure 5.7 depicts the dimensionless form of the centerline concentration decay for the counterflowing jet with θ values of 4 and 8°. The centerline distance is normalized by the centerline location $x_{_\lambda}$, which is defined as the location where the centerline concentration reaches the value of λ times the concentration at the exit of the jet nozzle. The data of the centerline concentration are normalized by the concentration at the jet and then scaled with λ. As can be seen from Figure 5.7 the data of the centerline concentration shows a universal form for the concentration decay, with all the data collapsed into a single curve. The solid line shown in this figure corresponds to the function found for a counterflowing jet of $\theta = 0°$. This shows that even for non-zero inlet yaw angles , the centerline concentration could be considered proportional to x^{-1}.

Again, the centerline concentration decay can be considered to be represented by a decay proportional to x^{-1}, a better approximation is observed if the decay of the centerline concentration is considered to be proportional to $x^{-6/5}$. This is shown as a broken line in Figure 5.7. A very similar result was found when β and $x_{_\beta}$ were used as the scale for the normalized centerline concentration decay (C_y/C_j) and the axial location respectively.

Figure 5.8 depicts the centerline concentration of the counterflowing jet in a dimensionless form, and shows for both nozzle diameters how the centerline concentration decay is unaffected by the value of θ. The solid line in Figure 5.8 describes a power law function equal to x^{-1}, and a power law of the form $x^{-6/5}$ is shown as a broken line. The length ratios λ and β, and the axial locations $x_{_\lambda}$ and $x_{_\beta}$, can be used to generate

a similar form of the centerline concentration decay of the counterflowing jet with small yaw angles. However, this similarity form is valid in the established flow region of the counterflowing jet, that is, up to 60 to 70 % of the total penetration length.

For a counterflowing jet with inlet yaw angles equal to zero, the relationship between the ratios λ and β, and the axial locations x_{λ} and x_{β} with the velocity ratio U_r, was found to be linear for $U_r > 4$, as well as was the case of $x_{1/e}$. For the case of inlet yaw angles different than zero (θ equal to 4 and 8 degrees) the data show a significant scatter around the linear function found for the case of $\theta = 0^{o}$. Figure 5.9 shows the variation of λ and β as a function of U_r. As was mentioned previously, the data for $\theta = 4^{o}$ and $\theta = 8^{o}$ do not follow the linear function as well as the case of $\theta = 0$. The equations of these two functions are given by $0.55 - 0.02\ U_r$ and $0.35 - 0.01\ U_r$ for the case of λ and β respectively. It is important to mention that these equations were found for $U_r > 4$, since the similar curve of the centerline concentration decay was found just for $U_r > 4$ when $\theta = 0^{o}$ (Chapter 3). The value of the axial distances $x_{1/e}$, x_{λ}, and x_{β} were found to have a linear dependance on U_r for the case of $\theta = 0^{o}$ (Chapter 3). However, the same behavior was not observed for the case of inlet yaw angles different than zero.

Figure 5.10 illustrate the relation between the axial distances $x_{1/e}$, x_{λ}, and x_{β} with U_r. Figure 5.10a shows the values of $x_{1/e}$ at different velocity ratios, nozzle diameter, and inlet yaw angles . From this figure it is clear that the values of $x_{1/e}$ for $\theta = 4^{o}$ and $\theta = 8^{o}$ are typically smaller than in the case of $\theta = 0^{o}$. This would suggest that the dilution of the counterflowing jet at the tested inlet yaw angles are slightly greater than when observed at $\theta = 0^{o}$. A similar behavior can be observed for the case of x_{λ} and x_{β}, however a slightly more even distribution around the linear function was noticed in Figures 5.10b and 5.10c. In Chapter 3, similar functions obtained from the centerline concentration decay were used to generate empirical equations to predict the concentration decay of the counterflowing jet. These equations were found to agree relatively well with the centerline concentration decay in the established flow

region. The scatter of the data in Figures 5.9 and 5.10 could result in a larger error when the empirical equations (Equations 3.6, 3.7, and 3.8) are used to predict the centerline concentration decay for counterflowing jets with inlet yaw angles different than zero.

5.3.2 Spreading of the counterflowing jet at small yaw angles

Figure 5.11 depicts the contour of the mean concentration field of the counterflowing jet for three different inlet yaw angles at $U_r = 4$. It is important to point out that the coordinates system was conveniently chosen, so the origin coincides with the center of the cylindrical jet nozzle. Therefore, the centerline of the jet concurs with the x axis of the coordinate system. Figure 5.11 shows that the effect of a yaw angle $\theta = 4^o$ is not as significant as in the case of $\theta = 8^o$. For the case of $\theta = 8^o$ the jet is deflected towards the counterflow stream. Figure 5.11b depicts an approximately similar shape of the 5 % contour with respect to the centerline of the jet. On the other hand, Figure 5.11c shows the deflection of the jet for $\theta = 8^o$ in the direction of the counterflow stream. The effects of the inlet yaw angles in the shape of the average concentration field seems to decrease for larger values of U_r. Figure 5.12 depicts the mean concentration contour of the counterflowing jet at $U_r = 11$. Although the deflection of the jet for the case of $\theta = 8^o$ for $U_r = 11$ (Figure 5.12c) is not as evident as the case of $U_r = 4$, it is noticeable that the jet has been bent by the counterflow stream. Contrary to this, for the case of $\theta = 4^o$ at $U_r = 11$ the shape of the concentration contour is not affected by the variation of the inlet yaw angles (see Figure 5.12b). A very similar result is evident for the case of $U_r = 19$ which is shown in Figure 5.13. This figure shows data obtained for the jet with a cylindrical nozzle equal to 5.64 mm, which depicts that the effects of the inlet yaw angles in the spreading of the jet are similar for the two jet diameters.

Figure 5.14 shows the normalized radial concentration profiles at different axial locations of the counterflowing jet with $\theta = 4^o$ and nozzle diameter D_1. The concentration

field was normalized by the concentration at the exit of the jet. In this figure four different jet to counterflowing velocity ratios are shown, $Ur = 4$ (a), $Ur = 8$ (b), $Ur = 11$ (c) and $Ur = 14$ (d). It is important to mention that the data of the profiles at $U_r = 12$ were not included since they were very similar to the one obtained for $Ur = 11$. The axial location of the profiles shown in Figure 5.14 were chosen to be in the established flow region (upstream of 0.70 x_p). Additionally, the profiles were obtained at axial distances $x/D \geq 6$, where the effects of the counterflowing jet can be considered subtle. Figure 5.14 shows that the effects of the inlet yaw angles vanish for higher values of U_r, this can be appreciated by observing the symmetry of the radial profiles at the higher values of U_r. For the case of $U_r = 14$ the radial profiles of the mean concentration are approximately symmetric with respect to the centerline of the jet. A similar result is observed in Figure 5.15, which depicts the normalized radial profiles of the mean concentration field for the counterflowing jet with $\theta = 4^o$ and nozzle diameter D_2. As can be seen for higher values of U_r, the effect of the inlet yaw angles is less significant and noticeable. It would appear that for high values of U_r the jet flow becomes stronger and less affected by the counterflow stream.

For the case of $\theta = 8^o$ the effects of the inlet yaw angles were found at every jet to counterflow velocity ratio tested. Figure 5.16 shows the normalized radial profiles of the mean concentration field for the counterflowing jet with $\theta = 8^o$ and nozzle diameter D_1. As was mentioned previously, the symmetry of the radial profiles are affected by the inlet yaw angle; clearly the centerline of the jet is bent towards the direction of the counterflowing current and away from the broken line shown in the graphs of Figure 5.16, which delineates the geometrical centerline of the cylindrical nozzle. Thus, it is possible to notice that the maximum radial concentration is deflected off the physical centerline of the jet nozzle. This deflection is more evident at axial distances further from the jet nozzle. For the nozzle diameter D_2, the radial profiles of the mean concentration field showed very similar results as the observations for D_1. Figure 5.17 gives the normalized radial profiles of the concentration field for the counterflowing jet with $\theta = 8^o$ and nozzle diameter D_2. Once again, the effect

of the inlet yaw angles are found for every jet to counterflow velocity ratio, even for the highest U_r tested ($U_r = 19$). One can infer that for $U_r = 19$, the jet flow is not strong enough to remove the effect of the larger inlet yaw angles that $\theta = 8^o$ represents.

Compared to the spreading of a jet with $\theta = 0^o$ (Chapter 4). It was found that for the case of inlet yaw angles different than zero, the spreading of the jet showed a similarity function in the inner region for an axial location upstream of the 70 % of the total jet penetration, this agrees with the results shown by Lam and Chan (2002). Nonetheless, the similarity function obtained for the radial spreading of the counterflowing jet was found just for the radial position within the jet width. This proved that, as suggested by Yoda and Fiedler (1996), there is an inner region where the jet flow is the dominant region, for which the flow presents a self-similarity behavior resembling a free jet. Figure 5.18 depicts the dimensionless form of the radial concentration profiles at different locations along the centerline of the counterflowing jet for different jet to counterflow velocity ratios. The profiles shown in this figure are for the counterflowing jet at $\theta = 4^o$. The mean concentration along the radial direction (C_y) is normalized by the concentration at the centerline of the jet in the corresponding axial location (C_c). The location of the concentration in the radial position (y) was normalized by the location at which the local mean concentration was equal to half the concentration at the centerline of the jet, this is $C_y = 0.5C_c$ this distance was noted by $y_{_{1/2}}$. As can be seen from Figure 5.18 the dimensionless form of the radial concentration shows a similar function for radial locations $|y/y_{_{1/2}}| \leq 1$, which was also observed for the case of the counterflowing jet with no inlet yaw angles (Chapter 4). A similar result was observed for the case of the counterflowing jet with inlet yaw angles equal to 8^o. Figure 5.19 depicts the dimensionless form of the radial concentration profiles of the jet with $\theta = 8^o$ at four different jet to counterflowing velocity ratios. Even though the dimensionless profiles collapsed into a single curve for the inner region of the radial profiles, the symmetry of the profiles are affected by the inlet yaw angles at radial locations out of the inner region of the jet where the counterflow stream is the dominant flow. The solid line shown in

Figures 5.18 and 5.19, represents the Gaussian distribution found for the case of inlet yaw angles equal to zero (Equation 4.1, Chapter 4). As can be seen the data in the inner zone of the counterflowing jet is well described by the Gaussian distribution. Therefore it is possible to suggest that the value of the inlet yaw angles tested in this investigation has no effect in the similar form of the radial concentration profiles.

As was previously reported in Chapter 4 the shape of the dimensionless radial concentration profiles was affected by the instabilities of the mixing zone. Although the established flow region is defined as the axial location upstream of $0.70x_p$, the effect of the mixing zone on the radial similarity region of the jet was observed for axial distances between 50 to 60 % of the total jet penetration (Chapter 4). For the case of the counterflowing jet at $\theta = 4^{\circ}$ the effects of the mixing zone in the similarity region were found to be negligible at axial distances close to 0.50 x_p. For the counterflowing jet with inlet yaw angles equal to 8°, the effects of the mixing zone were observed at axial distances *less* than $0.50x_p$. This can be observed in Figure 5.19. The jet is significantly bent by the counterflow stream for the large value of inlet yaw angles ($\theta = 8^{\circ}$).

The radial location $y_{_{1/2}}$ is commonly defined as the jet width and the growth of the $y_{_{1/2}}$ is often used to define the spreading of the jet (Fischer et al., 1979). Figure 5.20 depicts the growth of the jet width both diameters and different inlet yaw angles values ($\theta = 4^{\circ}$ Figure 5.20a and $\theta = 8^{\circ}$ Figure 5.20a). The axial location x and the jet width $y_{_{1/2}}$ are normalized by the maximum axial penetration of the jet x_p. As was shown in Figures 5.11 and 5.12 the penetration of the jet in the radial direction was not the same in both directions. Relative to the physical axis of the jet, the lateral penetration was found to be smaller on the side more exposed to the counterflow stream. As a result, the radial location of the jet width on the side more exposed to the uniform counterflow was found to be significantly smaller than the other. Therefore, the value of $y_{1/2}$ used corresponds to the averaged value of the jet width in both directions perpendicular to the centerline of the jet. Not surprisingly, Figures 5.12 and 5.13 show that the growth of the jet for non zero inlet yaw angles is more asymmetric

than the case of the counterflowing jet with $\theta = 0^o$. Nonetheless, when x_p is used as the scale factor for the width growth of the jet, the increase of the jet can be approximated by the equation found for the case of $\theta = 0^o$.

Figure 5.20 shows that the growth of the jet width can be described by the equations found for the case of the counterflowing jet of $\theta = 0^o$. For the linear growth region the equations is given by

$$\frac{y_{1/2}}{x_p} = 0.003 + 0.126 \left(\frac{x}{x_p} \right) \tag{5.2}$$

and for the growth of the jet width in the power law growth region

$$\frac{y_{1/2}}{x_p} = 0.027 + 0.32 \left(\frac{x}{x_p} \right)^{2.5} \tag{5.3}$$

For the two values of inlet yaw angles the jet width growth can be divided into two regions, the linear growth region, and the power law growth region. The linear growth region was found to extend up to approximately 30 % of the total penetration, and the power law growth region can be found at axial distances $0.30x_p < x < 0.60x_p$. This suggests that the maximum axial penetration of the counterflowing jet can be considered a scale factor for the increase of the jet width, including counterflowing jets with small inclinations.

5.4 Conclusion

In this chapter, the effects of small yaw angles values have been experimentally investigated. The study was focused on the effects of two different values of inlet yaw angles ($\theta = 4^o$ and $\theta = 8^o$). The centerline concentration decay and the spreading of the jet in the radial direction were studied to determine these effects. The investigation was focused in the dilution of the centerline concentration, maximum axial penetration and the self similar region of the radial spreading of the jet. The following conclusions were drawn from this investigation:

1. The axial penetration of the counterflowing jet was proved to be affected by the value of the yaw angle θ. The higher the value of θ the shorter the axial penetration of the counterflowing jet. Nonetheless, for low values of jet-to-counterflow velocity ratios ($U_r \leq 8$) the penetration length of the jet was found to display behavior similar to that of the counterflowing jet with $\theta = 0^o$. For $U_r \geq 8$ the relationship between x_p/D and U_r was found to follow a power law function of exponent equal to 3/4.

2. Although the penetration length of the jet was affected by the value of the inlet yaw angle, the centerline concentration decay was found to present similar characteristics as the observations for a counterflowing jet of $\theta = 0^o$, when the axial location is normalized by x_p.

3. The centerline concentration decay of the jet with small inclination can be represented by universal forms obtained for a counterflowing jet of inlet yaw angles equal to zero, as shown in Figures 5.6, 5.7 and 5.8.

4. The radial (cross-stream) concentration profiles of the jet in established flow region along the radial direction was found to be slightly affected by the small inlet yaw angle. At low values of U_r the symmetry of radial concentration profiles was significantly more affected by the two inlet yaw angles studied in this investigation. However, the effects of the inlet yaw angles seem to vanish for higher values of U_r. For the case of $\theta = 4^o$, the effects of the inlet yaw angles seem to be less significant for $U_r > 11$. For $\theta = 8^o$ the symmetry of the radial concentration profiles is noticeably affected by the inlet yaw angles even at $U_r = 19$. Even though the symmetry of the the radial concentration profiles is affected, the similarity form of the radial concentration profiles in the inner region was found to be approximately equal to the those observed in a counterflowing jet with inlet yaw angles equal to zero.

5. The scalar growth of the counterflowing jets studied in this investigation for the the different value of inlet yaw angles were found to be approximately the same

as the one observed for $\theta = 0^o$ when both the axial location and jet width are scaled with the penetration length. The two regions of the jet width growth were also observed for jets set at small inlet yaw angles to the counterflow. The linear growth region of the jet width with small inlet yaw angle was found to extend up to 30 % of the total jet penetration. The increase of the width in the linear growth region can be represented by the empirical equations obtained for $\theta = 0^o$ (Figure 5.20). The power law growth region was found be significantly more affected by θ, the data of the jet width were found to be sligthly off the empirical equation that describes the scalar growth of the jet with $\theta = 0^o$.

References

Beltaos, S. and Rajaratnam, N. (1973). Circular turbulent jet in an opposing infinite stream. *First Canadian Hydraulics Conference, Edmonton*.

Bernero, S. and Fiedler, H. E. (2000). Application of particle image velocimetry and proper orthogonal decomposition to the study of a jet in a counterflow. *Experiments in Fluids*, pages S274 – S281.

Chan, H. C. (1999). *Investigation of a round jet into a counterflow*. PhD thesis, Dept. of Civil Engineering, University of Hong Kong.

Fischer, H. B., List, E. J., Imberger, J., and Brooks, N. H. (1979). *Mixing in inland and coastal waters*. Academic Press, Inc.

Hilderman, T. L. (2004). *Measurement, modelling, and stochastic simulation of concentration fluctuations in a shear flow*. PhD thesis, University of Alberta.

König, O. and Fiedler, H. E. (1991). The structure of round turbulent jets in counterflow: a flow visualization study. *Advances in turbulence 3*, pages 61 – 66.

Lam, K. M. and Chan, C. H. C. (2002). Time-averaged mixing behavior of circular jet in counterflow: Velocity and concentration measurements. *Journal of Hydraulic Engineering*, 128(9):861 – 865.

Lam, K. M. and Chan, H. C. (1995). Investigation of turbulent jets issuing into a counterflowing stream using digital image processing. *Experiments in Fluids*, 18:210 – 222.

Morgan, W. D. and Brinkworth, B. J. (1976). Upstream penetration of an enclosed counterflowing jet. *Industrial and Engineering Chemistry Fundamentals*, 15(2):125 – 127.

Timma, E. (1962). Turbulent circular and falt streams developing in a counterflow. *Russian periodical, Adakemii Nauk. Estonskoy SSr, Seriya Fiziko - Matamatich-eskikh i Tekhnicheskikh Nauk*, 4:253 – 262.

Yoda, M. and Fiedler, H. E. (1996). The round jet in a uniform counterflow: flow visu-alization and mean concentration measurements. *Experiments in Fluids*, 21(6):427 – 436.

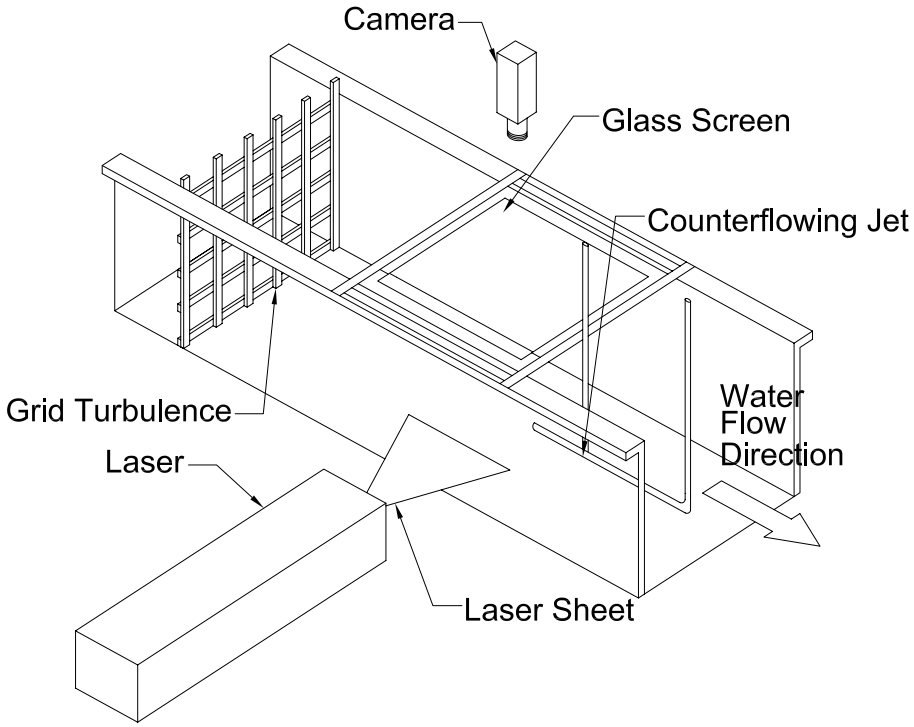

Figure 5.1: Schematic of the experimental setting used to measure the concentration field of the counterflowing jet.

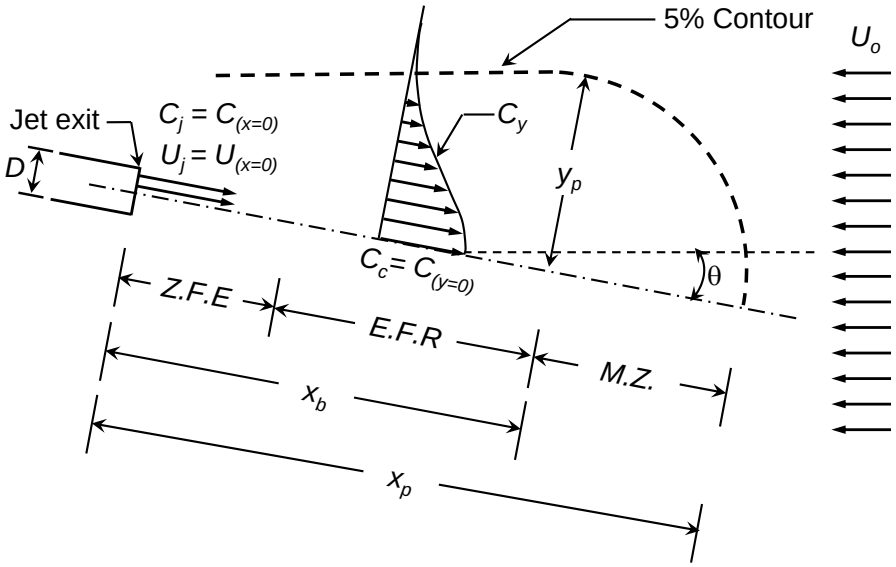

Figure 5.2: Schematic of the mean parameters of the counterflowing jet with a yaw angle θ (based on Beltaos and Rajaratnam (1973), Yoda and Fiedler (1996), and Chan (1999)). Three different regions can be identified: the zone of flow establishment (ZFE), the established flow region (EFR) , and the mixing zone (MZ).

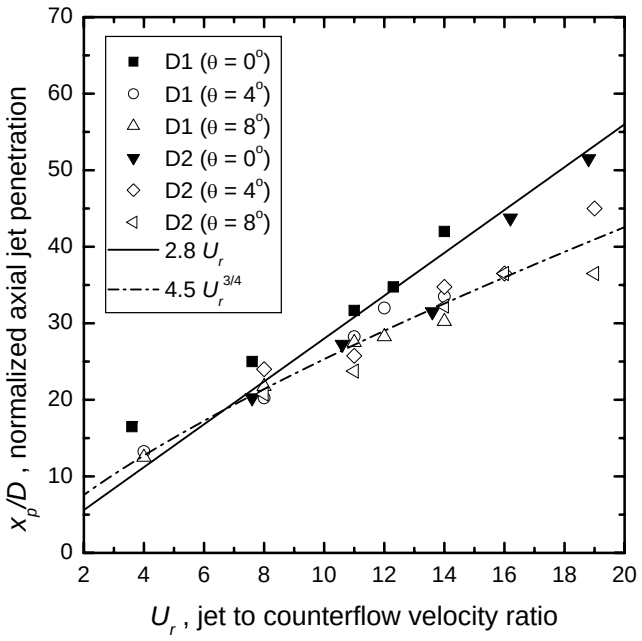

Figure 5.3: Maximum centerline penetration of the counterflowing jet. Solid symbols show the penetration of the counterflowing jet with inlet yaw angle of 0°. Solid line represents the linear relation given by Yoda and Fiedler (1996). The broken line shows the result of a fit done for the data with inlet yaw angle different than zero.

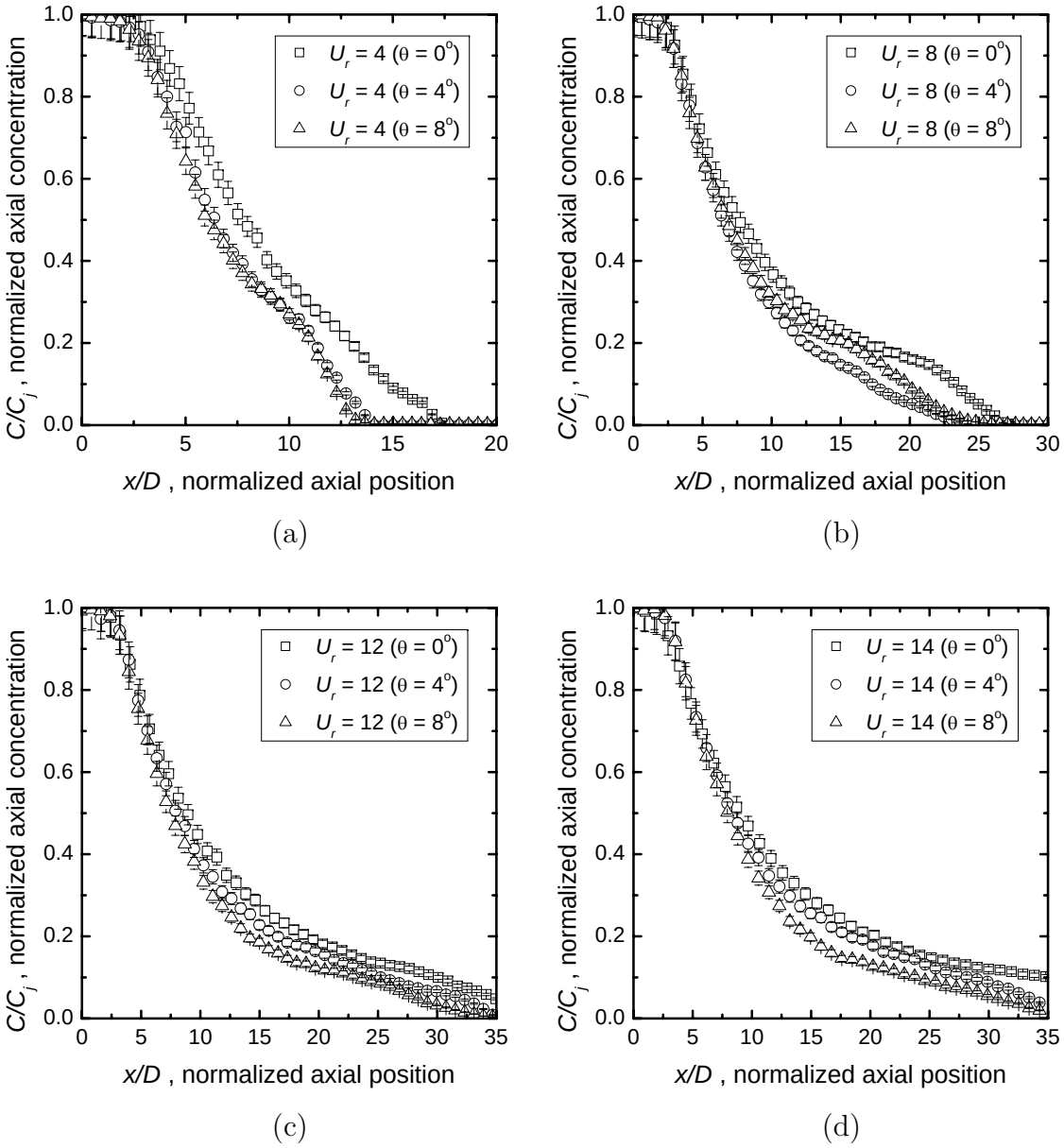

Figure 5.4: Centerline concentration profiles of the counterflowing jet at $Ur = 4$ (a), $Ur = 8$ (b), $Ur = 12$ (c) and $Ur = 14$ (d). The jet diameter of the nozzle used was 8.81 mm. The radial concentration is normalized by the concentration at the exit of the nozzle.

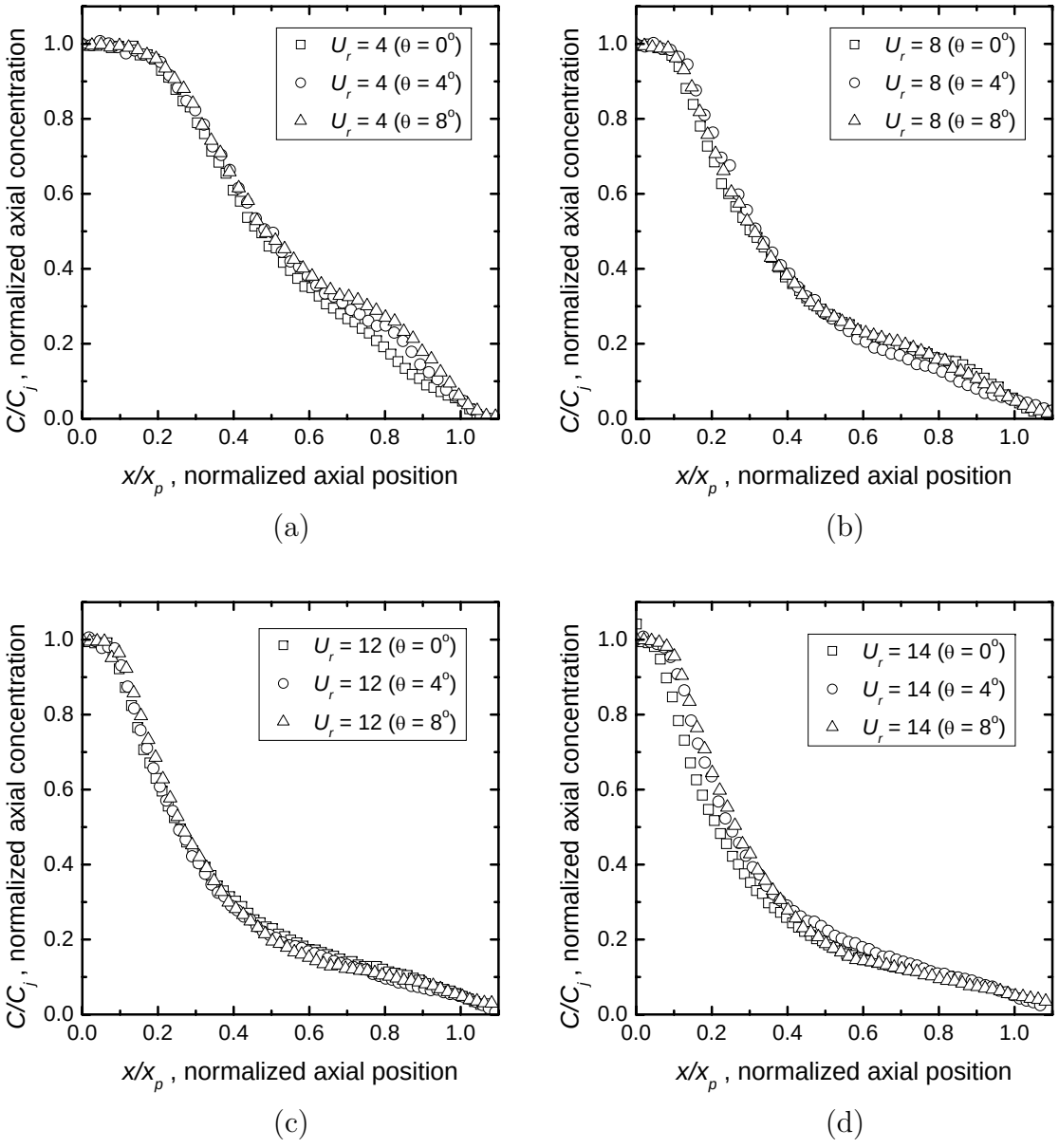

Figure 5.5: Centerline concentration profiles of the counterflowing jet at $Ur = 4$ (a), $Ur = 8$ (b), $Ur = 12$ (c) and $Ur = 14$ (d). The jet diameter of the nozzle used was 8.81 mm. The radial concentration is normalized by the concentration at the exit of the nozzle, and the axial location is normalized by the penetration length of the jet. The error bars of the data are approximately the size of the symbols; an example of this can be seen in Figure 5.4.

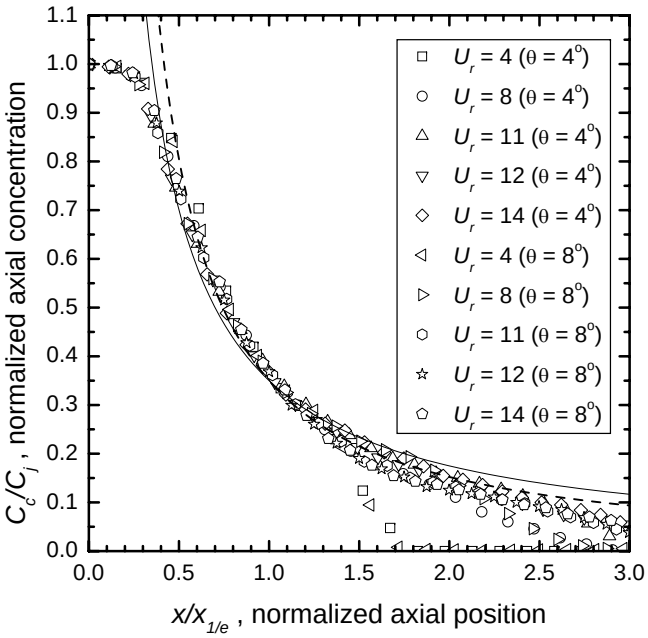

(a)

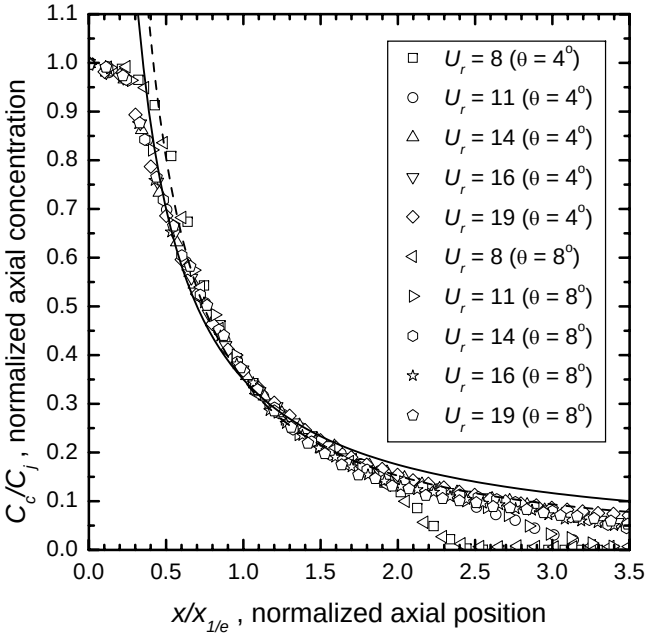

(b)

Figure 5.6: Dimensionless form of the centerline concentration decay of the counter-flowing jet for different values of θ and two different nozzle diameters (a) D = 8.81 mm and (b) D = 5.64 mm. The centerline distance $x_{_{1/e}}$ is defined as the centerline location where $C_y = e^{-1}\, C_j$. The error bars of the data are approximately the size of the symbols; an example of this can be seen in Figure 5.4.

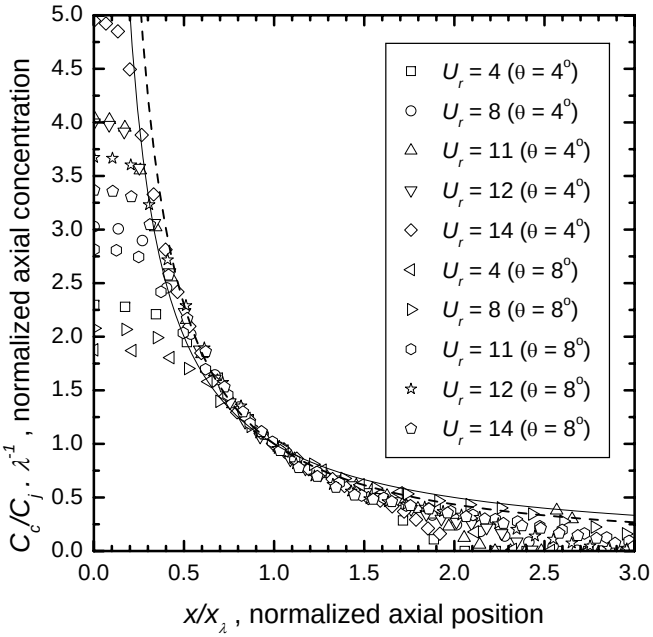

(a)

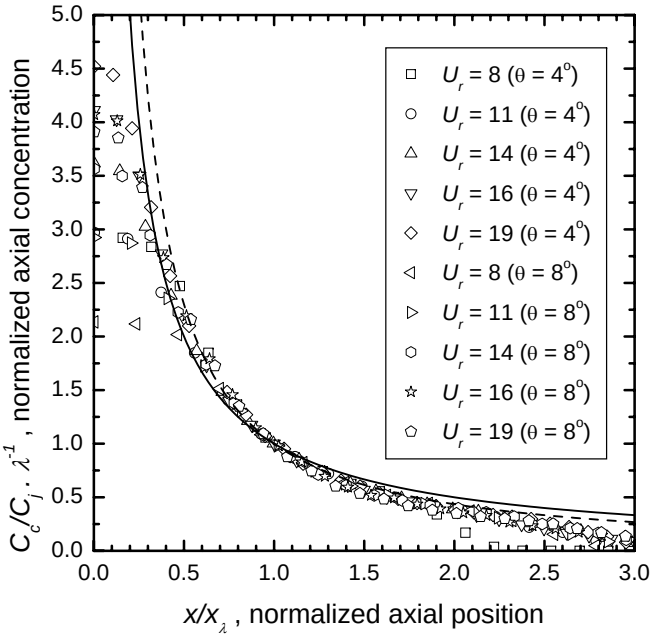

(b)

Figure 5.7: Dimensionless form of the centerline concentration decay of the counterflowing jet for different values of θ and two different nozzle diameters (a) D = 8.81 mm and (b) D = 5.64 mm. The centerline distance x_λ is defined as the centerline location where $C_y = \lambda\, C_j$. The error bars of the data are approximately the size of the symbols; an example of this can be seen in Figure 5.4.

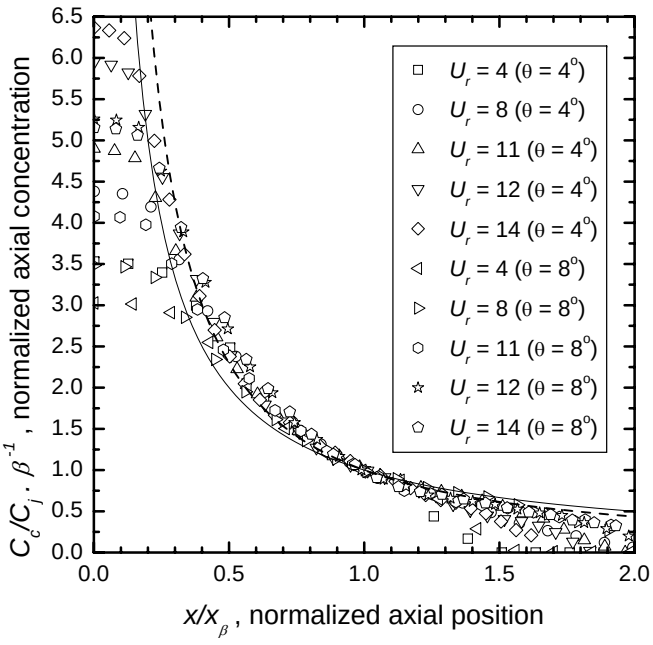

(a)

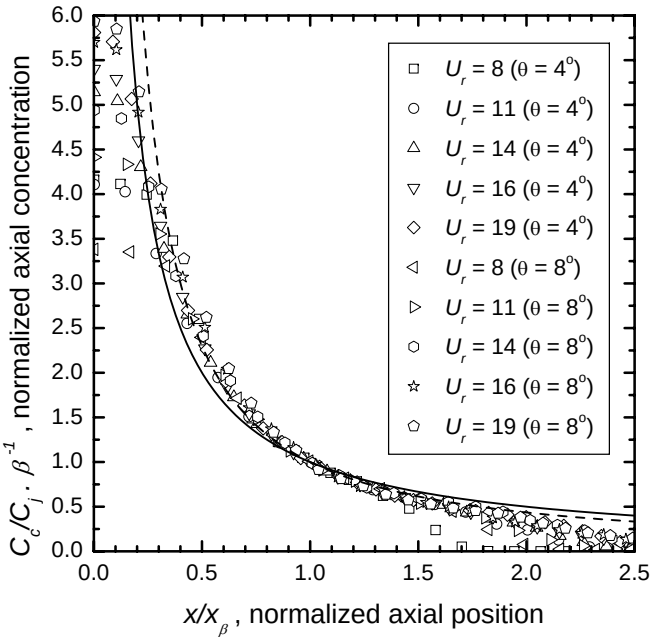

(b)

Figure 5.8: Dimensionless form of the centerline concentration decay of the counterflowing jet for different values of θ and two different nozzle diameters (a) D = 8.81 mm and (b) D = 5.64 mm. The centerline distance x_β is defined as the centerline location where $C_y = \beta\, C_j$. The error bars of the data are approximately the size of the symbols; an example of this can be seen in Figure 5.4.

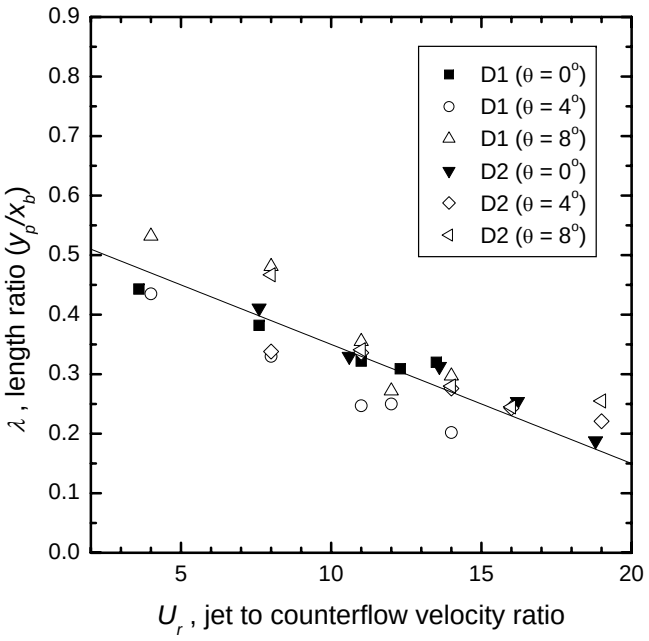

(a)

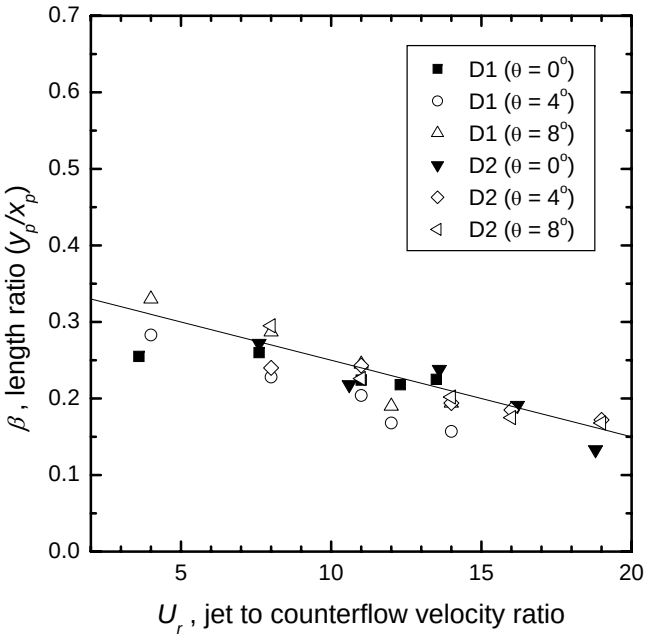

(b)

Figure 5.9: Geometrical parameters λ(a) and β(b) as a function of the jet to couterflowing velocity ratio U_r. The geometrical parameters were measured at different values of inlet yaw angles and U_r. The data indicated as D_1 and D_2 correspond to the data of the nozzle diameter 8.81 and 5.64 mm respectively.

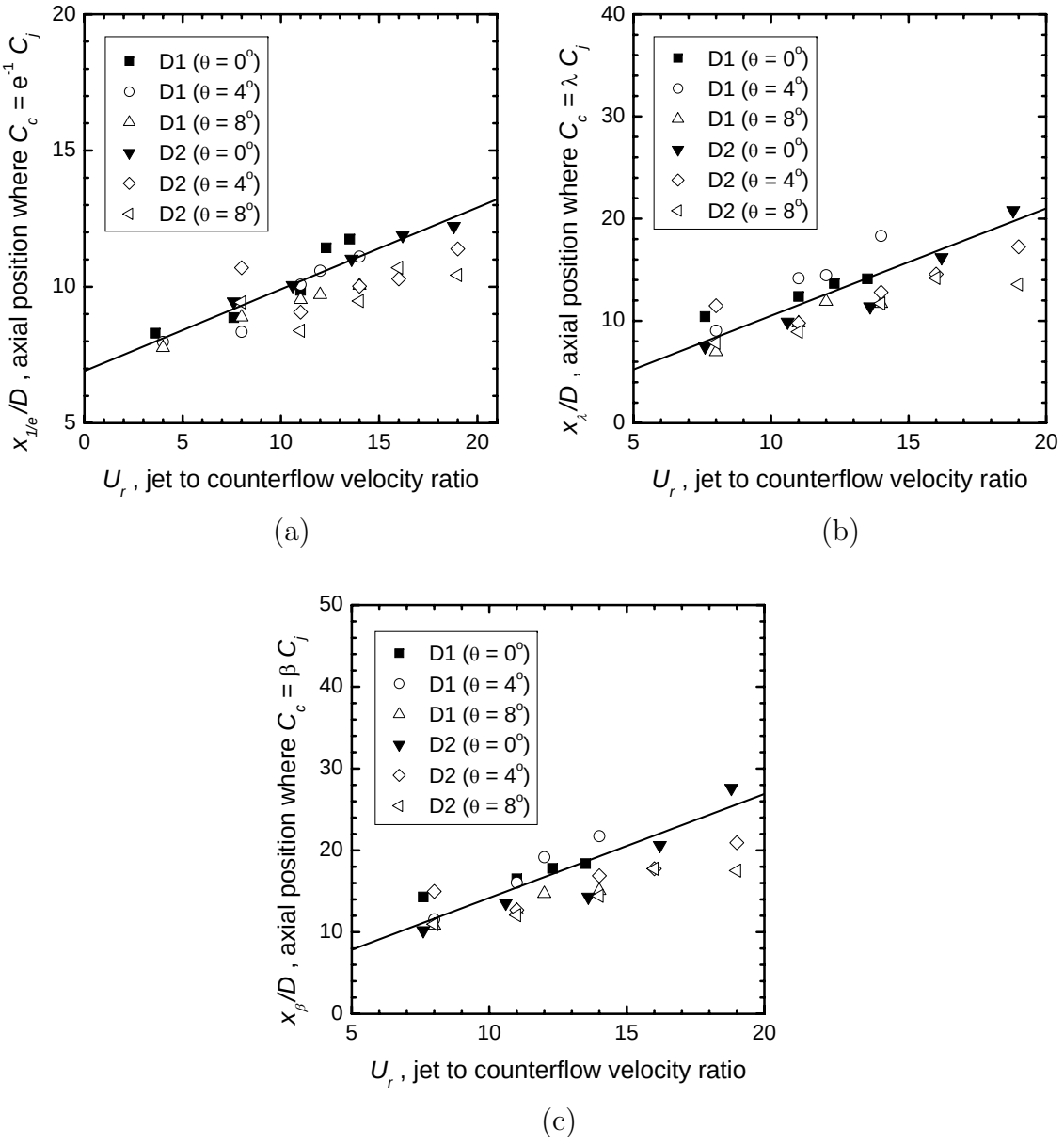

Figure 5.10: Axial distances $x_{1/e}$(a), x_λ(b), and x_β(c) as a function of the jet to counterflowing velocity ratio U_r. The data indicated as D_1 and D_2 correspond to the data of the nozzle diameter 8.81 and 5.64 mm respectively. The solid lines represent the linear function found for the case of $\theta = 0^o$, these functions are given by $6.9 + 0.3\ U_r$(a), $1.05\ U_r$(b), and $1.5 + 1.27\ U_r$(c).

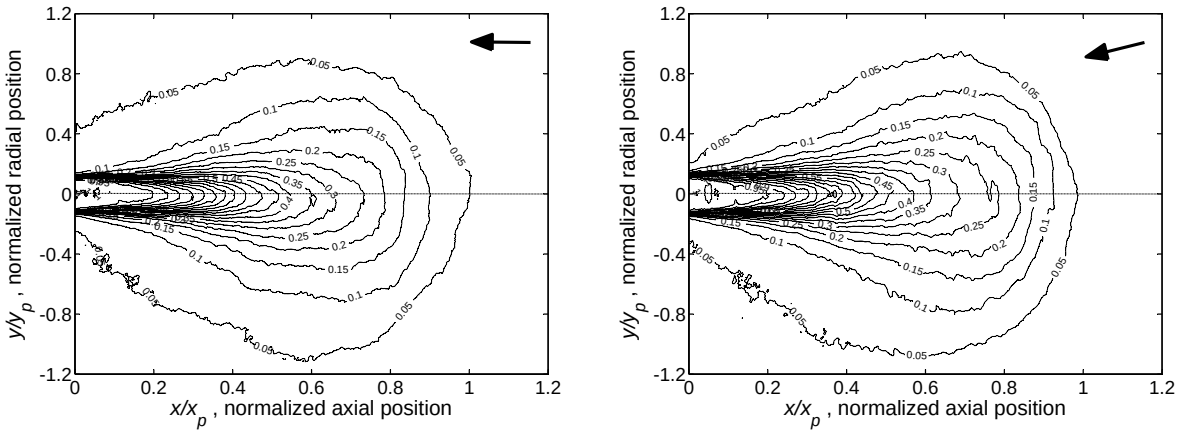

(a) (b)

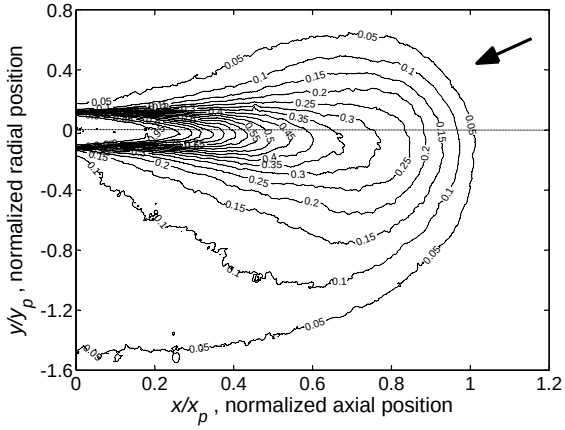

(c)

Figure 5.11: Mean concentration field of the counterflowing jet at $U_r = 4$ for three different values of θ; 0°(a), 4°(b), and 8°(c). Data shown in this graph corresponds to a nozzle with a diameter of 8.81 mm. The coordinates in the axial directions were normalized by the mean axial penetration of the jet (x_p), while the radial location was normalized by the average maximum lateral penetration of the jet (y_p). The arrows are symbolic representation of the approximate direction of the counterflow.

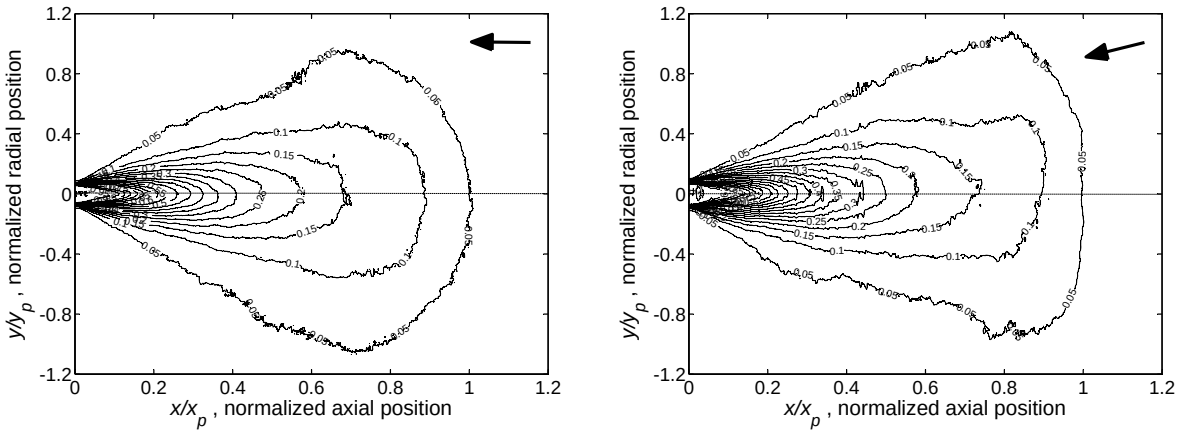

(a) (b)

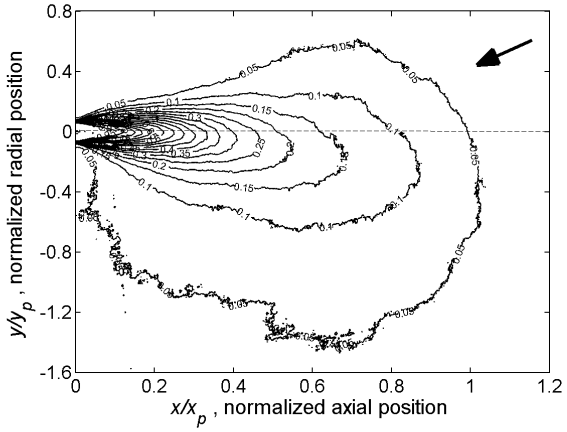

(c)

Figure 5.12: Mean concentration field of the counterflowing jet at $U_r = 11$ for three different values of θ; 0°(a), 4°(b), and 8°(c). Data shown in this graph corresponds to a nozzle with a diameter of 8.81 mm. The coordinates in the axial directions were normalized by the mean axial penetration of the jet (x_p), while the radial location was normalized by the average maximum lateral penetration of the jet (y_p). The arrows are symbolic representation of the approximate direction of the counterflow.

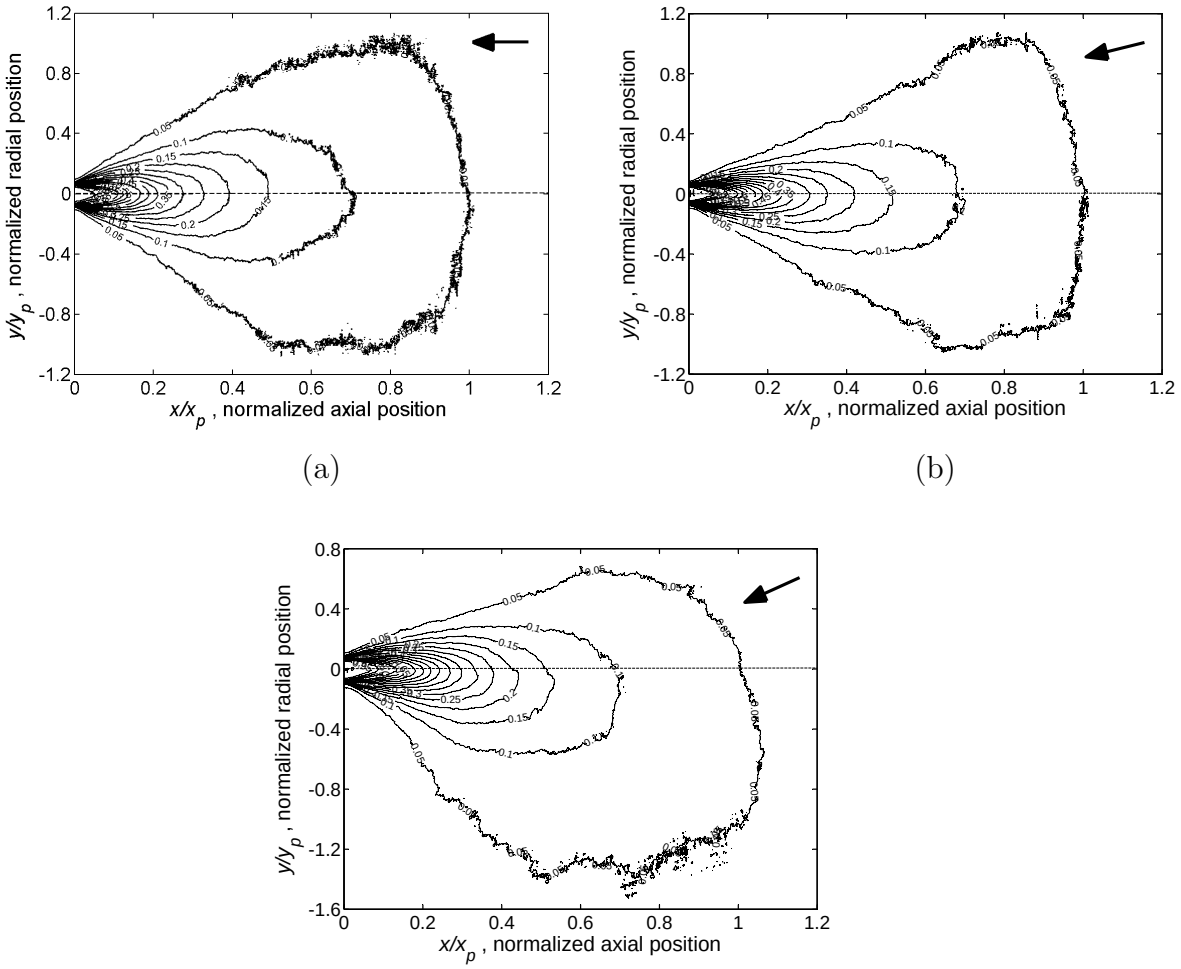

Figure 5.13: Mean concentration field of the counterflowing jet at $U_r = 19$ for three different values of θ; 0°(a), 4°(b), and 8°(c). Data shown in this graph corresponds to a nozzle with a diameter of 5.64 mm. The coordinates in the axial directions were normalized by the mean axial penetration of the jet (x_p), while the radial location was normalized by the average maximum lateral penetration of the jet (y_p). The arrows are symbolic representation of the approximate direction of the counterflow.

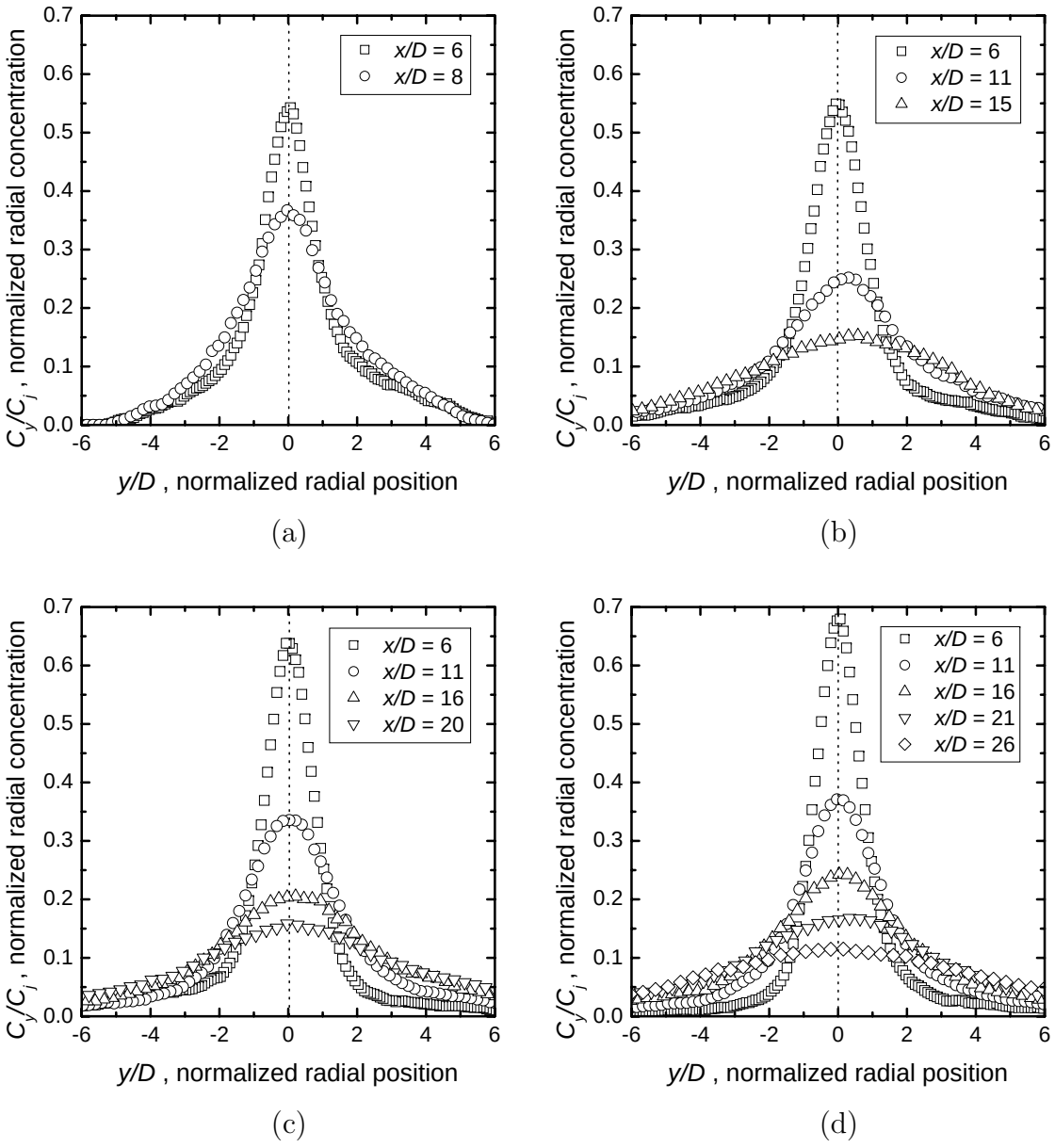

Figure 5.14: Radial concentration profiles of the counterflowing jet with $\theta = 4^o$ at $Ur = 4$ (a), $Ur = 8$ (b), $Ur = 11$ (c) and $Ur = 14$ (d). The jet diameter of the nozzle used was 8.81 mm. The radial concentration is normalized by the concentration at the exit of the nozzle. The profiles are obtained within the established flow region of the counterflowing jet. The error bars of the data are approximately the size of the symbols; an example of this can be seen in Figure 5.4.

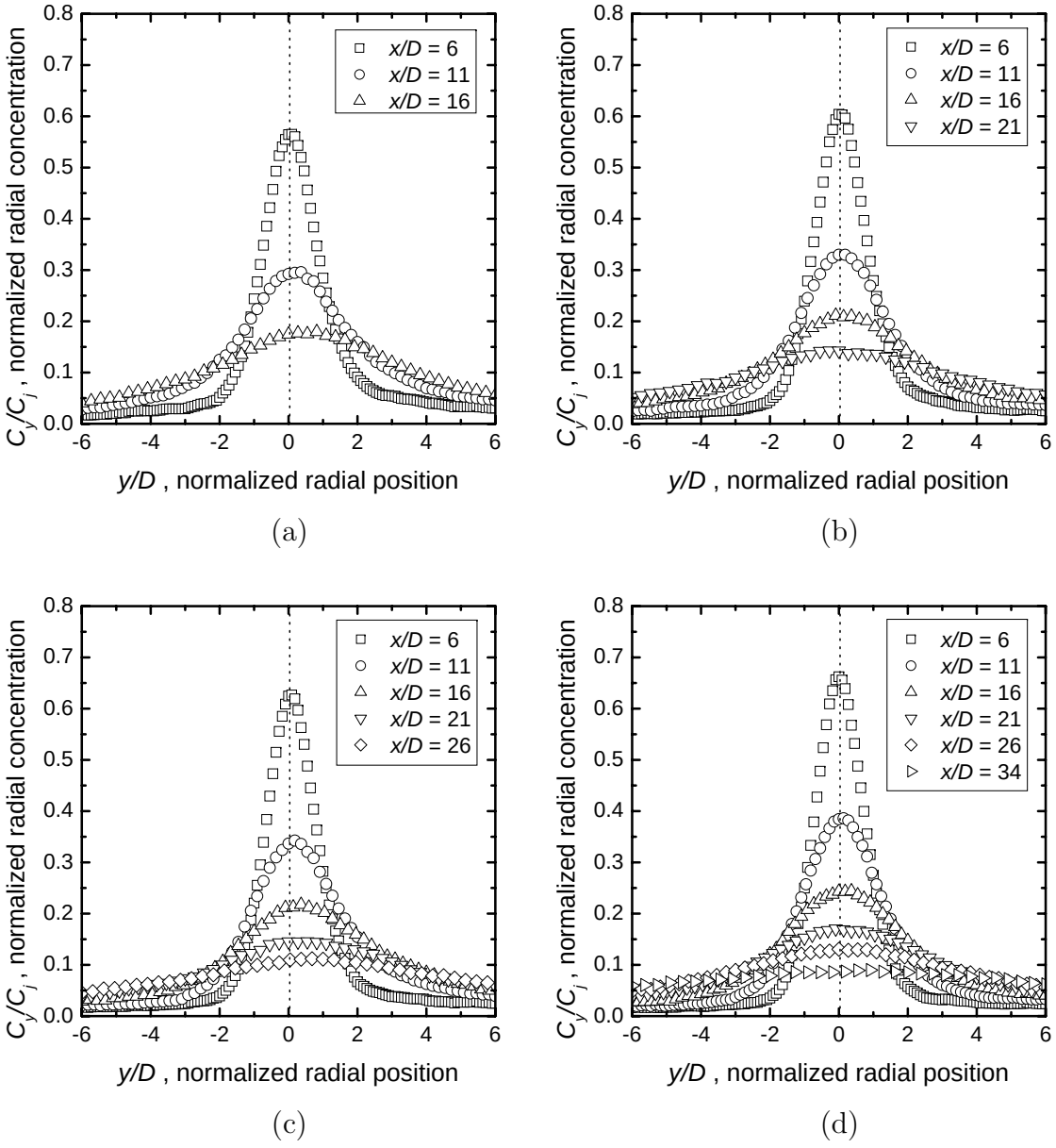

Figure 5.15: Radial concentration profiles of the counterflowing jet with $\theta = 4^{o}$ at $Ur = 11$ (a), $Ur = 14$ (b), $Ur = 16$ (c) and $Ur = 19$ (d). The jet diameter of the nozzle used was 5.64 mm. The radial concentration is normalized by the concentration at the exit of the nozzle. The profiles are obtained within the established flow region of the counterflowing jet. The error bars of the data are approximately the size of the symbols; an example of this can be seen in Figure 5.4.

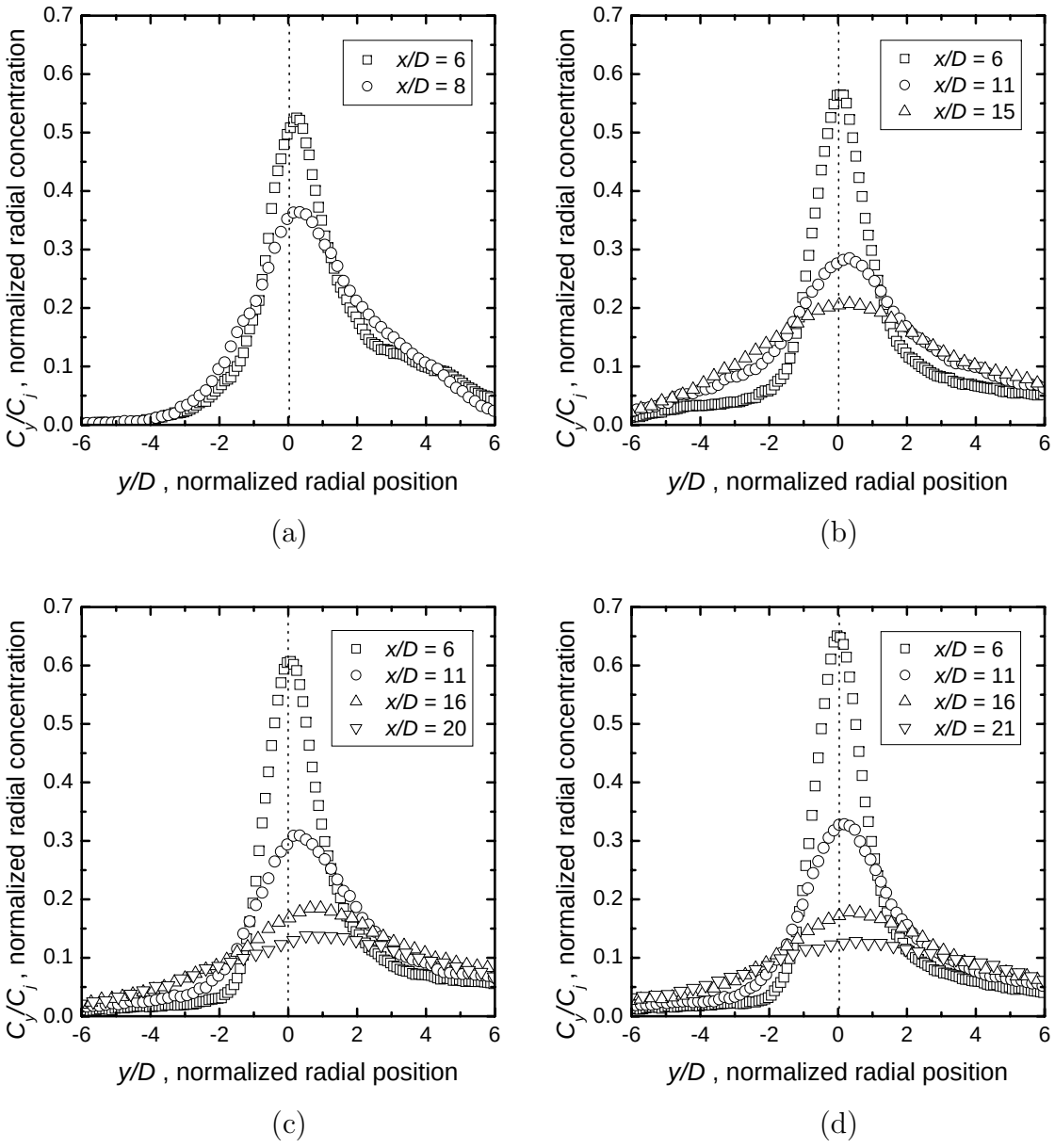

Figure 5.16: Radial concentration profiles of the counterflowing jet with $\theta = 8^{o}$ at $Ur = 4$ (a), $Ur = 8$ (b), $Ur = 11$ (c) and $Ur = 14$ (d). The jet diameter of the nozzle used was 8.81 mm. The radial concentration is normalized by the concentration at the exit of the nozzle. The profiles are obtained within the established flow region of the counterflowing jet. The error bars of the data are approximately the size of the symbols; an example of this can be seen in Figure 5.4.

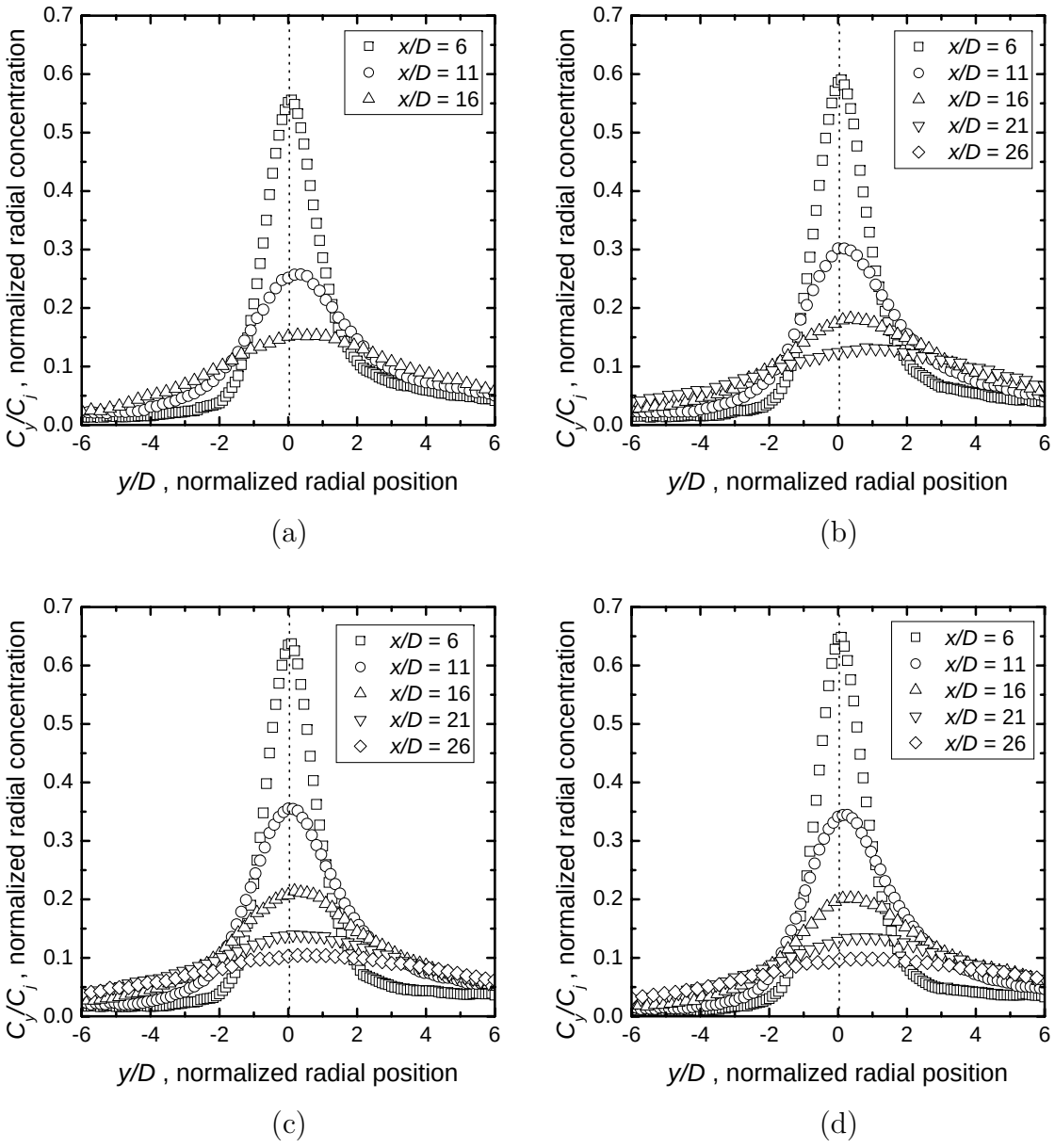

Figure 5.17: Radial concentration profiles of the counterflowing jet with $\theta = 8^{o}$ at $Ur = 11$ (a), $Ur = 14$ (b), $Ur = 16$ (c) and $Ur = 19$ (d). The jet diameter of the nozzle used was 5.64 mm. The radial concentration is normalized by the concentration at the exit of the nozzle. The profiles are obtained within the established flow region of the counterflowing jet. The error bars of the data are approximately the size of the symbols; an example of this can be seen in Figure 5.4.

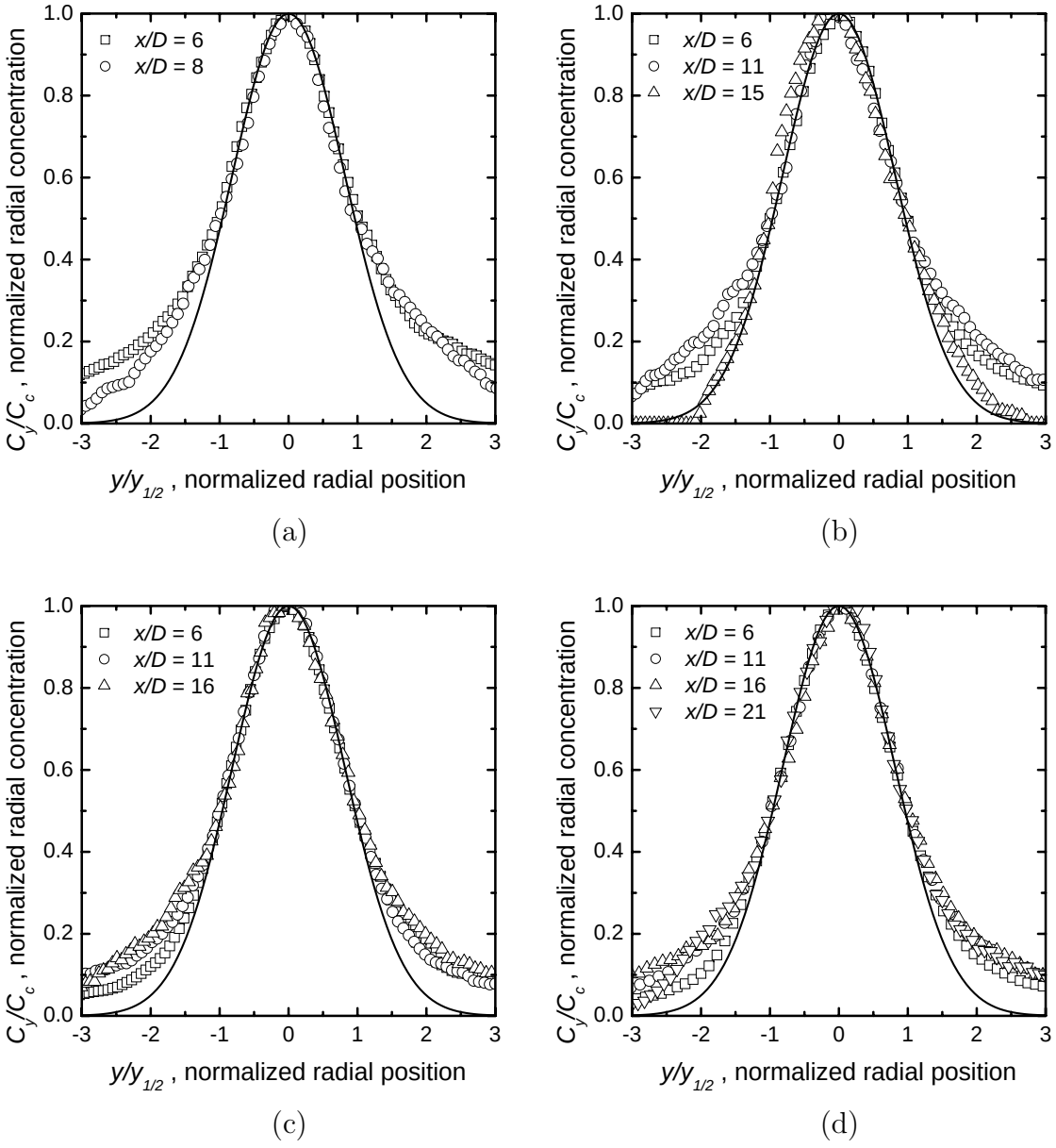

Figure 5.18: Self similarity of the radial concentration profiles of the counterflowing jet with $\theta = 4^{\circ}$ at $Ur = 4$ (a), $Ur = 8$ (b), $Ur = 11$ (c) and $Ur = 14$ (d). The jet diameter of the nozzle used was 8.81 mm. The radial concentration is normalized by the concentration at the geometrical centerline of the cylindrical nozzle. The radial coordinates are normalized by the jet width $y_{_{1/2}}$. The solid curve represents a Gaussian distribution. The error bars of the data are approximately the size of the symbols; an example of this can be seen in Figure 5.4.

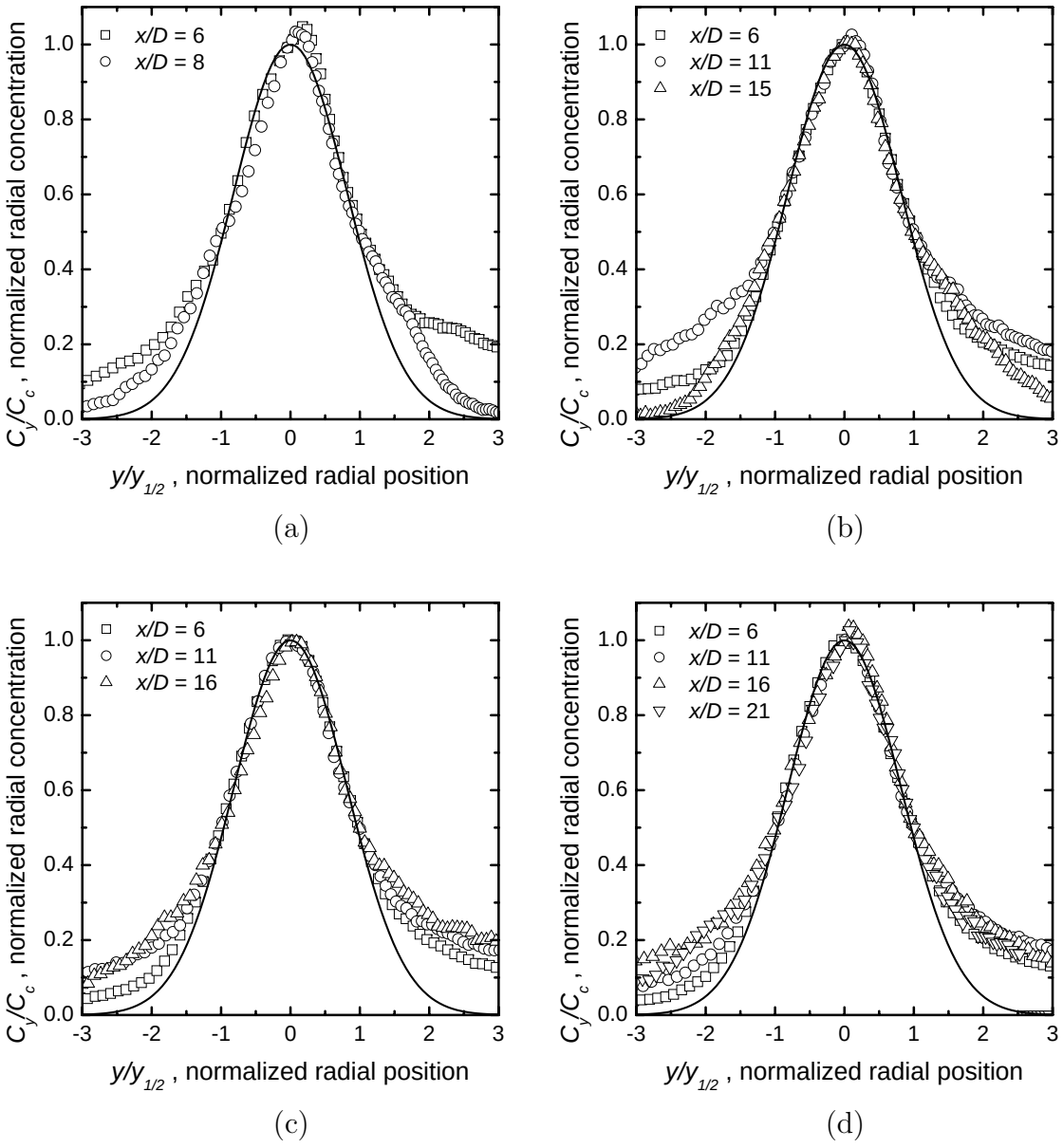

Figure 5.19: Self similarity of the radial concentration profiles of the counterflowing jet with $\theta = 8^{\circ}$ at $Ur = 4$ (a), $Ur = 8$ (b), $Ur = 12$ (c) and $Ur = 14$ (d). The jet diameter of the nozzle used was 8.81 mm. The radial concentration is normalized by the concentration at the geometrical centerline of the cylindrical nozzle. The radial coordinates are normalized by the jet width $y_{1/2}$. The solid curve represents a Gaussian distribution. The error bars of the data are approximately the size of the symbols; an example of this can be seen in Figure 5.4.

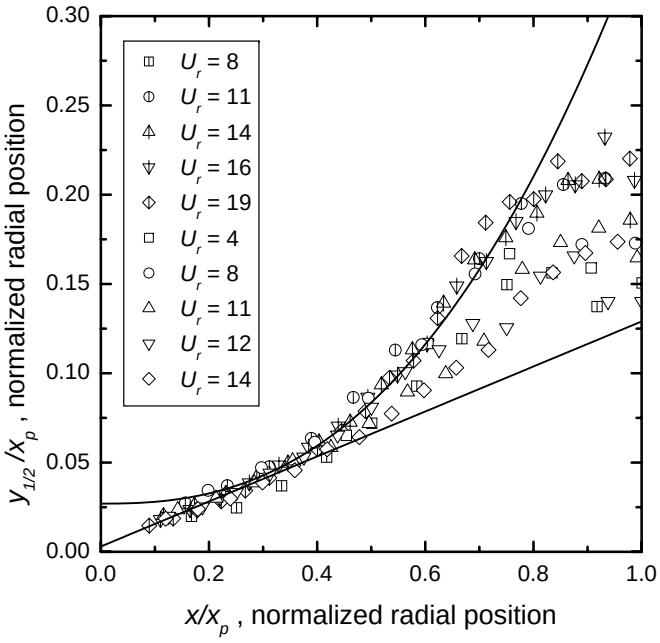

(a)

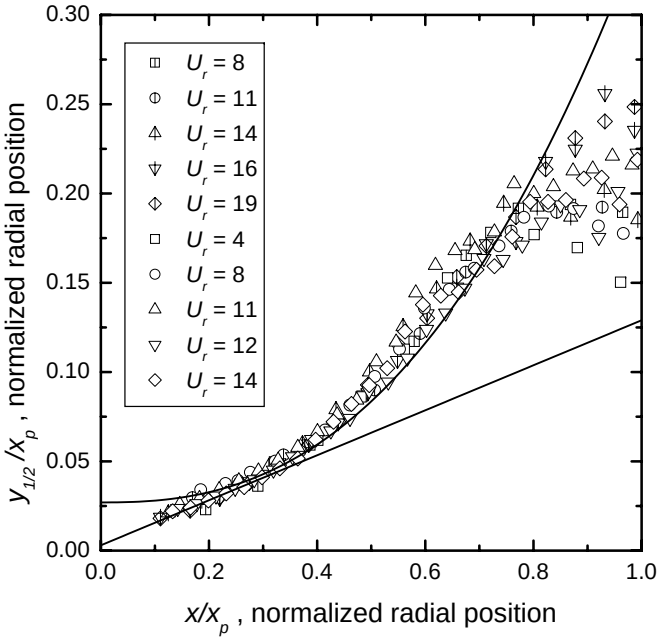

(b)

Figure 5.20: Concentration jet width ($y_{1/2}$) of the counterflowing jet at different jet to counterflow velocity ratios (U_r) for $\theta = 4^o$(a) and $\theta = 8^o$(b). The solid line represents the empirical equations of the jet width for the case of $\theta = 0^o$ (Equations 5.2 and 5.3). Open symbols D = 8.81 mm and cross symbols D = 5.64 mm.

Chapter 6

Conclusion and Recommendation

6.1 Conclusion

This work experimentally studied the physics of counterflowing jets. The effects of small inclinations on the spreading of the jet and the centerline concentration decay were investigated. This investigation was intended to generate information to describe the physical properties of this jet with confidence. The study was focused on the geometrical lengths of the mean concentration scalar field. The scalar field of the jet was measured using a planar laser induced fluorescence method that incorporates an alternative of converting fluorescein intensity to concentration data. Each chapter in this thesis was presented as an independent publication, therefore each has its own conclusion sections. The present chapter summarizes some of the conclusions of each of the chapter:

1. The Powell lens® generated a thin laser sheet with an approximately uniform distribution of light intensity. It was shown that the correction process removed the non uniformities of the laser sheet, via a very simple postprocessing routine.

2. Attenuation of laser intensity and photobleaching were found to be negligible for the level of dye concentration used in this investigation. As a result, the calibration process was required just to remove and correct the non uniformities apparent in the laser sheet, resulting in reliable scalar concentration data.

3. Geometrical length scales of the counterflowing jet were defined using the 5 % contour of the mean scalar concentration field. These geometrical length scales are: the maximum axial penetration (x_p), the maximum lateral penetration (y_p), and the axial location of the maximum lateral penetration (x_b). On average, the value of x_b was found to be approximately 70 % of the maximum axial penetration.

4. The flow of a counterflowing jet can be divided into three regions, the first being the zone of flow establishment, which contains the iso-concentration core. The length of this zone was found to change with the jet to counterflow velocity ratio (U_r). For higher values of U_r the effects of the iso-concentration core were found at larger distances downstream from the exit of the jet. In the present investigation the effects of the iso-concentration core were observed up to $6D$ in the downstream direction. The second, the established flow region, which was found downstream of the zone of flow establishment, up to 70 % of the total penetration length. In this region the flow behaves as a jet in quiescent surroundings, where the flow is dominated by the jet flow. Finally, the mixing zone, which was found at axial distances greater than 0.70 x_p. In this zone the fluctuating behavior of the jet was observed, and the properties of the flow were dominated by the counterflow stream. In the mixing zone the physical properties of the spreading of the jet cannot be clearly defined.

   In real situations the regions of the counterflowing jet are separated by a transition zone. For instance, the transition zone between the established flow region and the mixing zone was experimentally observed at axial distances within 60 to 80 percent of the total penetration length.

5. Two different ratios of the geometrical lengths (y_p/x_b and y_p/x_p) were used to generate empirical equations to predict the centerline concentration decay of the counterflowing jet in the established flow region. The ratios of the length scales were found to change linearly with the jet to counterflow velocity ratios studied in this investigation. The ratios of the geometrical scales were used to

generate a universal form of the spreading of the jet within the inner region.

6. The axial length scale $x_{1/e}$ was successfully used to generate a similar form of the centerline concentration decay of the jet in the established flow region. It was observed that the value of $x_{1/e}$ changes linearly with U_r.

7. Two different regions of the growth of the concentration jet width were defined. They are the linear growth region, where the jet width growths linearly with the axial location, and the power law growth region, were the growth of the jet is represented by a power law function. The linear growth region extends up to 30% of the maximum axial penetration of the jet. The power law growth region can be found between 30 to 60 percent of the maximum axial penetration. The growth of the jet for axial distances greater than 0.60 x_p was observed to be affected by the chaotic behavior of the fluctuations in the mixing zone.

8. It was observed that variations in the inlet yaw angle (θ) of the nozzle significantly affected the length of the maximum axial penetration of the jet. The higher the value of θ, the shorter the penetration length (x_p). At larger values of θ the counterflow can easily break into the flow of the jet, resulting in a more rapid deceleration of the jet flow and therefore reducing the maximum axial penetration of the jet.

9. The centerline concentration decay of the counterflowing jet with small inlet yaw angles was found to present similar characteristics as the observations for a counterflowing jet with no inclination, when the axial location is normalized by the value of the mean penetration distance x_p.

10. The symmetry of the jet spreading was observed to be affected by the value of the inlet yaw angle. The asymmetry was more evident at low values of U_r (e.g. $U_r = 4$) and greater value of θ (e.g. $\theta = 8^o$). The similarity function found for the counterflowing jet with $\theta = 0^o$ within the inner region of the jet was also observed for the case of the jet with small inclinations.

11. The average jet width of the counterflowing jet with small inlet yaw angle was found to grow following the function that describes the jet growth of the counter with no inlet yaw angle. The two regions; the linear growth region and the power law growth region, were also observed in the counterflowing jets with small inclinations. The linear growth region was found to be extended up to 30 % of the maximum penetration, and the power law growth region was observed for axial values between 30 to 55 percent.

6.2 Recommendations and Suggestions

The following suggestions are proposed for consideration in future work:

1. In the present investigation different jet diameters (D) were investigated; 8.81 mm and 6.54 mm. For the case of the larger diameter the maximum jet to counterflow velocity ratio evaluated was 14. Values of U_r greater than 14 were found to be out of the camera field of view. On the other hand for the case of D equal to 6.54 mm, the maximum value of U_r was 19. Therefore, it would be ideal to compare the two different jet diameters at every flow condition and at larger values of U_r.

2. As was previously mentioned, the counterflowing jet presents a random fluctuation of the jet. The natural frequency of these fluctuations has not been systematically investigated. Thus, the natural frequency of the jet, as well as the effect of averaging time and sample rate of the properties of the jet could be the topic of a very interesting investigation.

3. The counterflowing jet was investigated with no information regarding the velocity field. In addition to the findings of this investigation, a better understanding of the mixing of the counterflowing jet would be achieved if the concentration field and velocity field are measured simultaneously. An alternative is given by combining planar laser induced fluorescence and particle image velocimetry.

4. The value of the Reynolds numbers used in this investigation are relatively small compared to the values used in study of jets in other geometries. It would be interesting to investigate the physical properties of the counterflowing jet at higher Reynolds numbers.

5. The empirical equations obtained for the centerline concentration decay were based on the mean geometrical length scales of the concentration field and inlet yaw angle equal to zero. Therefore, it would be interesting to investigate if these geometrical lengths are valid for the velocity field.

Appendix A

Specifications of the CCD camera

Table A.1: Technical data of the 12 bit SensiCam camera.

Features	*Unit*	*SensiCam SVGA*
Resolution	$Pixel$	1280(H)×1024(V)
Pixel Size	μm^2	6.7×6.7
Sensor format	$inch$	2/3
Readout time full frame	fps	8
A/D Conversion factor	$e-/count$	5
Readout noise	$e-$	7-8
Maximum quantum efficiency	%	≥50 @ 450 nm
Spectral response	nm	280 to 1000
Dynamic range	bit	12 at 12.5 MHz
SNR	dB	69
Exposure/delay time setting	s	100 ns to 1 ms
Anti-blooming		>1000
Non-linearity	%	<1
Binning Horizontal		1 to 8
Binning Vertical		1 to 32
Cooling temperature	^oC	-12
Dark current	$e-.Pixel^{-1}.s^{-1}$	<0.1

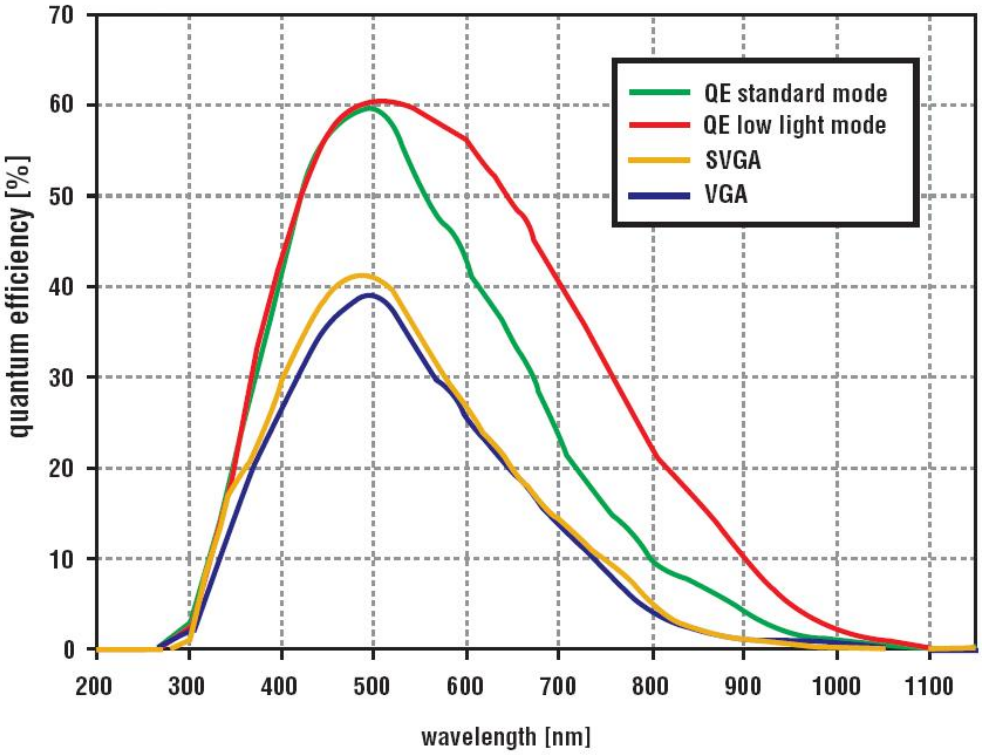

Figure A.1: Spectral response of the SensiCam SVGA. Image taken from the "High Speed CCD Imaging System" specifications sheet. The Cooke corporation imaging. www.cookecorp.com.

Appendix B

Rotameter calibration curves

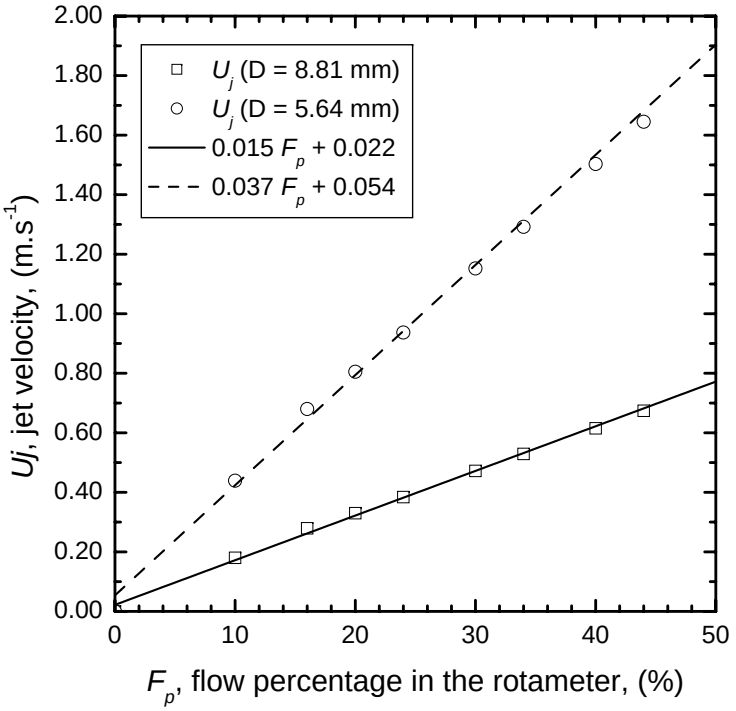

Figure B.1: Calibration curves of the rotameter for the large diameter jet (D = 8.81 mm), and small diameter jet ($D = 5.64$ mm). For both fits the R^2 was found to be 0.997, which suggests that the real data is well approximated by this regression line.